Chemical Geology 670 (2024) 122400

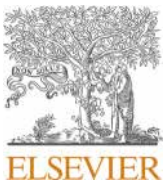

Contents lists available at ScienceDirect

Chemical Geology

journal homepage: www.elsevier.com/locate/chemgeo

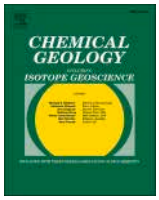

Unravelling the magmatic and hydrothermal evolution of rare-metal granites through apatite geochemistry and geochronology: The Variscan Beauvoir granite (French Massif Central)

Océane Rocher [a,*], Christophe Ballouard [a], Antonin Richard [a], Loïs Monnier [b], Patrick Carr [a], Oscar Laurent [b], Yanis Khebabza [b], Andreï Lecomte [a], Nordine Bouden [c], Johan Villeneuve [c], Benjamin Barré [d], Patrick Fullenwarth [d], Mathieu Leisen [b], Julien Mercadier [a]

[a] Université de Lorraine, CNRS, GeoRessources, F-54506 Vandoeuvre-lès-Nancy, France
[b] CNRS, Géosciences Environnement Toulouse (GET), Observatoire Midi-Pyrénées, 31400 Toulouse, France
[c] Université de Lorraine, CNRS, CRPG, F-54000 Vandoeuvre-lès-Nancy, France
[d] Imerys Ceramics France - Kaolins de Beauvoir, 03330 Echassières, France

ARTICLE INFO

Editor: Dr. Marco Fiorentini

Keywords:
Apatite
Magmatic
Hydrothermal
Rare-metal granite
Beauvoir

ABSTRACT

Peraluminous rare-metal granites (PRMGs) represent highly differentiated crustal granites characterised by extreme enrichment in metals, such as Li, Sn, Nb, Ta, W, and Be. This geochemical specificity is considered to be the result of a succession of magmatic and hydrothermal processes, the importance and individual impact of which are still debated. In this study, we investigate the magmatic and hydrothermal evolution of the Beauvoir leucogranite, a world-class PRMG from the French Paleozoic Variscan belt, through extensive characterisation of suprasolidus to subsolidus apatite. We employ a multi-tracing approach, combining *in-situ* elemental compositions (major, trace, and halogen elements), oxygen isotopic systematics, and U-Pb geochronology.

Four major magmatic and hydrothermal stages were identified through apatite petrography and U-Pb geochronology. Magmatic apatite crystallised at 314.6 ± 4.7 (2s) Ma. Decrease in the amplitude of the Eu anomaly in magmatic apatite from the deeper to shallower granitic units record an increase in the oxygen fugacity (fO_2) of the magma with differentiation, likely contributing to the crystallisation of a first and predominant cassiterite generation. Magmatic apatite REE patterns show significant tetrad effects; they reflect the exsolution of magmatic fluids involved in the precipitation of early hydrothermal apatite replacing igneous minerals or precipitating within veins during greisenisation episode dated at 314.3 ± 5.5 Ma and 311.7 ± 8.1 Ma. Early hydrothermal apatite, characterised by enrichment in Sr or S and Mn-REE depletion along with variable Br/I ratios and $\delta^{18}O$ compositions down to negative values, record mixing dynamics between two fluid end-members: (i) magmatic fluids, and (ii) oxidising meteoric fluids partially reequilibrated with country rocks. Meteoric fluids progressively invaded the Beauvoir PRMG at temperatures ≥ 450 °C and triggered precipitation of a second generation of cassiterite during mixing with magmatic fluids. Two late, non-magmatic, hydrothermal events are dated at 268.3 ± 20.4 Ma and 148.5 ± 26.6 Ma. Related apatite is marked by specific mineralogical and geochemical features such as high As contents and heavy oxygen isotope signatures. They are proposed to be linked to extension-related regional hydrothermal fluid circulation that contributed to metal endowment (U, F-Ba-Pb-Zn) in the crystalline basement and overlying sedimentary cover of Western Europe following the Variscan Orogeny.

Our results demonstrate that apatite is a key mineral to decipher the role of magmatic and hydrothermal processes leading to ore deposition and remobilisation in PRMGs, in relation with geodynamic evolution. Apatite records of external fluid incursions at near-solidus conditions highlight the open system nature of the Beauvoir PRMG, which is crucial for developing fully integrated metallogenic models applicable to similar deposits.

* Corresponding author.
E-mail addresses: oceane.rocher@univ-lorraine.fr, rocher.oceane@hotmail.com (O. Rocher).

https://doi.org/10.1016/j.chemgeo.2024.122400
Received 1 May 2024; Received in revised form 24 August 2024; Accepted 6 September 2024
Available online 10 September 2024

1. Introduction

The circulation of hydrothermal fluids in the Earth's crust is known to play a key role in mineralisation processes, sometimes leading to remarkable metal concentrations, both in terms of metal grade and volume. Mineralised hydrothermal systems can be associated with magma emplacement, and are then designated as ore-forming magmatic-hydrothermal systems. They are found in many geodynamic environments, encompassing continental as well as oceanic domains. Porphyry and greisen-related Sn-W ore deposits represent well-known examples of ore-forming magmatic-hydrothermal systems and result from the intrusion in the upper continental crust of intermediate to felsic magmas (Robb, 2020). In those two systems, fluid circulation within and around the intrusive bodies is proven to be a key element to metal enrichment and controls the spatial distribution of the mineralisation (e.g., Dilles, 1987; Audétat et al., 2000; Burnard and Polya, 2004; Sillitoe, 2010; Lecumberri-Sanchez et al., 2017; Legros et al., 2019). This relation between hydrothermalism and metal deposition seems to be less obvious for rare-metal granites and pegmatites, although they are emplaced in similar geologic settings.

Highly peraluminous rare-metal granites (PRMGs; Linnen and Cuney, 2005) as well as lithium-cesium-tantalum (LCT) pegmatites (Černý and Ercit, 2005) are characterised by extreme enrichment mostly in lithophile metals and halogens (e.g., Li, F, Ta, Nb, Sn, W, and Be), with concentrations exceeding those of the bulk upper continental crust by several order of magnitude (Tischendorf, 1977; Romer and Pichavant, 2020). They result from the crystallisation of highly evolved magmas and typically represent the final magmatic units emplaced during late-orogenic granitic magmatism (Kovalenko et al., 1970; Linnen, 1998; Linnen and Cuney, 2005). The primary mineralisation they host, such as Li aluminosilicates along with Nb-Ta-Sn oxide minerals, is disseminated throughout the intrusive body, and magmatic processes, such as partial melting and fractional crystallisation, play a key role for metal enrichment and deposition (e.g., Raimbault et al., 1995; Pichavant, 2022; Ballouard et al., 2023). However, it has also been long recognised that metasomatism, commonly designated as albitisation and greisenisation, generally affects highly evolved peraluminous granites and pegmatites and may lead to significant mineralogical and geochemical modifications of the ore-bearing mineral assemblage (e.g., Černý, 1986; Schwartz, 1992). Both metasomatic processes typically involve the circulation of a magmatic volatile phase (MVP), also referred to as magmatic fluids, which corresponds to either a supercritical fluid, low-density aqueous vapor, higher density and salinity liquid (possibly hypersaline), or vapor coexisting with liquid exsolved from the melt during its cooling and crystallisation (e.g., Burnham, 1979; Russell et al., 1995; Candela, 1997; Webster et al., 2009). Albitisation was suggested to be related to the interactions between highly fluxed melt or solute-rich magmatic volatile phase (i.e., MVP) and crystals at near-solidus conditions and the metasomatic media can significantly participate to the transport and concentrations of metals such as Li, Nb and Ta (e.g., Badanina et al., 2004; Müller et al., 2018; Kaeter et al., 2018; Ballouard et al., 2020a; Pfister et al., 2023). Greisenisation is presumed to mainly involve acidic and moderately saline (*ca.* 3–10 wt.% NaCl eq) magmatic fluids circulating at temperatures of 200–500 °C (e.g., Burt, 1981; Štemprok, 1987; Shepherd et al., 1985; Taylor, 1988; Schwartz and Surjono, 1990; Halter et al., 1998; Dobeš, 2005; Monnier et al., 2020), although the contribution of external fluids, especially of meteoric origin, has been highlighted in many systems (e.g., Witt, 1988; Cuney et al., 1992; Bettencourt et al., 2005). The relationship between greisen alteration and hydrothermal Sn and/or W mineralisation at subsolidus conditions is well documented (e.g., Monnier et al., 2020; Launay et al., 2021) and in some cases, the interactions between melt and external fluids equilibrated with the host-rocks was proposed as a key process to trigger the supra-solidus precipation of metal-bearing phases such as Nb-Ta oxide minerals (Fouillac and Rossi, 1991; London et al., 1996; Linnen et al., 2019; McNeil et al., 2020). Therefore, deciphering and quantifying the impact of exsolved magmatic fluids as well as external fluids, during and after the magmatic-hydrothermal transition, is essential to fully explain the formation of rare metal granite deposits.

The Beauvoir granite is located in the northern part of the French Massif Central (FMC) of the European Variscan belt and represents one of the best studied examples worldwide of peraluminous high-phosphorus rare-metal granite (PHP-RMG; Cuney et al., 1992). It is characterised by disseminated Sn-Li-Ta-Nb-Be mineralisation, which is broadly considered to initially derive from magmatic processes (Pichavant et al., 1987b; Raimbault et al., 1995; Pichavant, 2022). The importance of fluids in metal deposition has been clearly highlighted (Fouillac et al., 1987; Fouillac and Rossi, 1991; Charoy et al., 2003) with a complex magmatic-hydrothermal system developed following the emplacement of the intrusion that resulted in widespread greisenisation (Aïssa et al., 1987; Merceron et al., 1992; Cuney et al., 1992; Monnier et al., 2020) and hydrothermal mobility of rare metals (Harlaux et al., 2017). However, some key elements of its evolution remain rather poorly constrained, such as the role of external fluids in the greisenisation processes (Cuney et al., 1992; Monnier et al., 2020, 2021). The nature, conditions and timing of circulation of these external fluids, of potential diverse origins, are also debated (Fouillac et al., 1987; Fouillac and Rossi, 1991; Cuney et al., 1992). Furthermore, tectonic and thermal processes leading to the circulation of late fluids throughout the cooled granitic body, their impact on metal endowment, as well as the precise absolute chronology of these events, has not been fully elucidated yet (Merceron et al., 1987, 1992).

The difficulty of precisely deciphering the magmatic, magmatic-hydrothermal and hydrothermal evolutions of rare-metal deposits, like the Beauvoir granite system, arises from the scarcity of minerals representing suitable geochemical proxies to track back these processes. For example, micas from the Beauvoir PRMG have been extensively studied for both major and trace elemental compositions, providing insights into metal behavior from the magmatic to high-temperature hydrothermal stages (Monier et al., 1987; Monnier et al., 2022). However, micas are not stable throughout the global evolution of such system and *in-situ* isotopic data providing direct age and source constraints for hydrothermal fluid circulation are missing. Other traditional tracer minerals, like zircon and monazite, cannot be used as they are rare, and scarce zircon shows a high degree of metamictisation.

Apatite [$Ca_5(PO_4)_3(OH,Cl,F)$] is a common accessory mineral in many igneous and ore-forming systems, sensitive to melt or fluid-induced textural and geochemical changes over a wide range of pressures and temperatures (Harlov, 2015). Apatite can incorporate many major and trace elements in its structure, the most common being REE, Y, Mn, Fe, Sr, Pb, Na and the actinides U and Th substituting for Ca; small, highly charged ions such as Si, S, As and V replacing P; and the halogens (F, Cl, Br and I) in the anion site (Pan and Fleet, 2002). Because of this specific chemistry, apatite has been used for several years to decipher the evolution of igneous suites (e.g., Sha and Chappell, 1999; Belousova et al., 2002; Laurent et al., 2017; Zhang et al., 2020; Xu et al., 2024), the origin and composition of hydrothermal fluids, fluid-rock interactions and constrain the timing of hydrothermal processes (e.g., Harlov, 2015; Kusebauch et al., 2015a, 2015b; Ballouard et al., 2018; Pochon et al., 2018; Andersson et al., 2019; Melfou et al., 2023). Additionnaly, apatite crystallisation or alteration can be dated *in-situ* notably using the U-Pb system (Chew and Spikings, 2015) and high resolution O, Cl, Sr, Nd isotope systematics (e.g., Decrée et al., 2020; Cao et al., 2021; Melfou et al., 2023) can provide crucial information regarding the source and physico-chemical conditions of mineralising melts or fluids.

Apatite occurrences have been well-documented in numerous rare metal deposits related to peraluminous granite magmatism, including the Panasqueira Sn-W deposit (Portugal; e.g., Marignac et al., 2020), the Podlesí Li-Sn-W-Nb-Ta granite stock (Czech Republic; e.g., Breiter et al., 2005), and the Szklary LCT pegmatite (Poland; e.g., Szuszkiewicz et al., 2018). Previous studies of apatite within PRMGs and LCT pegmatites

mainly investigated petrogenetic processes, such as magmatic differentiation or magma mixing (Broska et al., 2004; Hsieh et al., 2008; Chu et al., 2009; Roda-Robles et al., 2022). Few studies used apatite to assess the hydrothermal history of these systems. Apatite geochronology has been employed to constrain the timing of primary magmatic-hydrothermal Sn mineralisation in the Erzgebirge (Germany; Romer et al., 2007), and also provided key constraints on establishing the metallogenic model for the Panasqueira ore system (Launay et al., 2021; Jaranowski et al., 2021). A recent study of apatite from the Mesozoic Qianlishan low-phosphorus PRMG (South China) supported its usefulness as a tracer of magmatic and metasomatic evolution (Zhang et al., 2024). The textural and geochemical record of the magmatic to hydrothermal evolution of PRMG systems such as the Beauvoir deposit remains fragmented, whereas apatite is a ubiquitous mineral crystallising from the supra- to sub-solidus stages in PRMGs due to the high-phosphorus content.

In this study, we couple *in-situ* determination of apatite chemistry, oxygen isotope systematics and U-Pb geochronology to unravel the magmatic and hydrothermal evolution of the Beauvoir system within the geodynamic evolution of the FMC. More specifically, we use apatite as a proxy to (i) constrain the timing of fluid circulations within the Beauvoir intrusion and relative to igneous crystallisation; (ii) trace the origin of successive fluids, the mixing dynamics, the physico-chemical conditions and fluid-rock interactions and (iii) decipher their implications regarding the metal endowment and crystallisation mechanism of rare metal-bearing minerals in the Beauvoir PRMG.

2. Geological setting

2.1. Regional geology

The FMC belongs to the internal zone of the European Variscan belt (Fig. 1a), which results from the main collision between the supercontinents Gondwana to the south and Laurussia to the north (Matte, 1991; Robardet, 2002). Spanning from the Late Devonian to the Early Carboniferous (*ca.* 380 to 290 Ma; Matte, 1986; Ballèvre et al., 2014), this orogenic event ultimately led to the formation of Pangea (Tait et al., 2000).

The structure of the FMC essentially consists of a metamorphic nappe stack, composed of four main tectonic units, developed diachronously during the Devonian to Early Carboniferous and intruded by granitic magmas from *ca.* 360 to 295 Ma (Vanderhaeghe et al., 2020 and references therein). From north to south and from top to bottom, these tectonic units are: the Upper Gneiss Unit (UGU), the Middle Allochthonous Unit (MAU) identified in the Limousin, the Lower Gneiss Unit (LGU) and the Parautochtonous Unit (PAU). In the northern part of the FMC, in the region of Echassières, the stack of the UGU, LGU and PAU forms the Sioule series, an inverted metamorphic sequence (Grolier, 1971) (Fig. 1b). This series is bounded to the west and to the south, respectively, by sinistral and dextral Carboniferous shear zones (i.e., the Sillon Houiller and Sainte-Christine faults, respectively) and underwent at least three significant tectonic-metamorphic episodes (Faure et al., 2009; Schulz, 2009; Do Couto et al., 2015) including: (i) a high pressure D_0 event, during which the UGU experienced high- to ultra-high-pressure eclogite-granulite-facies metamorphism recorded elsewhere in the FMC between 390 and 360 Ma (Lotout et al., 2020; De Hoÿm de Marien et al., 2023); (ii) a D_1 event, characterised by a top-to-the-SW shearing synchronous with migmatisation and exhumation of the UGU and LGU units; and (iii) a medium pressure-medium temperature D_2 event, associated with a top-to-the-NW shearing. D1 and D2 events are thought to have been postdated by the unconformable deposition at *ca.* 330 Ma of the "Tuffs anthracifères" series consisting of weakly deformed and metamorphosed terrigenous sedimentary and felsic volcanic rocks (Bruguier et al., 1998; Do Couto et al., 2015). The Sioule metamorphic series is structured by two major antiforms, in the centre of which the PAU mica schists crop out. They are intruded by two granitic plutons: the Pouzol-Servant porphyritic granite in the southern antiform and the Echassières granitic complex in the northern antiform (Fig. 1b).

2.2. The Echassières granitic complex

The Echassières granitic complex is a circular intrusive body, 3 km in diameter, emplaced during a major N20° shortening episode at the end of the Carboniferous (Gagny et al., 1984; Gagny and Jacquot, 1987; Feybesse, 1985; Blès et al., 1989). It results from the intrusion of at least three granitic units (Cuney et al., 1992; Raimbault et al., 1995)(Fig. 1c): (i) the inferred La Bosse granite, concealed at depth and possibly at the origin of a quartz-wolframite vein system, the La Bosse stockwork, developed within the PAU mica schists; (ii) the Colettes granite, a cordierite-bearing two-mica porphyritic granite; and (iii) the Beauvoir granite, a highly evolved albite-lepidolite-topaz leucogranite hosting disseminated Sn-Li-Ta-Nb-Be mineralisation.

The Beauvoir PRMG was emplaced during the Variscan late-orogenic extensional stage at *ca.* 310–315 Ma (Rb-Sr on whole rock; Duthou and Pin, 1987; Ar-Ar on lepidolite; Cheilletz et al., 1992, and U-Pb on columbite-group minerals; Melleton et al., 2015). It has been studied by many authors, in particular following the drilling of a *ca.* 900 m deep drillhole (GPF1) in 1985 as part of the "Géologie Profonde de la France" (GPF) drilling program (Cuney and Autran, 1987). Petrographic and structural studies highlighted a vertical zonation within the granite, leading to the proposal of three main magmatic units that were inferred to have successively intruded the parautochthonous mica schists of the Sioule metamorphic series (Bouchez et al., 1987; Gagny, 1987; Jacquot and Gagny, 1987; Monier et al., 1987; Rossi et al., 1987). These units are designated as the B1 (~ 100–450 m depth in GPF1), B2 (~ 450–750 m) and B3 (~ 750–880 m) facies, with the B1 unit thought to represent the final and most differentiated magma batch (Fig. 1c). A recent study revealed a more complex sequence composed of 18 sub-units distributed across 4 units (i.e., B1, B1', B2 and B3), which incrementally intruded the host mica schists (Esteves et al., 2024). A last facies, distinguished by its porphyritic texture and referred to as "Beauvoir porphyry enclave", has been encountered within the B2 and B3 units, either as dykes or enclaves (e.g., Cuney et al., 1992; Monnier et al., 2018). Its chemical characteristics closely resemble those of the Colettes granite, indicating a possible genetic connection (Raimbault and Azencott, 1987; Monnier et al., 2018).

The Beauvoir PRMG exhibits a remarkable enrichment in fluxing and litophile elements (Li, P, F, Rb, Cs, Be, Nb, Ta, Sn, W, U), especially at its apical part (Raimbault et al., 1995), and therefore shares many characteristics with rare-element pegmatites of the LCT family (Raimbault, 1998; Černý and Ercit, 2005). For instance, the concentrations in Li, Sn, and Ta respectively vary from 0.1 to 1 wt.%, 0.02 to 0.4 wt.%, and 40 to 500 ppm, values that largely exceed those of the bulk upper continental crust (24 ppm for Li; 2.1 ppm for Sn; and 0.9 ppm for Ta; Rudnick and Gao, 2003). Crystallisation experiments have demonstrated that the melts that formed the Beauvoir PRMG crystallised under pressures of 100 to 300 MPa at very low temperatures (below 670 °C) with solidus estimated to be near 550 °C, a common characteristic of flux-rich granitic melts (Pichavant et al., 1987a; Pichavant, 2022). Albite, quartz, K-feldspar and Li-F-micas, with zinnwaldite to lepidolite compositions, represent the major magmatic minerals of the Beauvoir crystallisation sequence, along with cassiterite (Sn; generation I), topaz (F), apatite (F), amblygonite-group minerals (Li-F), herderite (Be-F), zircon, columbite-group minerals (Nb-Ta), pyrochlore-group minerals (Nb-Ta-U), and uraninite (U) as accessories (Pichavant et al., 1987a; Rossi et al., 1987; Johan et al., 1988; Cuney et al., 1992; Raimbault et al., 1995; Pichavant, 2022)(Fig. 2). This magmatic paragenesis evolves across the three magmatic units (i.e., B1, B2 and B3). The proportion of accessory minerals tends to increase from the B3 unit to the most evolved B1 unit. A similar trend is observed for the abundance of albite, whereas the proportions of quartz and K-feldspar progressively decrease from the B3 to the B1 unit, with Li-micas transitioning from zinnwaldite to lepidolite.

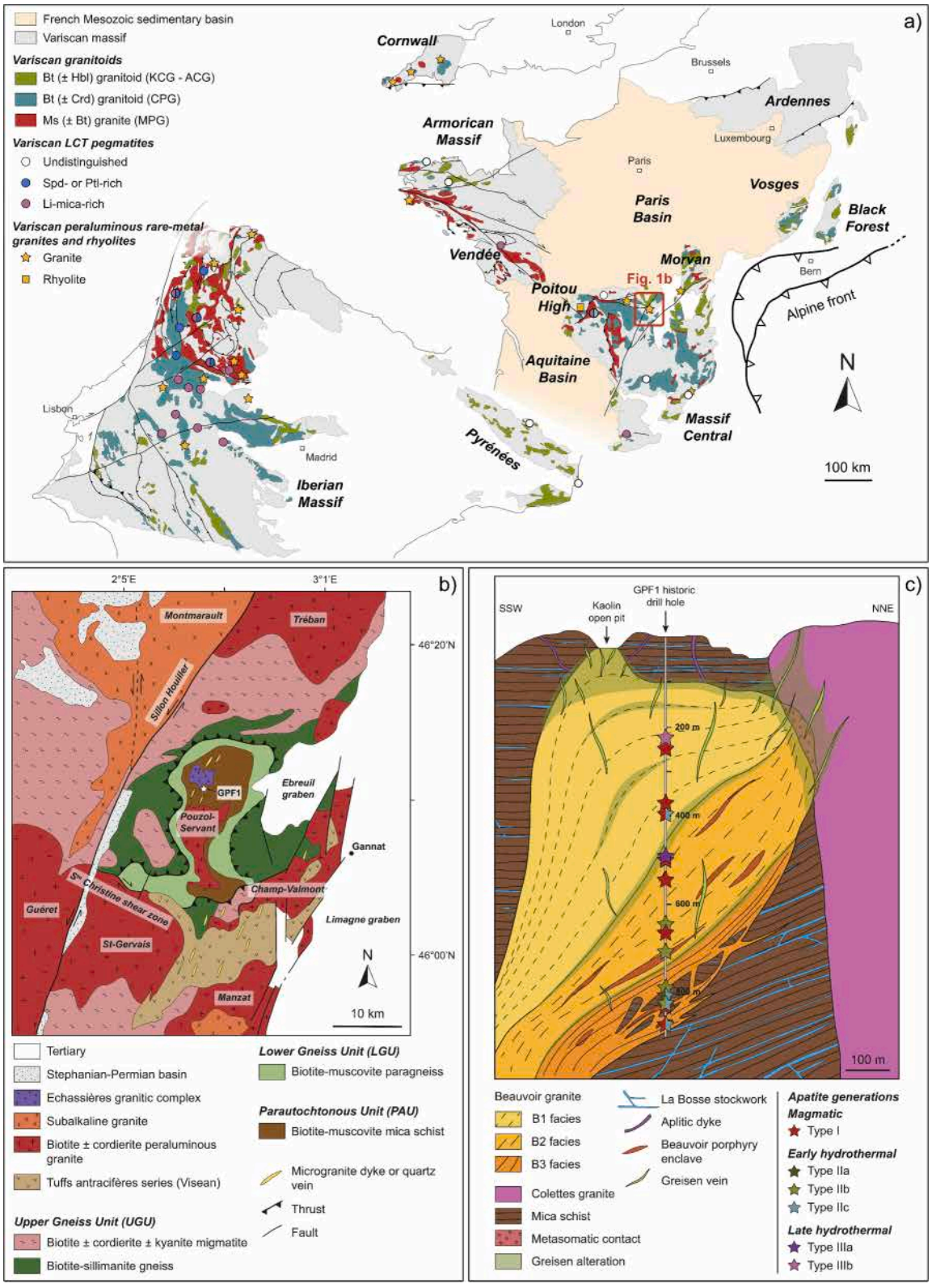

Fig. 1. (a) Schematic representation of the western European Variscan belt representing the main terranes and showing Variscan granitoids, as well as LCT pegmatites, rare-metal granites and rhyolites (modified from Ballouard et al. (2024)). The granitoids typology is from Barbarin (1999). MPG: muscovite-bearing peraluminous granites; CPG: cordierite-bearing peraluminous granitoids; KCG: K-rich and K-feldspar porphyritic calc-alkaline granitoids. ACG: amphibole-rich calc-alkaline granitoids. Mineral abbreviations according to Warr (2021). (b) Simplified geological context of the Echassières granitic complex in the northern part of the French Massif Central (FMC) (modified from Cuney et al. (1992) and Harlaux et al. (2017)). The location of the GPF1 deep drillhole that crosscuts the Beauvoir PRMG is indicated by the white star. (c) Interpretative cross-section of the Beauvoir PRMG representing the vertical magmatic internal zoning composed by the three successive units B1, B2, and B3 (modified from Cuney et al. (1992) and Monnier et al. (2018)). The location of the studied samples is shown together with the classification of the apatite generations encountered (section 4.1).

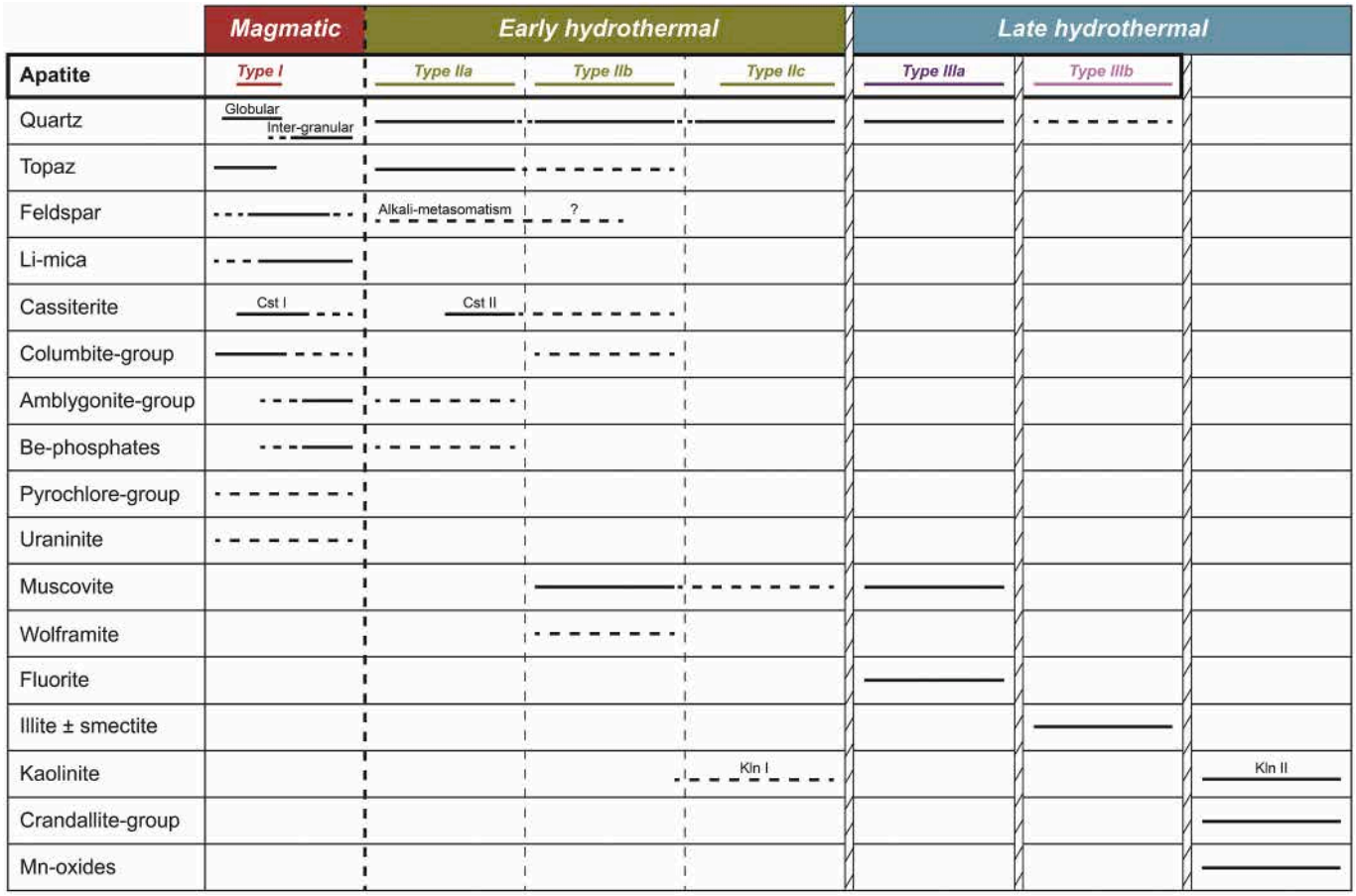

Fig. 2. Paragenetic synthesis of magmatic and hydrothermal mineralogical associations of the Beauvoir system. The hatched areas indicate a temporal and genetic disconnection of events during the early and late hydrothermal evolution of the Beauvoir PRMG. Magmatic paragenesis is based on Pichavant et al. (1987a), Rossi et al. (1987), Johan et al. (1988), Cuney et al. (1992), Raimbault et al. (1995), and Pichavant (2022). The early hydrothermal paragenesis relies on the studies of Merceron et al. (1987, 1992) and Monnier et al. (2018, 2019). The late hydrothermal paragenesis draws from the descriptions of Merceron et al. (1987, 1992). See sections 2.4 and 4 for details on the different apatite generations. Abbreviations follow the IMA conventions compiled by Warr (2021).

2.3. *The Beauvoir magmatic-hydrothermal system*

The magmatic-hydrothermal to hydrothermal evolution of the Beauvoir PRMG is complex and characterised by multiple fluid circulation episodes. Four major stages can be recognised (Cuney et al., 1992; Merceron et al., 1992; Monnier et al., 2019): (i) the early hydrothermal stage (200–550 °C), driven by the intrusion heat, mostly led to the development of vertical quartz veins, as well as the greisen alteration of both the intrusion and the surrounding rocks (i.e., the Colettes granite, La Bosse stockwork and host mica schists); (ii to iv) three late hydrothermal stages were associated to fluid circulation genetically and temporally disconnected from the Beauvoir PRMG emplacement. The first two late hydrothermal stages are respectively characterised by the development of sub-vertical quartz veins associated with fluorite (< 250 °C) and illite-smectite (100–200 °C) precipitation, while the third and final stage resulted in widespread supergene kaolinisation (≤ 50 °C), essentially affecting the apical part of the Beauvoir intrusion and coeval with low-temperature phosphate precipitation (i.e., crandallite-group minerals) (Fig. 2).

The early hydrothermal stage can also be designated as a magmatic-hydrothermal transition. This transition consists of a continuous evolution, throughout cooling of the granitic melt, from an initially purely magmatic system dominated by crystal-melt interactions to a system dominated by crystal-melt-fluid phase interactions, that finally results in a purely hydrothermal system associated to fluid-rock interactions (Halter and Webster, 2004; Audétat and Edmonds, 2020). The term "early hydrothermal stage" thus includes the magmatic and early hydrothermal stages described by Merceron et al. (1992) and the early orthomagmatic and greisenisation stages as detailed by Monnier et al. (2022). It has been initiated by the exsolution of hot (> 490 °C) magmatic fluids from the Beauvoir melts during crystallisation. The early circulation of these magmatic fluids (i.e. L1 fluids described by Aïssa et al. (1987)) primarily led to acidic F-rich alteration, predominantly occurring in the contact zones between the granite and the host mica schists (Cuney et al., 1992; Monnier et al., 2020). Magmatic fluids concentrated in the shallowest B1 unit, generating an overpressure abruptly released by fracturing (Aïssa et al., 1987; Cuney et al., 1992) that induced the emplacement of sub-vertical, centimetric quartz veins (Merceron et al., 1987, 1992), as well as the phase separation of primary magmatic fluids (L1) into a high-salinity brine (L2) and a low- to moderate-salinity vapor (V2) (Aïssa et al., 1987; Harlaux et al., 2017). Primary (L1) and secondary (L2 and V2) magmatic fluids progressively evolved by cooling and mixing with fluids of external origin (e.g., meteoric or metamorphic fluids; Aïssa et al., 1987; Cuney et al., 1992; Monnier et al., 2020). These fluid circulations were responsible for the widespread greisenisation of the Beauvoir intrusion and adjacent rocks. Greisen-alteration thus seems temporally and genetically linked to the Beauvoir intrusion emplacement dated at *ca.* 310–315 Ma (Duthou and Pin, 1987; Cheilletz et al., 1992; Melleton et al., 2015), as suggested by the age of 307 ± 3 Ma obtained through U-Pb dating of greisen alteration-related monazite within the Echassières complex (Monnier et al., 2021). Greisenisation has been particularly intense at the apical part of the Beauvoir PRMG but is also encountered at depth, essentially at the transition zones between the three magmatic units (i.e., B1, B2

and B3; Merceron et al., 1992). It involved the pervasive replacement of igneous minerals, mainly feldspar (± quartz and lepidolite), by a quartz-muscovite assemblage, commonly associated with the precipitation of other secondary minerals, such as apatite, topaz, cassiterite (generation II), columbite- and pyrochlore-group minerals, as well as the formation of millimetric quartz-muscovite veins (Merceron et al., 1987; Monnier et al., 2018, 2019) (Fig. 2) The progressive cooling of greisen-forming fluids is thought to be associated with successive crystallisation of muscovite, pyrophyllite, donbassite, tosudite and minor early kaolinite (Kln I on Fig. 2) (Merceron et al., 1987, 1992). Sodic (i.e., albitisation) and potassic alterations were also observed to a lesser extent and were proposed to derive from the circulation of the highly saline magmatic brine L2 (Monnier et al., 2018). During greisenisation, Na^+ and K^+ are released into the aqueous solution, increasing the alkali/H^+ ratio and potentially triggering alkali-metasomatism (e.g., Štemprok, 1987; Pirajno, 2009; Ballouard et al., 2020a). In constrast, alkali-metasomatim may induce greisenisation by progressively decreasing the alkali/H^+ ratio of the system. Therefore, the greisen and alkali alterations encountered in the Beauvoir PRMG might have been driven by the same fluids, as the associated replacement reactions form a self-sustaining chemical system, potentially leading to multiple successive generations of albitite and greisen (e.g., Ballouard et al., 2020a).

The three distinct late hydrothermal stages are interpreted to derive from the circulation of external fluids (i.e. meteoric, metamorphic fluids or basinal brines) throughout the cooled granitic body (Merceron et al., 1992), and consist in: (i) fluorite mineralisation, (ii) illite ± smectite vein fillings, and (iii) widespread supergene kaolinisation. Fluorite occurs in association with quartz in sub-vertical veins or in inter-granular secondary porosity, as well as a replacement of igneous minerals, in particular albite (Merceron et al., 1987). Fluorite precipitation seems to clearly postdate greisen alteration and to be related to the circulation of external fluids; however its timing and the origin of involved fluids remain poorly constrained (Merceron et al., 1987; Raimbault, 1988). The precipitation of illite results from hydrothermal fluid circulation at temperatures of *ca.* 200 °C during the Upper Jurassic (151 ± 4 Ma obtained by K-Ar dating of illite; Merceron et al., 1987). It is followed by the precipitation of illite/smectite mixed-layer minerals as vein-filling materials. Finally, supergene kaolinisation occured during the last alteration event of the Beauvoir PRMG (Eocene to Oligocene; Merceron et al., 1987; Charoy et al., 2003; Monnier et al., 2019). Kaolinisation has been particularly intense at the apical part of the intrusion, and mostly overprints greisen alteration. Kaolinite is found as replacement of greisen-related muscovite and igneous feldspar, and apatite is systematically altered either into kaolinite or crandalite-group minerals. Accessory Mn-oxides, W-rich goethite, crandalite-group minerals, and illite/smectite mixed layer clays commonly accompany kaolinite precipitation. These minerals also co-precipitated with quartz in late brecciated veins exhibiting evidence of multiple reactivation episodes (Monnier et al., 2019). Two generations of kaolinite have then been identified, the first and minor one (Kln I on Fig. 2) precipitating at the end of the early hydrothermal stage, and the second one resulting from the supergene alteration event (Kln II in Fig. 2).

2.4. Apatite occurences in the Beauvoir PRMG

Three apatite generations were previously described within the Beauvoir PRMG (Aubert, 1969; Wang, 1988; Johan et al., 1988; Cuney et al., 1992; Monnier et al., 2019).

Apatite I, also referred to as apatite A by Wang (1988), represents an accessory mineral found throughout the entire intrusive complex, with a lesser occurrence in the B1 unit. It is characterised by a green to blue natural colour, and forms euhedral to subhedral crystals included in or closely associated with igneous topaz. Based on this textural relation, apatite I has been interpreted as an early crystallising mineral in the magmatic sequence (Wang, 1988; Johan et al., 1988; Cuney et al., 1992). Apatite I exhibits high MnO contents, decreasing from the B3 and B2 units (2–7 wt.%) to the B1 unit (< 1 wt.%) (Wang, 1988).

Apatite II forms colourless to green subhedral to anhedral grains, typically replacing apatite I and albite within the three magmatic units (Aubert, 1969; Wang, 1988; Johan et al., 1988). Although it essentially co-precipitates with quartz, muscovite and topaz, apatite II is locally associated with fluorite. Its precipitation is thought to derive from the extensive greisenisation affecting the Beauvoir PRMG, as well as the surrounding rocks.

Finally, a third apatite population (apatite III) has been described by Cuney et al. (1992) and Charoy et al. (2003). It forms a rim on crandallite-group minerals, more particularly goyazite, and mainly differs from apatite I and II by its significant SrO content, reaching up to 1.5 wt.%. The precipitation of crandallite-group minerals in the Beauvoir PRMG was presumed to result from the low-temperature destabilisation of albite and lepidolite during the Oligocene continental extension, responsible for the opening of the Limagne graben (Charoy et al., 2003).

3. Material and methods

3.1. Sampling strategy

As described in section 2, the evolution of the Beauvoir PRMG is characterised by three main supra- and sub-solidus stages: (i) magmatic, (ii) early hydrothermal and (iii) late hydrothermal stages. Sixteen samples were collected along the GPF1 historic drillhole to ensure the best representativity possible of each stage within the three magmatic units (i.e. B1, B2, and B3; Fig. 1c; Table 1). Eight samples of granite with little to no visible alteration were selected as reference for the magmatic stage: three from B1, four from B2, and one from B3. The early hydrothermal stage was investigated through eight samples. Among these, five samples were chosen to represent the different degrees of pervasive greisen alteration in the Beauvoir PRMG (390.9, 642.7, 789.7, 819.5 and 862.0 m), two samples displayed veins formed by early and greisen-related fluid circulation (704.2 and 801.0 m), and one sample represented greisen alteration of the pre-existing La Bosse stockwork (816.5 m). Finally, two samples were analysed for the late hydrothermal stages, respectively from the B1 (221.1 m) and B2 (486.5 m) units. A pair of thin and thick sections (30 μm and 150–200 μm, respectively) was prepared for each sample to provide equivalent areas for petrographic study and analytical data acquisition.

Previous studies suggested the contribution of external fluids potentially reequilibrated with the country rocks during the development of the Beauvoir magmatic-hydrothermal system (section 2.3; Fouillac and Rossi, 1991; Merceron et al., 1992; Charoy et al., 2003). For comparison with apatite compositions, and to trace external fluid contribution, we investigated the bulk geochemical compositions of representative metasedimentary rock samples from the Sioule series, which represent the country rocks of the Echassières magmatic complex. The location and a brief description of the samples are provided in Table S9 (Supplementary Material 2).

3.2. Imaging and analytical methods

Details about analytical protocols are provided along with data in Supplementary Material 1 and are briefly summarised here.

The mineralogy, textural relationships and chemical zoning of apatite grains were investigated using optical microscopy, cathodoluminescence (CL) imaging with an OPEA Cathodyne connected to a Nikon Eclipse LV100 microscope, micro-XRF chemical mapping along with backscattered electron (BSE) imaging using a TESCAN VEGA3 Scanning Electron Microscope (SEM) at GeoRessources (Nancy, France). Higher resolution chemical maps along with quantitative major and minor element compositions of apatite were obtained by electron microprobe analyses (EPMA) at GeoRessources using natural and synthetic standards. The structural formulae of the distinct apatite generations were calculated based on 12.5 oxygen atoms per formula unit

Table 1
Summary of samples and apatite characteristics. All samples derive from the GPF1 historic drillhole. Abbreviations follow the IMA conventions compiled by Warr (2021), with the exception of AGM: amblygonite-group minerals; CGM: columbite-group minerals; CdlGM: crandallite-group minerals PGM: pyrochlore-group minerals; M: magmatic mineral; EH: early hydrothermal mineral; LH: late hydrothermal mineral.

Generation	Type	Facies	Depth (m)	Sample description	Mineral association	Apatite main petrographic features
Magmatic	**I**	Beauvoir – B1	247.0 368.7 390.9	Granite with little to no visible alteration	**M:** Quartz, albite, K-feldspar, lepidolite/zinnwaldite, topaz, apatite, AGM ± CGM, PGM, cassiterite, zircon	Anhedral to euhedral blue to green apatite closely associated with igneous topaz and commonly containing inclusions of zircon and CGM
		Beauvoir – B2	495.3 546.5 660.4 862.0			
		Beauvoir – B3	824.0			
Early hydrothermal	**IIc**	Beauvoir – B1	390.9	Slightly greisenised granite	**M:** Quartz, albite, K-feldspar, lepidolite, topaz, apatite, AGM ± CGM, PGM, cassiterite, zircon **EH:** Apatite ± muscovite	Anhedral apatite replacing igneous AGM
	IIb	Beauvoir – B2	642.7	Greisenised Beauvoir granite overprinted by kaolinite	**M:** Quartz, lepidolite, albite ± cassiterite, CGM **EH:** Quartz, muscovite, topaz, apatite **LH:** Kaolinite	Anhedral grains partially replaced by a kaolinite
	IIb	Beauvoir – B2	704.2	Vein at the contact between the greisenised Beauvoir and porphyric granites	**EH:** Quartz, apatite ± muscovite	Fringes of sub-euhedral to euhedral apatite mainly growing sub-perpendicular to the strike of the quartz vein
	IIb	Beauvoir – B3	789.7	Beauvoir granite showing traces of oxidative late alteration	**M:** Quartz, albite, K-feldspar, zinnwaldite, topaz, apatite, AGM ± CGM, PGM, cassiterite, zircon **EH:** Apatite ± muscovite **LH:** CdlGM, kaolinite, Fe-oxides	Anhedral apatite replacing igneous minerals, in particular albite, in turn partially replaced by CdlGM
	IIa and IIc	Beauvoir – B3	801.0	Polyphase vein at the contact between the Beauvoir granite and a mica schist enclave	**EH:** Quartz, topaz, cassiterite, lepidolite, muscovite, apatite **LH:** CdlGM, Sr-sulfide	**IIa:** Sub-euhedral apatite co-precipitating with quartz, topaz and cassiterite **IIb:** Anhedral apatite co-precipitating with Ms and partially replaced by CdlGM associated to Sr-sulfide
	IIb	Pre-existing La Bosse stockwork	816.5	Disseminated greisen in a stockwork enclave	**EH:** Topaz, muscovite, quartz, apatite ± wolframite, rutile, monazite	Subhedral to euhedral apatite commonly containing monazite inclusions
	IIb and IIc	Beauvoir – B3	819.5	Greisenised Beauvoir granite	**M:** Quartz, zinnwaldite, Be-phosphates **EH:** Quartz, muscovite, apatite	**IIb:** Anhedral apatite found in replacement of zinnwaldite and co-crystallising with a Qz-Ms assemblage **IIc:** Anhedral red apatite replacing Be-phosphates
	IIc	Beauvoir – B2	862.0	Slightly greisenised granite	**M:** Quartz, albite, K-feldspar, zinnwaldite, topaz, apatite, AGM ± CGM, PGM, cassiterite, zircon **EH:** Apatite ± muscovite	Anhedral to subhedral apatite co-precipitating with Ms and replacing igneous minerals such as albite
Late hydrothermal	**IIIa**	Beauvoir – B2	486.5	Polyphase pervasive vein	**LH:** Fluorite, quartz, muscovite, apatite, illite	Subhedral to euhedral apatite precipitating at the edge of the fluorite vein
	IIIb	Beauvoir – B1	221.1	Vuggy quartz vein with a Mn-oxides selvedge	/	Aggregates of small euhedral apatite grains precipitating in the vein porosity

(apfu). Whole-rock geochemical analyses of metasedimentary rocks from the Sioule series were performed at the SARM (Nancy, France).

Measurements of oxygen isotopic composition and halogen concentrations (F, Cl, Br and I) of apatite were performed by ion microprobe (SIMS) at the CRPG (Nancy, France). Analyses were performed close to EPMA spots by focusing a primary Cs^+ ion beam on a raster area of ~15 × 15 and 5 × 5 μm for oxygen isotope and halogen compositions, respectively. Conditions similar to those of Decrée et al. (2020) were used for O isotope measurements. Correction of instrumental mass fractionation (IMF) was conducted by analysing the Durango fluorapatite reference material ($\delta^{18}O$ = 9.4 ‰; Trotter et al., 2008). The $^{18}O/^{16}O$ ratios are expressed as $\delta^{18}O$ values and are normalised to the Vienna Standard Mean Ocean Water (VSMOW) composition ($^{18}O/^{16}O$ = 0.0020052; Baertschi, 1976) with long-term reproductibility (2s) varying from 0.08 to 0.20 ‰. Halogen concentration analysis protocol follows that of Melfou et al. (2023). Halogen compositions were again determined relative to the Durango fluorapatite standard with detection limits of 6.6 × 10^{-5} ppm for F, 1.3 × 10^{-4} ppm for Cl, 3.8 × 10^{-3} ppm for Br, and 7.9 × 10^{-4} ppm for I. Relative standard deviations are (RSD, 1s) of 2.99 % for F, 0.45 % for Cl, 6.00 % for Br, and 1.19 % for I.

Trace element concentrations and U-Pb isotope compositions of apatite were determined by LA-ICP-MS at Géosciences Environnement Toulouse (GET, France) and GeoRessources laboratories, and similar analytical protocols were used in both laboratories. Laser ablation for trace element analyses were performed with a constant spot size of 30 μm. For trace element analyses, the NIST SRM 610 glass was used as primary reference material for the correction of mass bias and instrumental drift (Jochum et al., 2011). The NIST SRM 612 glass (Jochum et al., 2011) and the Durango apatite were used as secondary control materials. Trace elements concentrations determined for the Durango apatite mostly fall within the range of reported values (note that this apatite is not homogenous in most elements; Table S6 in Supplementary Material 2). The signal on ^{43}Ca within apatite was used as the internal standard, assuming a stoichiometric Ca content of 39.74 wt.%. For U-Pb analyses, isotope ratios were initially determined using the NIST SRM 610 glass again as a primary reference material for the correction of mass bias and instrumental drift. Matrix-corrected ratios were then determined by an average fractionation factor calculated for multiple apatite reference materials employed throughout the study, including Madagascar (Thomson et al., 2012), McClure Mountain (Schoene and Bowring, 2006), Durango (McDowell et al., 2005) and Duluth apatite (Schmitz et al., 2003). U-Pb ages presented in this study are lower intercept ages calculated in $^{238}U/^{206}Pb$ vs. $^{207}Pb/^{206}Pb$ Tera-Wasserburg diagrams with IsoplotR (Vermeesch, 2018) and errors are quoted at the 2-sigma level. Despite similar analytical protocols, systematic bias of U-Pb isotope compositions and ages will exist between both laboratories. We estimate the interlaboratory reproducibility to be ± 1.0 % relative from the dispersion of apatite reference material lower intercept ages obtained during this study (Fig. S1 in Supplementary Material 1). This uncertainty is added in quadrature to any lower intercept date. The resulting total uncertainty is referred to in the following sections and indicated in brackets on Figs. 11 and S2 (Supplementary Material 1).

4. Results

4.1. Apatite petrography

Three major apatite generations were identified (Table 1; Figs. 2, 3, 4, 5): (i) Magmatic apatite (type I) interpreted to have crystallised from the granitic melt; (ii) Early hydrothermal apatite (types IIa, IIb and IIc) which formed through fluid circulation associated with greisen alteration and directly related to the emplacement and cooling of the Beauvoir granite body; (iii) Late hydrothermal apatite (types IIIa and IIIb) that precipitated following fluid circulations thought to be genetically and temporally disconnected from the granite emplacement.

4.1.1. Magmatic apatite

Magmatic apatite (type I) is widespread in unaltered to weakly altered granite samples throughout the entire intrusive complex, with a relatively lower abundance in the B1 unit in comparison to the B2 and B3 units. Its natural colour varies from dark green to deep blue, being mostly dark green in the B1 unit and deep blue in the B2 and B3 units (Figs. 3a-c, 4b). This colour diversity between magmatic units was already outlined by Wang (1988). Apatite I forms euhedral to subhedral grains co-crystallising with typical magmatic minerals as defined by phase equilibria experiments of the Beauvoir PRMG (e.g., Pichavant et al., 1987a; Pichavant, 2022), in particular topaz but also Li-micas, albite, quartz and K-feldspar. In addition to a close textural relationship with igneous topaz (Fig. 4a), apatite I commonly hosts inclusions of zircon and columbite-group minerals (Figs. 4e, h). This is consistent with previous petrographic observations of the Beauvoir PRMG supporting its magmatic origin (Rossi et al., 1987; Johan et al., 1988; Wang, 1988). Within the three magmatic units, local accumulations of Li-mica flakes define layering interpreted as magmatic fabrics (Bouchez et al., 1987; Jacquot, 1987) and exhibiting enrichment in magmatic topaz and apatite, as observed in the B2 unit (Figs. 3b, 4a). Magmatic apatite shows a yellow-greenish CL signal, which is generally brighter and more greenish in the B1 unit compared to the B2 and B3 units (Figs. 4c, d, f, g, i). In some cases, it is characterised by a growth zoning, evolving from a dark greenish to yellowish colour in the core to a relatively brighter rim, whereas irregular patches with a brighter yellowish CL signal generally cross-cut this zoning and probably correspond to alteration zones (Figs. 4c, d, f, g, i). All observations collectively confirm the magmatic origin of apatite I and indicate that it may be an early crystallising mineral, contemporaneous with magmatic topaz, within the magmatic paragenetic sequence.

4.1.2. Early hydrothermal apatite

The early hydrothermal stage resulted in the precipitation of an apatite population (type II) occurring in silicified or greisenised Beauvoir granite and pre-existing La Bosse stockwork, in association with mineral assemblages typical of the Beauvoir early hydrothermal event. Apatite II shows heterogeneous distribution, paragenetic context, textural and CL characteristics, leading to the definition of different subtypes (i.e., apatite IIa, IIb, and IIc).

Apatite IIa has been found in association with topaz, quartz and cassiterite within a hydrothermal vein near a contact between the altered Beauvoir granite and the host mica schist in the B3 unit (Fig. 3d). It shows a complex CL texture characterised by dark primary areas partially replaced by brighter secondary zones (Fig. 5b). Cassiterite seems to have preferentially precipitated within these bright-CL secondary zones or at the transition between dark- and bright-CL zones (Figs. 5a, b).

Apatite IIb precipitated with quartz ± muscovite, topaz and accessory wolframite and columbite-group minerals (Figs. 5c, e, g, i), which is a typical mineralogical assemblage of greisen alteration (Pirajno, 2009; Monnier et al., 2019). Apatite IIb is colourless to light blue and has been found as replacement of igneous minerals (Figs. 3f, 5c, e), in particular feldspar and Li-micas, as well as within quartz ± muscovite veins (Figs. 3e, 5g). As previously mentioned, kaolinisation commonly overprints greisen-altered areas, and apatite systematically shows signs of alteration (Charoy et al., 2003; Monnier et al., 2019). This is the case in samples 642.7 and 789.7, where apatite IIb is partially replaced by kaolinite and crandalite-group minerals, in particular goyazite ($SrAl_3(PO_4)_2(OH)_5(H2O)$) (Fig. 5i). Three sub-sets of occurrences of apatite IIb can then be distinguished based on petrographic observations: (i) pervasive greisen alteration (samples 816.5 and 819.5); (ii) greisen vein (sample 704.2); and (iii) greisen alteration overprinted by kaolinite (samples 642.7, 789.7 and 801.0).

The greisen vein selected for further investigation was observed at the contact between the Beauvoir PRMG and a porphyritic enclave, both of which have been intensively greisenised (Fig. 3e). It shows fringes of

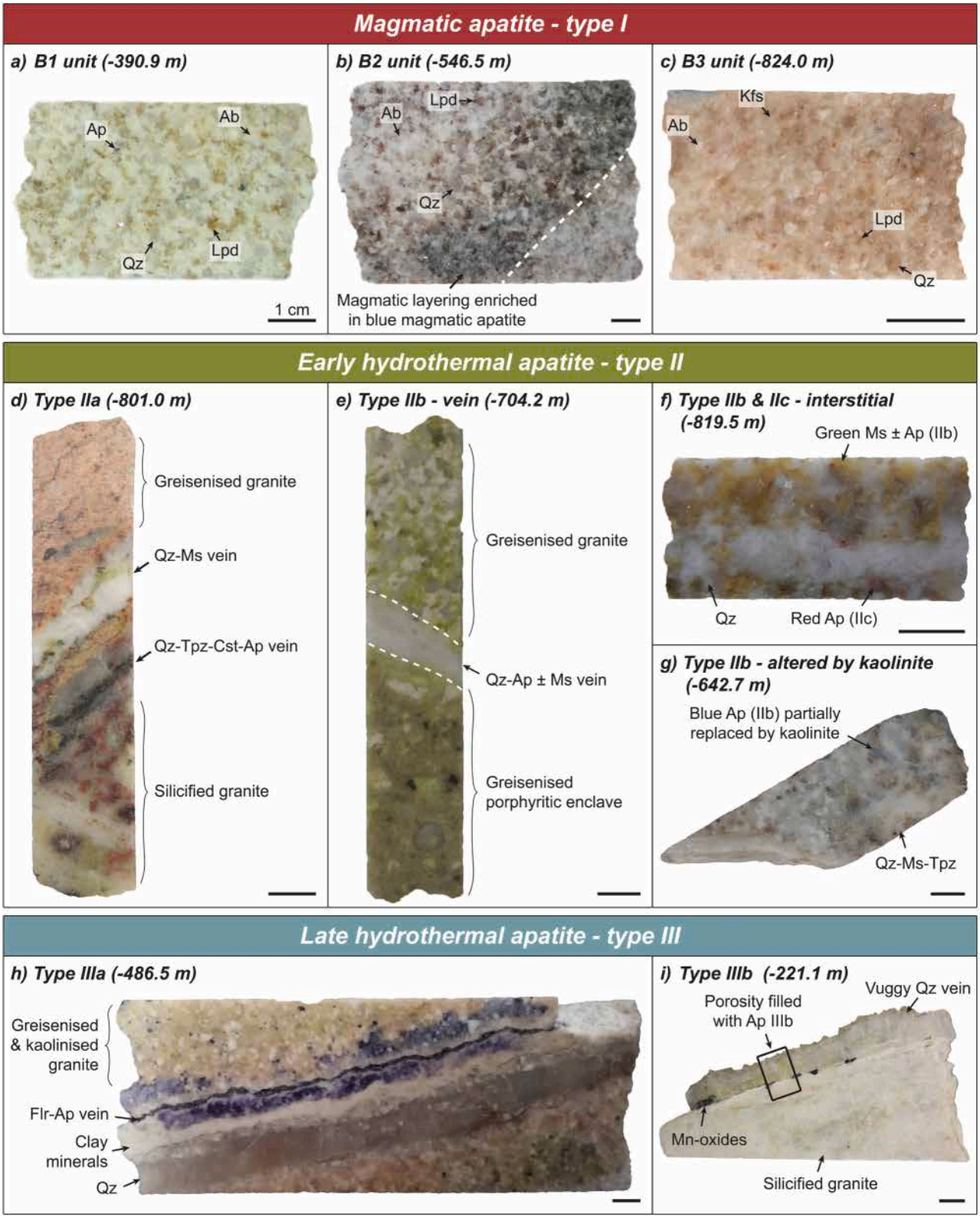

Fig. 3. Selected macrophotographs of investigated samples grouped by hosted apatite type: (a) to (c) Beauvoir granite from the B1, B2 and B3 units, respectively; (d) Quartz-topaz-cassiterite-apatite (type IIa) vein crosscutting the greisenised Beauvoir granite; (e) Quartz-apatite (type IIb) vein at the contact between the greisenised Beauvoir and porphyritic granites; (f) Greisenised Beauvoir granite with interstitial type IIb and IIc apatite; (g) Greisenised Beauvoir granite with apatite IIb partially overprinted by kaolinisation; (h) Composite quartz-fluorite-clay mineral-apatite (type IIIa) vein crosscutting the Beauvoir granite showing signs of both greisenisation and kaolinisation; (i) Vuggy quartz vein exhibiting a Mn-oxides selvedge and late hydrothermal apatite (type IIIb) having precipitated in the vein porosity. Abbreviations follow the IMA conventions compiled by Warr (2021). The scale below each photograph represents 1 cm.

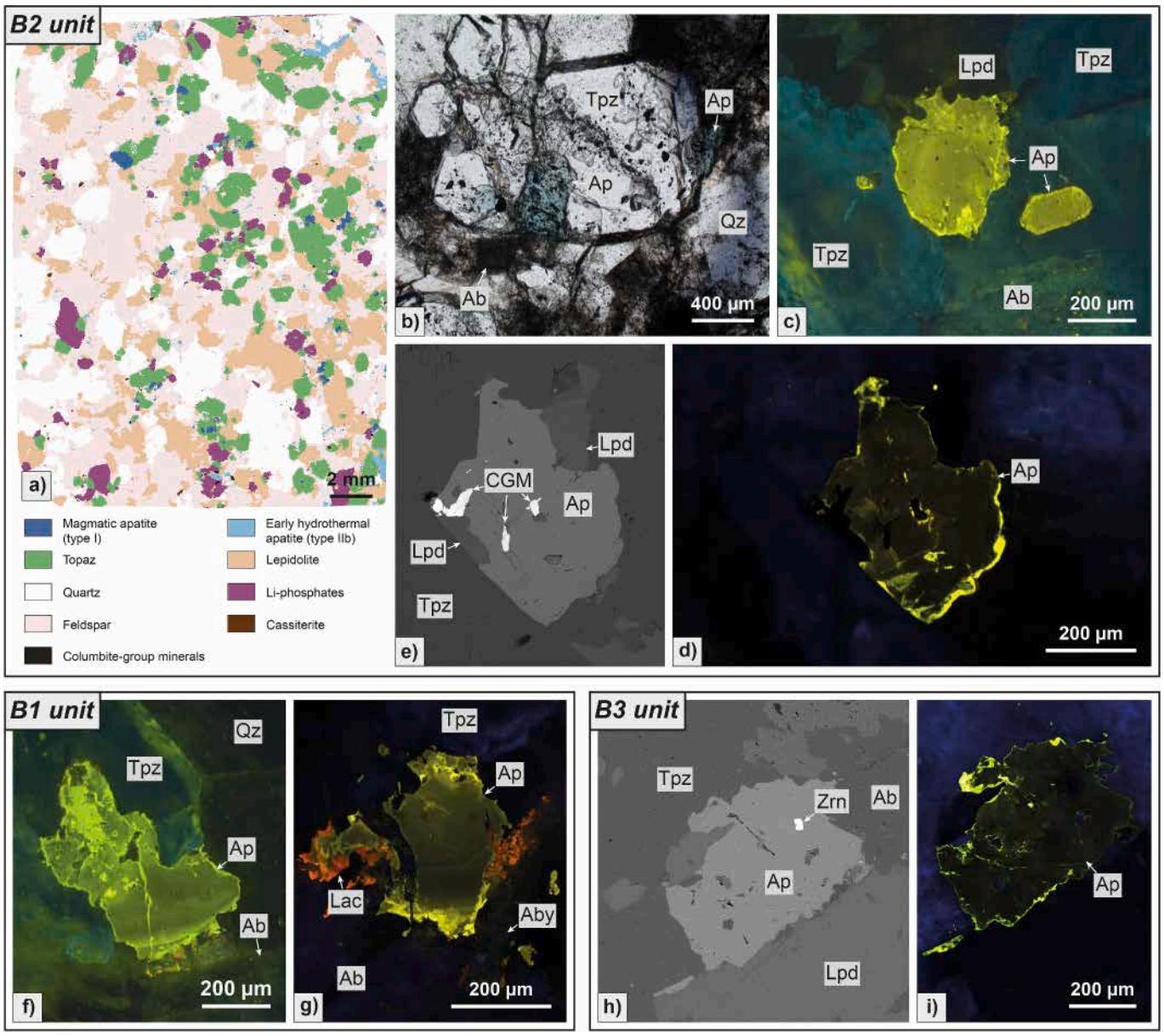

Fig. 4. Petrographic characteristics of magmatic apatite (type I) within the three magmatic units of the Beauvoir PRMG (i.e., B1, B2 and B3). (a) µ-XRF mineralogical map of a typical thin section from the B2 unit (−546.5 m) showing the close spatial relation between magmatic apatite (type I) and topaz, as well as the partial replacement of igneous feldspar and lepidolite by apatite IIb; (b) Thick section microphotograph (plane-polarised light) of blue apatite I; (c-d) CL images of apatite I in the B2 unit; (e) BSE image of apatite I containing inclusions of columbite-group minerals in the B2 unit; (f-g) CL images of apatite I in the B1 unit; (h-i) BSE and CL image of apatite I containing a zircon inclusion in the B3 unit. Abbreviations follow the IMA conventions compiled by Warr (2021), with the exception of CGM: columbite-group minerals. (For interpretation of the references to colour in this figure legend, the reader is referred to the web version of this article.)

sub-euhedral to euhedral apatite, which grew sub-perpendicular to the strike of the quartz vein (Fig. 5g).

The CL signature of apatite IIb is characterised by a brighter and more greenish colour than magmatic apatite found in the B2 and B3 units but is similar to the CL signal of magmatic apatite from the B1 unit (Figs. 5d, f, h, j). Apatite IIb commonly exhibits altered zones, especially in the sample 816.5, and brighter altered areas contain small (*ca.* < 5 µm) monazite inclusions (Figs. 5c, d). This characteristic suggests that the apatite grains underwent metasomatism, possibly leading to the leaching of LREE from apatite lattice and precipitation of secondary monazite (e.g., Harlov, 2015).

Apatite IIc forms anhedral grains replacing Li- and Be-phosphates (i.e., amblygonite-group minerals and herderite, respectively), and greisen-related minerals (i.e., quartz, muscovite and topaz) (Fig. 5k). It shows a CL signature varying from a greenish colour similar to apatite IIb, yet darker, to a distinctive orange colour, especially when it occurs as a replacement of Be-phosphates (Fig. 5l). In that case, apatite IIc also differs from apatite IIb by a red to orange natural colour (Fig. 3f).

4.1.3. Late hydrothermal apatite

Apatite IIIa was observed within a composite and pervasive quartz, muscovite, fluorite and illite vein (Fig. 3h). Igneous lepidolite and a greisen-related quartz-muscovite assemblage are partially replaced by illite (Fig. 6a), which is one of the typical late hydrothermal alteration minerals in the Beauvoir PRMG. Apatite IIIa forms subhedral to euhedral crystals precipitating in close spatial relation with fluorite (Fig. 6a). It shows more yellowish colour but less luminescence in CL images than apatite II (especially apatite IIb) and exhibits growth zoning (Fig. 6b).

Apatite IIIb forms colloform aggregates in the porosity of a vuggy quartz vein exhibiting a Mn-oxides selvedge (Fig. 6f). As apatite IIIa, its CL signature is less luminescent but more yellowish than apatite II

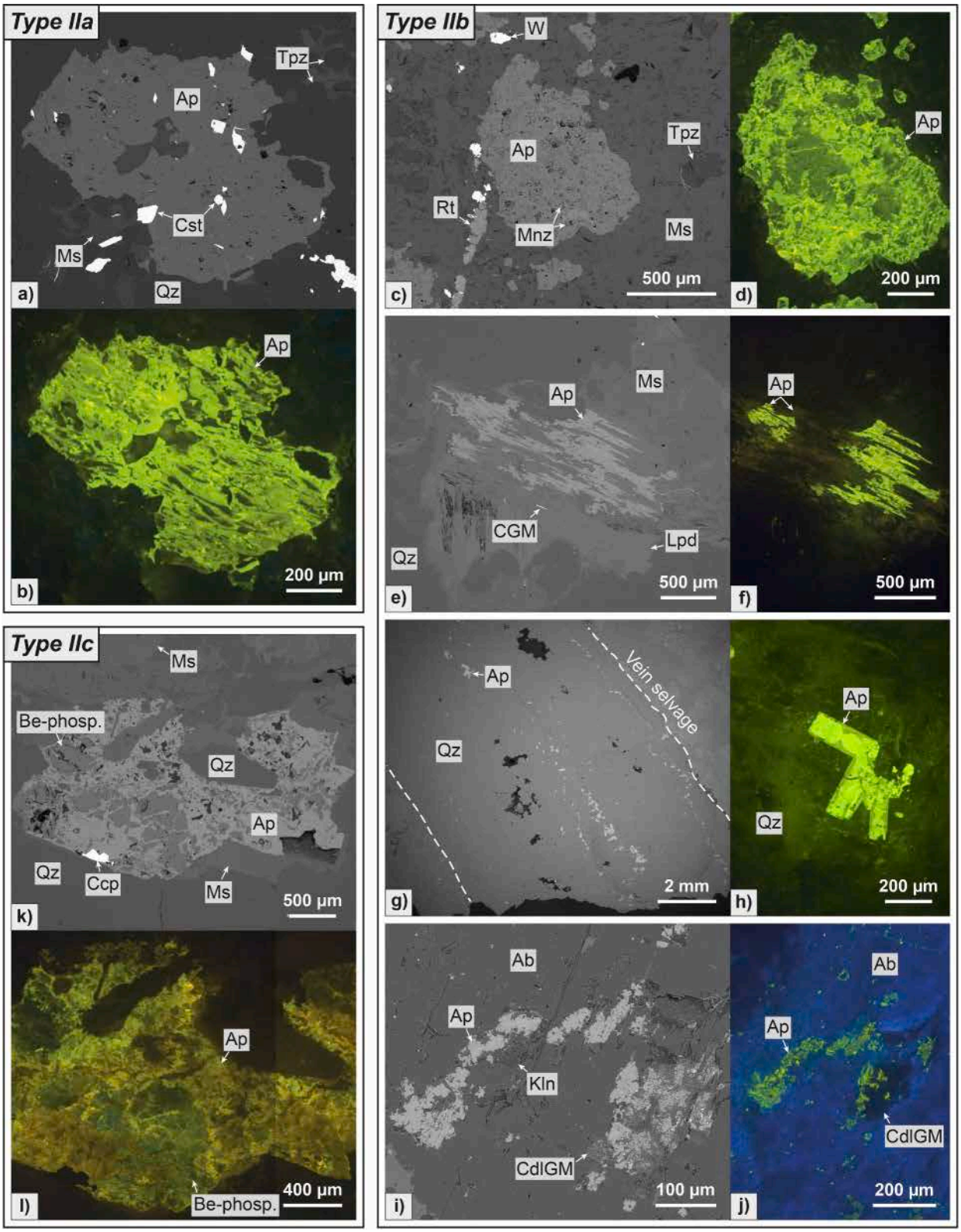

Fig. 5. Petrographic characteristics of early hydrothermal apatite (type II) within the Beauvoir PRMG and host mica schists. (a-b) BSE and CL images of apatite IIa in the B3 unit. Apatite IIa exhibits a complex CL texture characterised by dark primary areas partially overprinted by brighter zones. Cassiterite seems to have preferentially precipitated within bright-CL secondary zones or at the transition between dark- and bright-CL zones. (c-d) BSE and CL images of a greisenised mica schist enclave. Apatite IIb exhibits metasomatism, revealed by the patchy CL texture and the presence of monazite inclusions. (e-f) BSE and CL images of apatite IIb replacing magmatic lepidolite in the B3 unit. (g-h) BSE image of an apatite IIb-bearing greisen vein crosscutting the B2 unit and CL image of hosted apatite. Subeuhedral to euhedral apatite IIb mainly grew sub-perpendicular to the strike of the quartz vein. (i-j) BSE and CL images of apatite IIb partially replaced by kaolinite and crandallite-group minerals in the B3 unit. (k-l) BSE and CL images of apatite IIc replacing Be-phosphates in the B3 unit. Abbreviations follow the IMA conventions compiled by Warr (2021), with the exception of CdlGM: crandallite-group minerals, and CGM: columbite-group minerals.

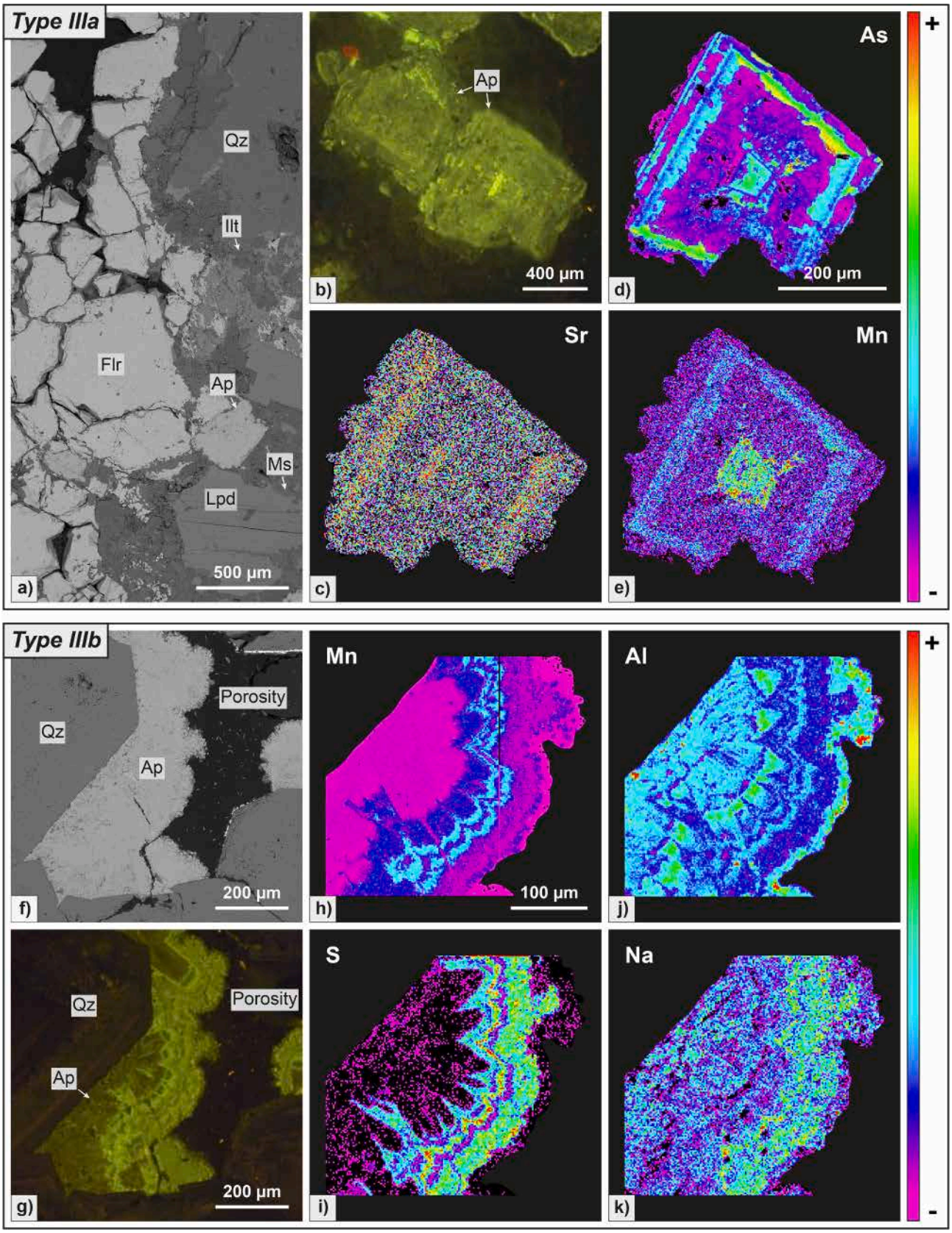

Fig. 6. Petrographic characteristics of late hydrothermal apatite (type III) within the Beauvoir PRMG. (a) BSE image highlighting the close spatial relation between apatite IIIa and fluorite; (b) CL image of apatite IIIa showing a discrete oscillatory zonation; (c-e) WDX element mapping of apatite IIIa revealing As, Sr and Mn relative distribution within the grain; (f-g) BSE and CL images of apatite IIIb forming colloform aggregates precipitating in the porosity of a vuggy quartz vein; (h-k) WDX mapping of Mn, Al, S and Na distributions in apatite IIIb. Abbreviations follow the IMA conventions compiled by Warr (2021).

varying from a dark core to a brighter rim (Fig. 6g).

4.2. Halogens

All apatite occurrences have relatively low Cl content, below 1100 ppm, while most of them show F content above 3.0 wt.% (first quartile value). The vast majority of apatite generations encountered within the Beauvoir PRMG are therefore fluorapatite, with minor (< 1 % of measured compositions) hydroxyapatite identified in the brightest secondary zones of apatite IIa, where the calculated H_2O content reaches up to 1.6 wt.%. Bromine and iodine can substitute for F on the anion site, albeit as trace constituents (Pan and Fleet, 2002; Kusebauch et al., 2015a). Bromine and I contents are low, yet always well above detection limits, and range from 0.2 to 47.2 ppm and from 0.01 to 4.99 ppm, respectively.

4.3. Major and minor elements

P_2O_5 and CaO contents of all apatite generations fall into relatively wide ranges, respectively varying from 36.4 to 44.4 wt.% and 48.7 to 58.6 wt.%, revealing significant substitution on Ca and P sites. Manganese also appears as a major constituent, ranging in concentrations from below the detection limit (i.e., < 0.1 wt.%) to *ca.* 6.5 wt.% MnO. Systematic variations in MnO contents include: (i) as previously emphasised by Wang (1988), apatite I concentrations globally correlate with depth, the average contents decreasing from 5.6 to 4.3 and 1.6 wt.% from the B3, B2 and B1 units, respectively. Such a magmatic differentiation trend, whereby Mn concentration decreases with increasing differentiation without significant changes in Sr and S contents (Fig. 7), differs distinctly from the early hydrothermal apatite II evolution trend, whereby Mn depletion is associated with Sr enrichment; (ii) an overall decrease in MnO content is also observed over time, i.e., from apatite I (mean ~ 3.7 wt.%) to apatite II and III (mean ~ 1.7 wt.% and 0.4 wt.%, respectively).

Apatite I is characterised by high MnO content (Fig. 7), low to moderate Na_2O, SiO_2 and FeO concentrations reaching up to 0.7, 0.2 and 0.6 wt.%, respectively. The chemistry of apatite II reveals a three-step trend (Fig. 7) evolving from: (i) a composition similar to magmatic apatite, dominated by high MnO and low to moderate FeO concentrations. This particular chemistry is associated with dark-CL primary zones of apatite IIa (MnO ~ 2.7–4.8 wt.% and FeO < 0.9 wt.%; Fig. 4b); (ii) a composition differing by a significant Sr enrichment, locally noticeable within the bright-CL secondary zones of apatite IIa (SrO < 0.8 wt.%) and clearly characteristic of apatite IIb. Strontium in apatite IIb reaches up to 4.7 wt.% SrO (mean ~ 1.15 wt.%), with the exception of apatite IIb overprinted by kaolinisation, where Sr was rarely detected through EPMA (< 0.5 wt.%). This SrO enrichment is accompanied by low to moderate FeO contents (< 1.1 wt.%); and finally (iii) a composition characterised by relatively high Na_2O and SO_3 concentrations, that are generally above the detection limit and reach up to 1.4 and 4.1 wt.%, respectively. This is the case in apatite IIb overprinted by kaolinisation and apatite IIc. The simultaneous enrichment in S and Na can be attributed to the following co-substitution on the Ca and P sites (Pan and Fleet, 2002):

$SO_4^{2-} + Na^+ \leftrightarrow PO_4^{3-} + Ca^{2+}$.

A significant Al_2O_3 enrichment is also observed in most early hydrothermal apatite sub-generations, especially in apatite IIb overprinted by kaolinisation, with Al_2O_3 values up to 3.5 wt.%.

Apatite IIIa predominantly differs from the other apatite generations by a relatively important enrichment in As with As_2O_3 concentrations ranging from 0.4 to 5.3 wt.% (mean ~ 1.8 wt.%). The oscillatory zonation highlighted by CL imaging correlates with modifications of the major element chemistry; slightly brighter zones are enriched in As, Mn and Sr and depleted in P compared to the darker areas (Figs. 6c-e). Apatite IIIb exhibits low to moderate SO_3 (<0.1–1.6 wt.%; mean ~ 0.5 wt.%) and Na_2O (0.2–0.6 wt.%; mean ~ 0.4 wt.%) concentrations. Similarly to apatite IIb overprinted by kaolinisation, it is also relatively enriched in Al,

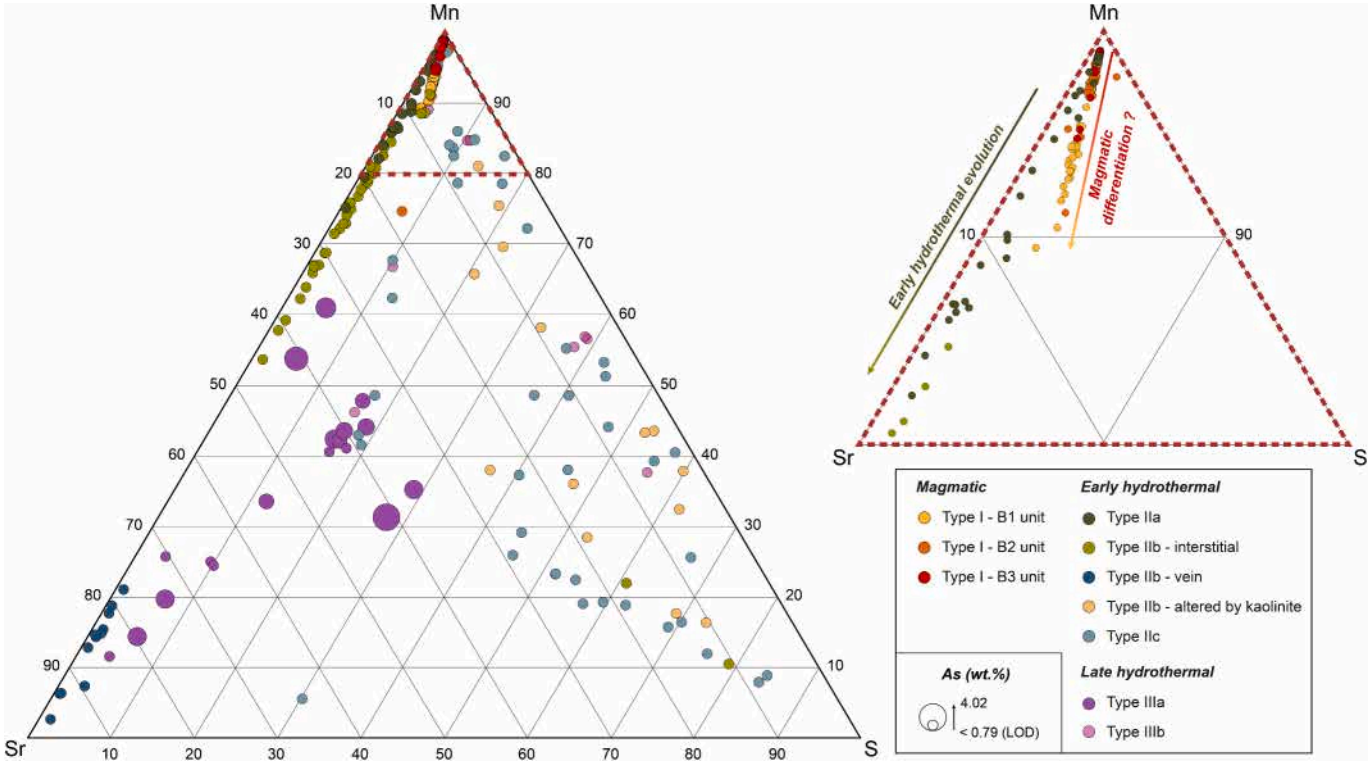

Fig. 7. Sr, S and Mn ternary plot with indication on the As content (circle size) in apatite generations from the Beauvoir PRMG. Magmatic apatite is characterised by an enrichment in Mn. Early hydrothermal apatite varies from Mn-enriched (type IIa), to Sr-rich (type IIb) and S-rich (type IIb altered by kaolinite and type IIc), whereas late hydrothermal apatite is As-enriched for apatite IIIa and S-enriched for apatite IIIb. Data are from EPMA. When an element was not detected at an analysis spot, half of the detection limit was assigned as the concentration.

with Al_2O_3 content varying from below the detection limit to 1.1 wt.% (mean ~ 0.4 wt.%). Apatite IIIb CL luminescence correlates with systematic variations in those elements, the brighter areas being enriched in S, Na and depleted in Al and Mn compared to the darker areas (Figs. 6h-k).

4.4. Trace elements

Apatite generations are associated with distinct trace elements and REE signatures (Figs. 8, 9). Apatite I shows similar trace elements distributions within the three magmatic units, but Sn, Y and total REE concentrations display an overall decreasing trend from the deepest B3 to intermediate B2 and shallowest B1 unit (Figs. 8a, 9a, b). Chondrite-normalised REE patterns of apatite I display LREE enrichment (La_N/Yb_N ~ 2.8–35.7), as well as a strong to moderate negative Eu anomaly (Eu/Eu* ~ 0.01–0.75) (Fig. 9a). Similar features characterise the whole rock REE patterns of the unaltered Beauvoir PRMG (Fig. 9a) (Raimbault et al., 1995). Additionally, apatite I exhibits irregular REE distributions consisting in four curved segments (La-Nd, Pm-Gd, Gd-Ho, and Er-Lu) (Fig. 9a), and designated as lanthanide tetrad effect (Masuda et al., 1987; Bau, 1996; Irber, 1999). The tetrad effect degree (TE_{1-3}) can be quantified for each magmatic unit following Irber (1999), and ranges from 1.05 to 1.73. As estimated TE_{1-3} values essentially exceed 1.1, the tetrad effect degree for magmatic apatite is considered significant (Irber, 1999). Some distinctions are noticeable in the apatite REE patterns of the three magmatic units (Figs. 9a, d). An overall depletion in REEs associated with an increase in La_N/Yb_N is observed from the B3 ($\sum$REE ~ 590–5420 ppm; La_N/Yb_N ~ 2.8–7.7), to the B2 ($\sum$REE ~ 490–3230 ppm; La_N/Yb_N ~ 3.5–8.7), and finally the B1 unit ($\sum$REE ~ 160–1580 ppm; La_N/Yb_N ~ 7.5–35.7). The Eu anomaly is also more pronounced in the B3 and B2 units, exhibiting very similar Eu/Eu* ratios ranging from less than 0.01 to 0.47, in contrast to the B1 unit where the Eu/Eu* ratios vary from 0.27 to 0.75 (Fig. 9a).

Based on the distribution of trace elements in apatite II, two main groups can be identified. The first group, comprising apatite IIa and interstitial apatite IIb, exhibits trace element and REE patterns broadly comparable to those of apatite I, although they are characterised by a distinctive positive Eu anomaly (Eu/Eu* ~ 1.5–5.7; Fig. 9b) and show slightly lower Li, Sn, Th and U concentrations, as well as higher Sr contents (Fig. 8b). The second group includes apatite IIb overprinted by kaolinisation and apatite IIc. By contrast, this group is associated with a relative enrichment in Li, and is depleted in Y, Sn and Th (Fig. 8c). Apatite II from this group is REE-depleted, with total REE content not exceeding 50 ppm (Fig. 9d). REE distributions are characterised by LREE depletion, MREE enrichment, and no distinct Eu anomaly ($0.02 \leq La_N/Yb_N \leq 2.4$) (Fig. 9b). Flat HREE signatures are also observed for apatite IIc, whereas the REE spectra of apatite IIb overprinted by kaolinisation display a more irregular pattern. Those characteristics resemble the whole rock distribution of the kaolinised granite (Fig. 9c). Apatite IIb found within a quartz vein shows an intermediate trace element distribution between the two groups of early hydrothermal crystals, with REE chondrite-normalised spectra similar to the second group (Fig. 9b) but a Sr enrichment similar to the first group (Figs. 8b, c).

Late hydrothermal apatite III comprises some of the most Li-enriched (up to 230 ppm) apatite generations in the Beauvoir PRMG (Fig. 8d). They have variable total REE contents between 2 and 130 ppm, and are globally depleted in REE compared to apatite I (Fig. 9d). Their REE distribution is mainly characterised by a LREE depletion compared to MREE and HREE (La_N/Yb_N ~ 0.06–0.51), and again resembles the whole rock REE pattern of the kaolinised granite (Fig. 9c). Apatite IIIa has modest negative Eu anomaly (Eu/Eu* ~ 0.38–0.71) and its composition notably stands out due to strong Pb enrichment (Fig. 8d).

4.5. Oxygen isotopes

Disregarding the altered zones of the grains, apatite I shows a wide range of O isotopic composition throughout the entire intrusive

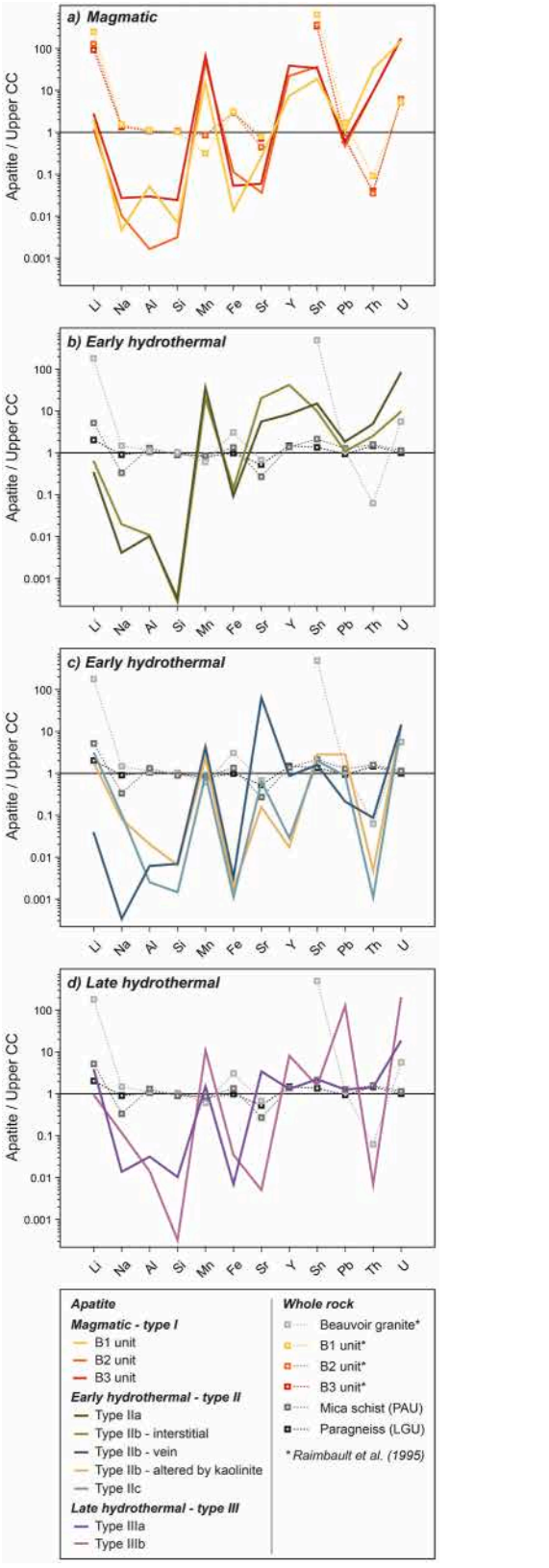

Fig. 8. Trace elements distribution normalised to the upper continental crust (CC) (Rudnick and Gao, 2003) for the distinct apatite generations from the Beauvoir PRMG. Whole rock trace elements distributions for the Beauvoir granite (Raimbault et al., 1995), the Sioule mica schist and paragneiss (Table S9 in Supplementary Material 2) are plotted as references. PAU: Parautochtonous Unit; LGU: Lower Gneiss Unit.

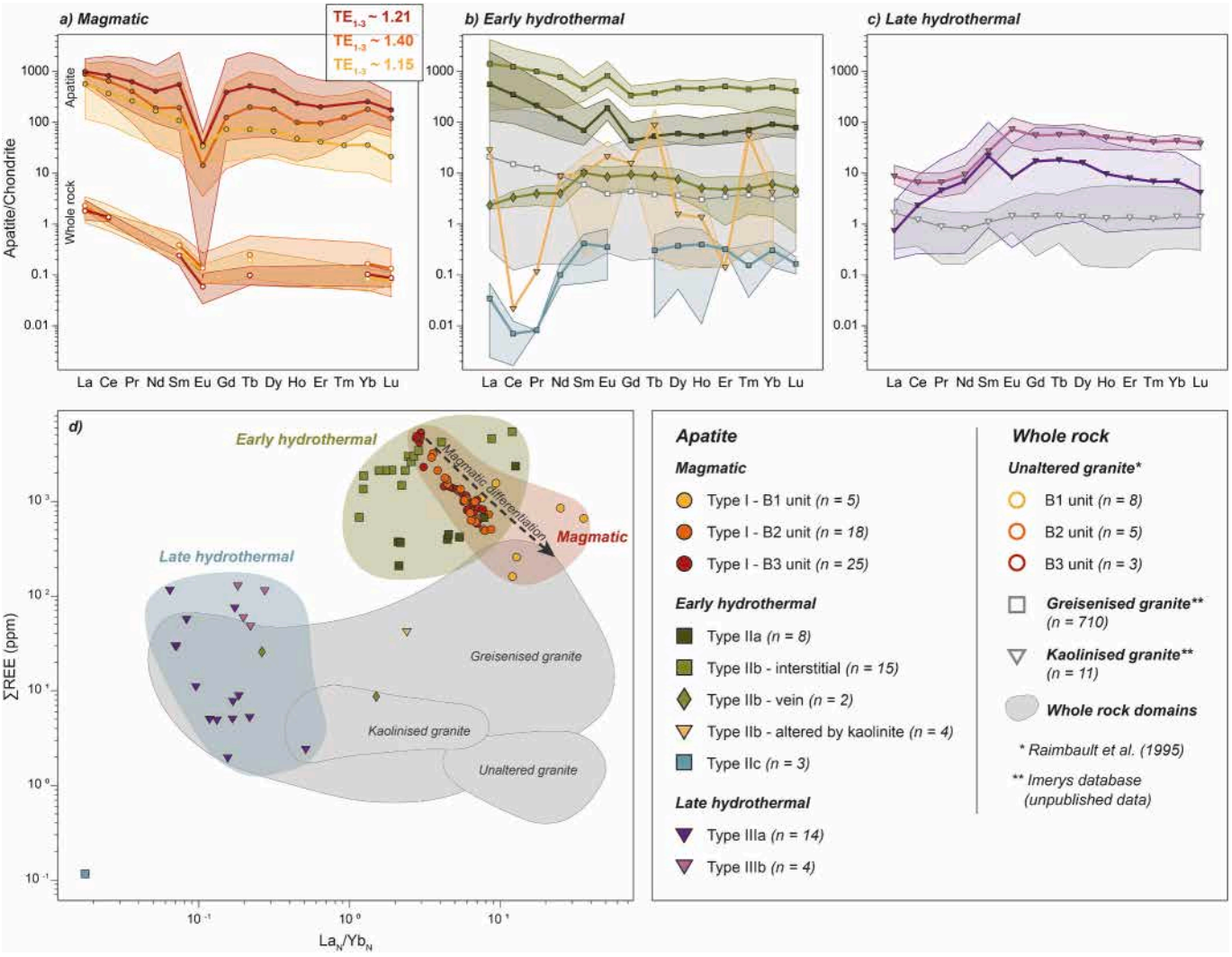

Fig. 9. REE compositions of the different apatite generations from the Beauvoir PRMG: (a-c) Chondrite-normalised REE patterns (Boynton, 1984). The degree of the tetrad effect (TE_{1-3}) was estimated for magmatic apatite following Irber (1999). (d) Total REE content as a function of the La_N/Yb_N ratio within apatite. Whole-rock compositions of samples of unaltered granite (Raimbault et al., 1995) greisenised granite and kaolinised granite (unpublished Imerys database) from the Beauvoir intrusion are shown for comparison.

complex, with $\delta^{18}O$ values varying from 2.0 to 15.8 ‰ (Fig. 10a). This pronounced scatter is predominantly attributed to apatite I analysed in the B1 unit (2.0–15.8 ‰; mean ~ 5.8 ± 0.4 ‰, 2s), whereas less variable $\delta^{18}O$ values are obtained for the B2 (3.9–9.9 ‰; mean ~ 6.1 ± 0.3 ‰) and B3 units (6.3–8.5 ‰; mean ~ 7.7 ± 0.3 ‰). In terms of mean $\delta^{18}O$ values, an overall decrease is observed from the deepest B3 unit (mean ~ 7.7 ± 0.3 ‰) to the intermediate B2 unit (mean ~ 6.1 ± 0.3 ‰) and the shallowest B1 unit (mean ~ 5.8 ± 0.4 ‰; Fig. 10a). Intra-grain variation range in apatite I increases from the B3 unit (*ca.* 1 ‰), to the B2 (0.5–3 ‰) and B1 (4–6 ‰) units. In the B1 unit only, a systematic core to rim trend is noticeable, with brighter-CL magmatic growth rims (Figs. 4f, g) commonly exhibiting heavier O isotopic signatures compared to cores ($\delta^{18}O_{rim}$ values up to 3 ‰ higher).

The $\delta^{18}O$ values of altered zones observed in apatite I fall into a wide range of −3.7 to 8.3 ‰ in the B1 unit and of −14.8 to 12.2 ‰ in the B2 unit. A single value of 5.2 ± 0.3 ‰ has been obtained for an altered domain of apatite I from the B3 unit. Altered zones (mean ~ 3.7 ± 0.4 ‰ and 4.9 ± 0.3 ‰ for the B1 and B2 units, respectively) overall show lower $\delta^{18}O$ values compared to unaltered magmatic micro-domains.

Apatite II is associated with significantly scattered O isotopic compositions, ranging from −6.7 to 7.5 ‰ for apatite IIa, −8.8 to 13.4 ‰ for apatite IIb, and −7.5 to 12.5 ‰ for apatite IIc (Figs. 10b, c). Among all analysed apatite IIb, two apparent end-members can be distinguished: (i) the quartz-apatite greisen vein (sample 704.2), for which $\delta^{18}O$ fall into a narrow negative range of −3.3 to −1.0 ‰ (mean ~ −2.1 ± 0.2 ‰); (ii) the greisen-altered zones, with apatite being partially replaced by kaolinite and crandallite-groupe minerals (samples 642.7, 789.7 and 801.0), in which the O isotopic signature of apatite is notably heavier (−1.2 to 13.4 ‰; mean ~ 10.8 ± 0.2 ‰). The two other samples (i.e., 816.5 and 819.5) are representative of pervasive greisen alteration and exhibit significant scatter in O isotopic compositions between these two end-members, their $\delta^{18}O$ values ranging from −3.7 to 8.6 ‰ (mean ~ 5.3 ± 0.2 ‰) and from −8.8 to 12.7 ‰ (mean ~ −0.8 ± 0.2 ‰), respectively.

A noticeable systematics exists between O isotopic signature, elemental chemistry and apatite CL-signal, when the grain distinctly exhibits darker-CL primary replaced by brighter-CL secondary zones, as it is the case for apatite IIa (Fig. 5b) and apatite IIb from sample 816.5 (Fig. 5d). The darker-CL primary zones tend to exhibit heavier O isotopic

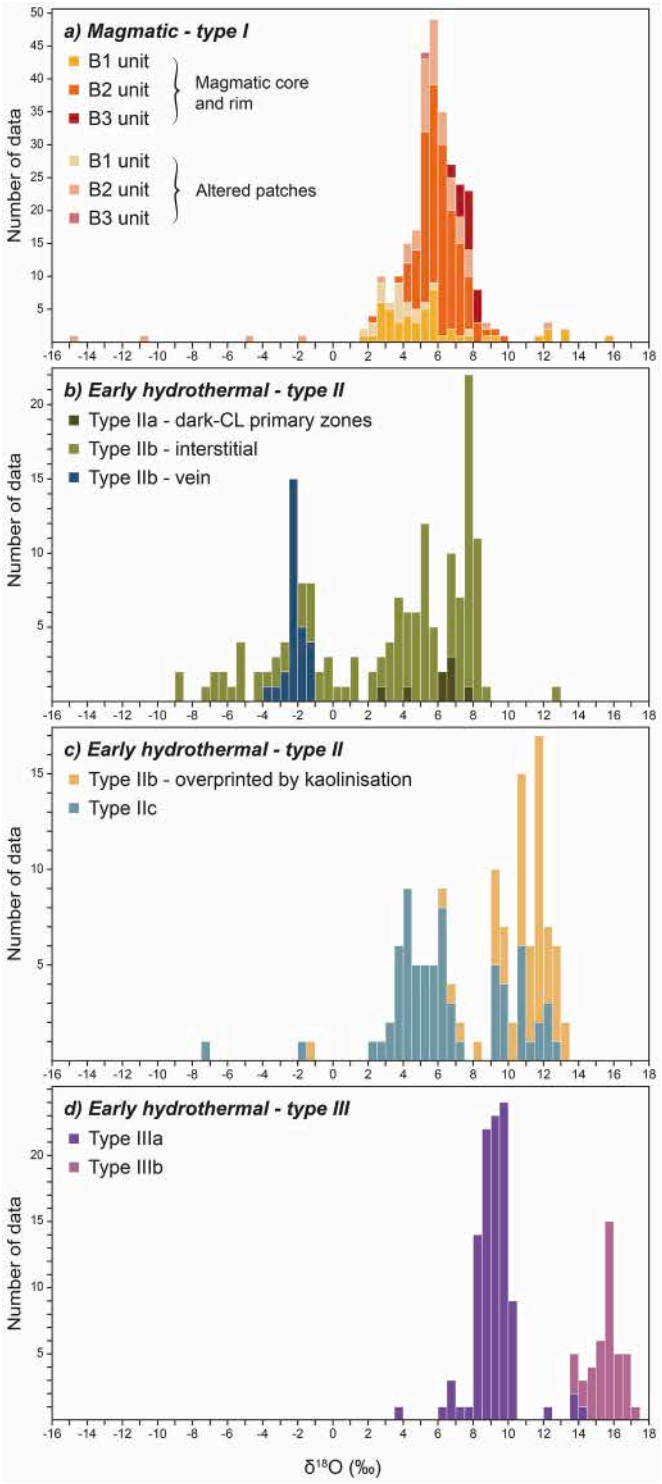

Fig. 10. O isotopic composition of the distinct apatite generations from the Beauvoir PRMG system: (a) Magmatic generation; (b-c) Early hydrothermal generations; (d) Late hydrothermal generations.

signatures, higher Mn and total REE contents and lower Sr concentrations than the brighter-CL micro-domains. For instance, dark-CL primary areas within apatite IIa exhibit O isotopic compositions of 2.7 to 7.5 ‰ (mean ~ 5.9 ± 0.2 ‰), average MnO and Sn concentrations of 4.1 wt.% and 43 ppm, respectively, an average REE total content of 870 ppm and SrO content essentially below the detection limit (i.e., < 0.1 wt.%). In contrast, bright-CL secondary areas are characterised by a distinctly lighter O isotopic signature, with $\delta^{18}O$ values ranging from −6.7 to 3.7 ‰ (mean ~ −3.5 ± 0.3 ‰), lower MnO (mean ~ 3.0 wt.%), Sn (mean ~ 3 ppm) and total REE (mean ~ 320 ppm) concentrations and a higher SrO (mean ~ 0.3 wt.%) content (see sections 5.1 and 5.4 for further discussion).

The O isotopic signature of apatite III is typically heavy (Fig. 10d). Apatite IIIa shows scattered $\delta^{18}O$ values ranging from 3.4 to 14.4 ‰ (mean ~ 9.2 ± 0.2 ‰), while apatite IIIb has the heaviest O isotopic signature, with $\delta^{18}O$ values varying between 13.6 and 17.0 ‰ (mean ~ 15.6 ± 0.2 ‰).

4.6. U-Pb geochronology

Tera-Wasserburg diagrams for the main supra- and sub-solidus stages (i.e., magmatic, early hydrothermal and late hydrothermal stages) are presented in Fig. 11, and additional plots for the distinct magmatic and early hydrothermal apatite sub-generations are presented in Fig. S2 (Supplementary Material 1). The U content of the different apatite generations from the Beauvoir PRMG shows a wide range, from less than 1 ppm to *ca.* 1000 ppm. Apatite I is relatively enriched in U (*ca.* 140–790 ppm) compared to typical apatite from other felsic igneous rocks (*ca.* 1–100 ppm; O'Sullivan et al., 2020). Apatite II shows lower U concentrations (*ca.* 0.04–140 ppm), except for the dark-CL primary zones of apatite IIa and for apatite IIb overprinted by kaolinisation, which yield similar values to apatite I. Moderate to high U concentrations characterise apatite III, with U content reaching up to *ca.* 1000 ppm in apatite IIIb.

Apatite I from the B1, B2 and B3 units plot relatively close to the concordia curve in the Tera-Wasserburg diagram due to their high U and relatively low initial Pb contents (Fig. 11a). Lower intercept dates of 315.0 ± 6.8 Ma ($n = 16$; MSWD = 1.7), 312.0 ± 18.3 Ma ($n = 23$; MSWD = 1.2) and 313.6 ± 5.0 Ma ($n = 22$; MSWD = 1.3) obtained for the B1, B2 and B3 units, respectively, are identical within uncertainty (Figs. S2a, b, c in Supplementary Material 1). Apatite I from the B1 unit is characterised by the highest $^{207}Pb/^{206}Pb$ and lowest $^{238}U/^{206}Pb$ ratios, reflecting a relative enrichment in initial Pb (Fig. S2a). The combination of all data for magmatic apatite define a lower intercept date of 314.6 ± 4.7 Ma ($n = 61$; MSWD = 2.2) and the discordia line returns an initial $^{207}Pb/^{206}Pb_{(i)}$ ratio of 0.80 ± 0.02, reasonably close to the model isotopic composition of terrestrial lead at 310 Ma (i.e., $^{207}Pb/^{206}Pb_{(310\ Ma)} \sim 0.86$; Stacey and Kramers, 1975) (Fig. 11a).

Three subsets can be distinguished within the early hydrothermal generation (i.e., apatite IIa, IIb and IIc). Data from apatite IIa yield a lower intercept date of 314.3 ± 5.5 Ma ($n = 27$; MSWD = 4.0) and a $^{207}Pb/^{206}Pb_{(i)}$ composition of 0.83 ± 0.01, which is similar to the common Pb value defined by magmatic apatite (Fig. 11b). A significant spread along the discordia is observed, with bright-CL secondary zones enriched in common Pb compared to the darker-CL primary zones. Three samples have been analysed for apatite IIb, and represent: (i) pervasive greisen alteration, (ii) vein formation during the greisenisation episode, and (iii) greisen-alteration overprinted by kaolinisation. Data from apatite IIb associated with pervasive alteration define a relatively well-constrained isochron with a lower intercept date of 315.8 ± 7.2 Ma ($n = 54$; $^{207}Pb/^{206}Pb_{(i)} = 0.85 \pm 0.01$; MSWD = 2; Fig. S2d in Supplementary Material 1), whereas U-Pb analyses of apatite from the greisen-related vein result in an imprecise date of 301.0 ± 20.2 Ma ($n = 35$; $^{207}Pb/^{206}Pb_{(i)} = 0.84 \pm 0.01$; MSWD = 2.3; Fig. S2e in Supplementary Material 1). Two clusters in the Tera-Wasserburg plot can be identified from the analysis of apatite IIb overprinted by kaolinisation, especially differing by their U content (Fig. S2f in Supplementary Material 1). No date can be unambiguously assigned on the basis of these data, given that the two clusters are sharply separated and appear to belong to distinct discordia trends. As all apatite IIb, except for

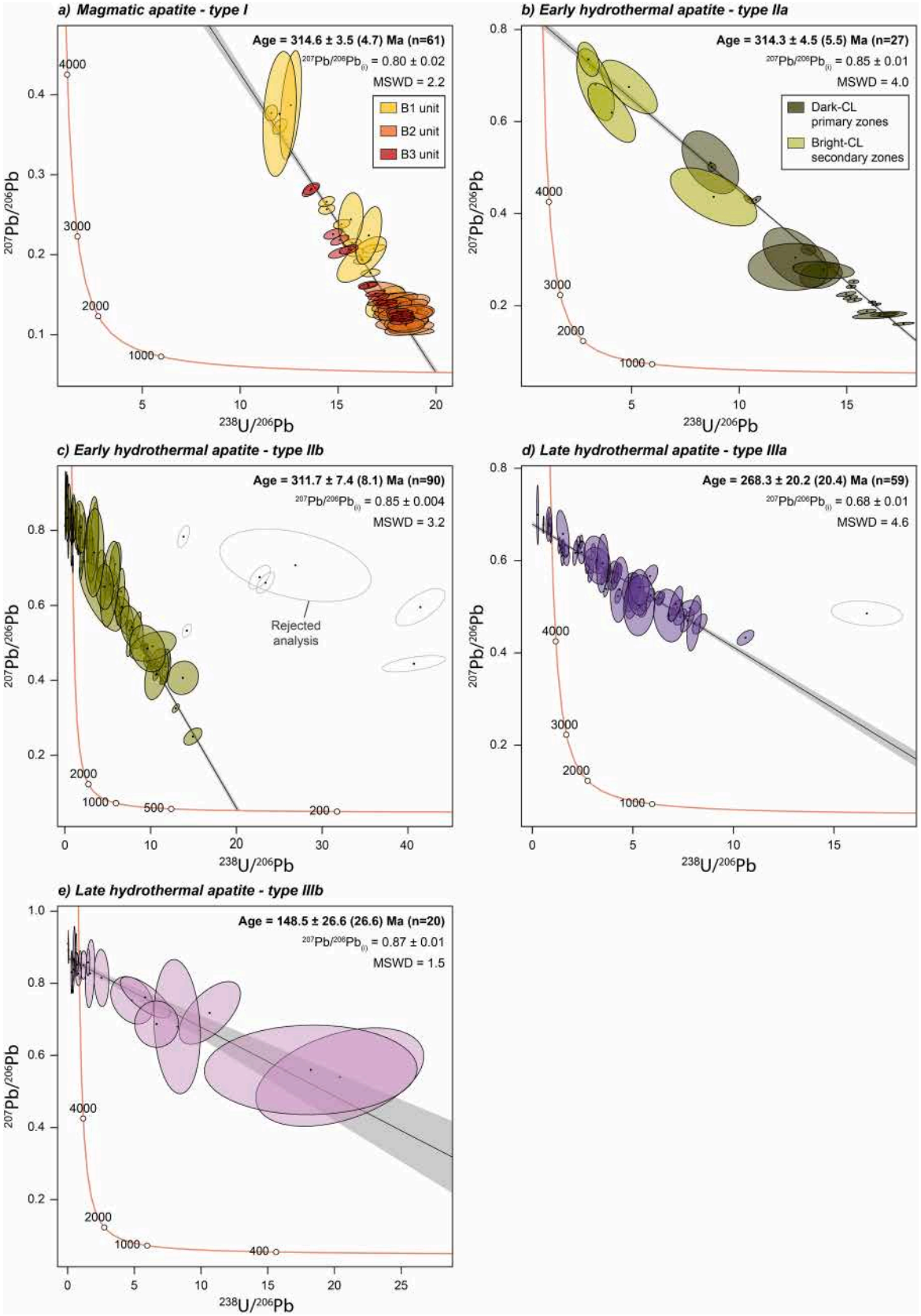

Fig. 11. Tera-Wasserburg diagrams for the different apatite generations from the Beauvoir PRMG. (a) Magmatic apatite; (b-c) Early hydrothermal apatite – types IIa and IIb, respectively; (d-e) Late hydrothermal apatite – types IIIa and IIIb, respectively. Ellipses and age uncertainties are reported at the 2-sigma level. The first uncertainty indicated corresponds to the analytical uncertainty with overdispersion, whilst the second one in brackets takes into account interlaboratory reproducibility (± 1 %).

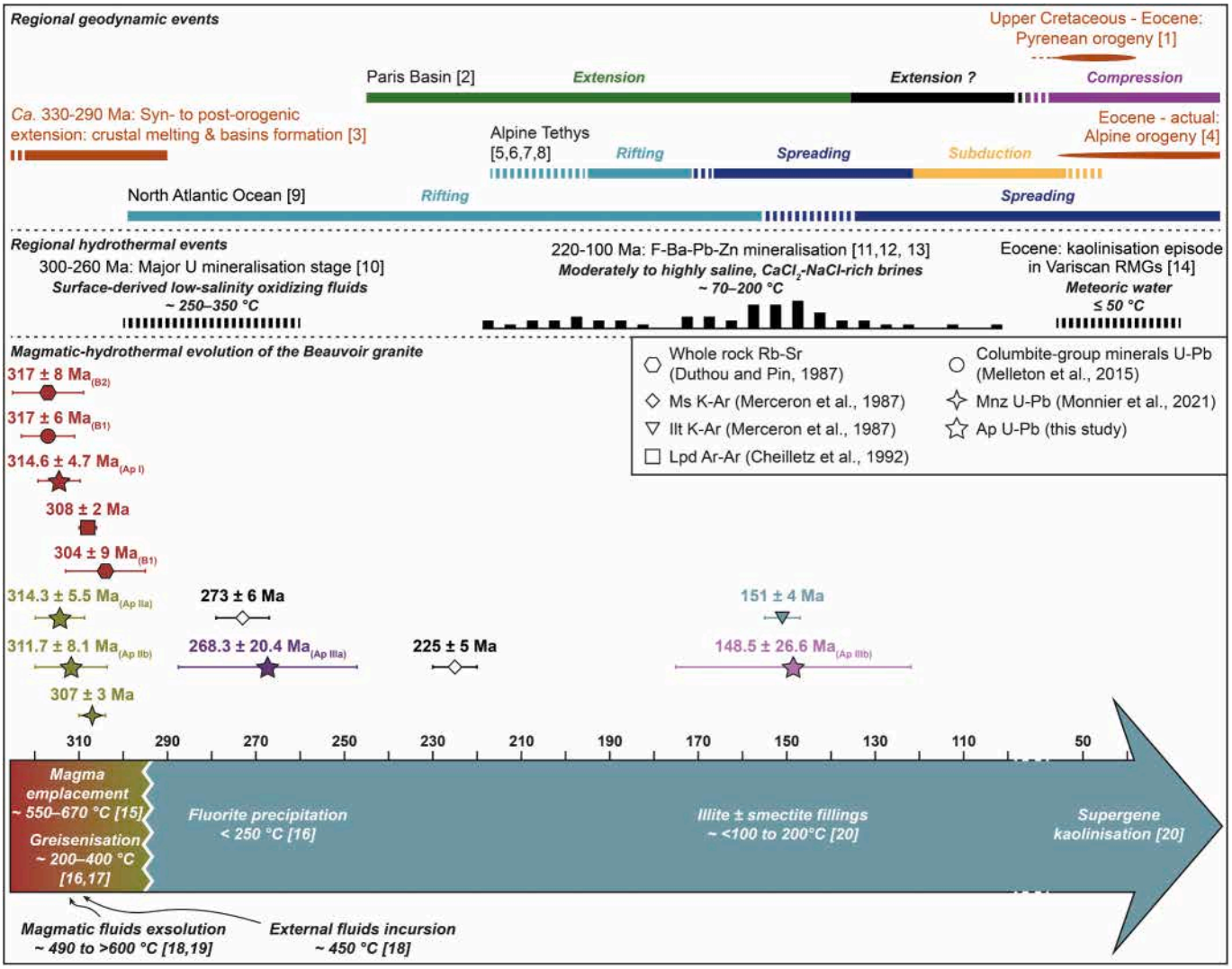

Fig. 12. Chronology of the different magmatic and hydrothermal events that occurred in the Beauvoir PRMG between 315 Ma and the Eocene in parallel with the main regional geodynamic and hydrothermal events. All ages are reported with uncertainties at the 2-sigma level. Ages obtained by Rb-Sr dating of whole rock samples from the B1 and B2 units (Duthou and Pin, 1987) were recalculated using the ^{87}Rb decay constant of Villa et al. (2015). The F-Ba-Pb-Zn mineralisation event is from a compilation of geochronological data for the FMC and adjacent regions (i.e., Poitou High, Morvan and Vendée). The histogram represents only central ages, disregarding associated uncertainties. [1] Rosenbaum et al. (2002); [2] Guillocheau et al. (2000); [3] Vanderhaeghe et al. (2020); [4] Ford and Lickorish (2004); [5] Stampfli et al. (2002); [6] Handy et al. (2010); [7] Bellahsen et al. (2014); [8] Van Hinsbergen et al. (2020); [9] Angrand and Mouthereau (2021); [10] Ballouard et al. (2017) and references therein; [11] Cathelineau et al. (2012) and references therein; [12] Gigoux (2015) and references therein; [13] Bouat et al. (2023); [14] Gaudin et al. (2015) and references therein; [15] Pichavant (2022); [16] Merceron et al. (1992); [17] Monnier et al. (2020); [18] Aïssa et al. (1987); [19] Harlaux et al. (2017); [20] Merceron et al. (1987).

apatite IIb overprinted by kaolinisation, produce similar U-Pb dates and $^{207}Pb/^{206}Pb_{(i)}$ compositions within uncertainty, this subset is presumed to have precipitated over a relatively short period of time. Therefore, all data, except for apatite IIb overprinted by kaolinisation, were pooled to obtain an overall date of 311.7 ± 8.1 Ma, with a $^{207}Pb/^{206}Pb_{(i)}$ ratio of 0.85 ± 0.004 (n = 90; MSWD = 3.2) (Fig. 11c). Due to the lack of exploitable signals, no date could be obtained for apatite IIc.

Finally, U-Pb data from the two late hydrothermal generations yield distinct dates of 268.3 ± 20.4 Ma (n = 59; MSWD = 4.6) for fluorite-related apatite (apatite IIIa; Fig. 11d) and of 148.5 ± 26.6 Ma (n = 20; MSWD = 1.5) for colloform apatite occurring in the porosity of a quartz vein with a Mn-oxide selvedge (apatite IIIb; Fig. 11e). While both apatite subsets show a dominant common Pb proportion of total Pb, which results in imprecise dates, they are still significantly younger than the Beauvoir PRMG.

5. Discussion

5.1. Timing of magmatic and hydrothermal episodes for the Beauvoir peraluminous rare-metal granite

The Beauvoir PRGM is marked by four major apatite generations, which are respectively characteristic of the magmatic, early hydrothermal and the two late hydrothermal stages. Based on textural evidence, apatite I is related to the crystallisation of the Beauvoir magmas and represents an early mineral within the magmatic paragenetic sequence (section 4.1; Fig. 2). Analyses of apatite I from the three main magmatic units together yield an age of 314.6 ± 4.7 Ma (Fig. 11a). Considering the magmatic origin of apatite I, this date likely represents the crystallisation age of the Beauvoir PRMG, which is consistent with previous studies that suggested emplacement ages identical within

uncertainties, i.e., 304 ± 9 Ma and 317 ± 8 Ma by Rb-Sr dating of whole rock samples from the B1 and B2 units, respectively (Duthou and Pin, 1987; ages recalculated with the ^{87}Rb decay constant of Villa et al., 2015), 308 ± 2 Ma by ^{40}Ar-^{39}Ar dating of lepidolite (Cheilletz et al., 1992) and 317 ± 8 Ma by applying the U-Pb method on columbite-group minerals from the B1 unit (Melleton et al., 2015) (Fig. 12). From 325 to 310 Ma, the axial part of the Variscan belt experienced lithospheric extension, leading to crustal melting and widespread granitic magmatism (e.g., Vanderhaeghe et al., 2020; Schulmann et al., 2022). The emplacement of the Beauvoir PRMG at *ca.* 315–310 Ma marks the end of this event. In the FMC, it is contemporaneous with the emplacement of other PRMGs and pegmatites, as well as peraluminous leucogranite-related W ± Sn hydrothermal deposits, within transcurrent or extensional tectonic structures (Cuney et al., 2002; Bouchot et al., 2005; Melleton et al., 2015; Harlaux et al., 2018; Carr et al., 2021; Monnier et al., 2021).

Early hydrothermal apatite II and late hydrothermal apatite III generally display intergrowth textures with hydrothermal assemblages and occur as pervasively distributed alteration minerals, or are found within veins. Those characteristics supports their precipitation from hydrothermal fluids. The early hydrothermal generation is associated with quartz ± muscovite ± topaz ± cassiterite and is characteristic of greisen alteration (Monnier et al., 2019) (Fig. 2). The complex and irregular textures in early hydrothermal apatite observed in CL (Figs. 5b, d, f, j) suggest dissolution-reprecipitation processes during metasomatic alteration. In some apatite II occurrences, grains distinctly exhibit darker-CL primary replaced by brighter-CL secondary zones, which correlate with systematic changes in elemental and O-isotopic compositions (section 4.5). Consequently, the overprint of the initial chemistry appears predominantly restricted to brighter-CL altered zones, whereas the darker-CL unaltered zones potentially preserve the signature from the primary fluid circulation. This modification in apatite chemistry is also reflected in the U-Pb data, as the altered zones are typically characterised by higher proportion of initial Pb relative to radiogenic Pb compared to primary zones. (e.g., Fig. 11b for apatite IIa). Yet, for most samples, U-Pb analyses from the altered and unaltered zones lie along the same trend between initial and radiogenic Pb, indicating that they formed within a timespan shorter than the obtained uncertainties (2s = 5.5 and 8.1 Ma for apatite IIa and IIb, respectively). Considering that the Beauvoir magmatic-hydrothermal system probably cooled over a time scale of the order of *ca.* 10^4 years due to the small size of the intrusion (~ 0.21 km^3; Raimbault et al., 1995) and its shallow emplacement (~ 3 km; Cuney et al., 1992) (e.g., Coulson et al., 2002; Ingebritsen et al., 2010; Andersen and Weis, 2020), apatite U-Pb dating does not allow to assert that metasomatic processes recorded in most early hydrothermal apatite (apatite II) are temporally linked to greisen alteration. However, petrographic observations support a genetic link between the precipitation of apatite II and greisenisation. The textural and compositional variability observed in early hydrothermal apatite likely results from changes in greisenising fluids properties (e.g., temperature, composition), leading to destabilisation and (re-)crystallisation of apatite.

The two main ages determined for the early hydrothermal stage (i.e., 314.3 ± 5.5 Ma for apatite IIa and 311.7 ± 8.1 Ma for apatite IIb; Fig. 12) are consistent with a preliminary age of 307 ± 3 Ma for the greisenisation event related to the Beauvoir PRMG emplacement, obtained by U-Pb dating of monazite from the alteration halo of a quartz vein formed from greisen-related fluids within the Echassières complex (Monnier et al., 2021). These ages are indistinguishable within uncertainty from those of magmatic apatite and, conversely, significantly older than the Permian-Triassic estimate derived from K-Ar dating of muscovite (273 ± 6 Ma for pervasive greisen alteration and 225 ± 5 Ma for the formation of greisen-related veins; Merceron et al., 1987) (Fig. 12). Therefore, our new geochronological results support a strong temporal and genetic relation between greisen alteration and Beauvoir PRMG magma emplacement, as proposed by many authors for the Beauvoir PRMG (e.g., Cuney et al., 1992; Monnier et al., 2020). Such temporal relationship between granite intrusion and greisen alteration has been documented for other similar systems (e.g., Breiter et al., 2017; Launay et al., 2021).

To date, there is limited data available to constrain the timing of the fluorite mineralisation episode within the Beauvoir intrusion. An external origin of mineralising fluids has been emphasised based on fluorite REE patterns (Raimbault, 1988). Previous authors also suggested that a conceivable origin may lie in the widespread hydrothermal event affecting western Europe and resulting in the formation of large veins and stratiform F-Ba-Pb-Zn ore deposits (Merceron et al., 1987; Raimbault, 1988). Although the genesis of these hydrothermal deposits occurred over an extensive period spanning from the Early Jurassic to the Early Cretaceous (*ca.* 210–100 Ma; Joseph et al., 1973; Baubron et al., 1980; Soule de Lafont and Lhegu, 1980; Davaine, 1980; Nigon, 1988; Sizaret et al., 2009; Boiron et al., 2010; Cathelineau et al., 2012; Gigoux et al., 2015; Lenoir et al., 2023), the geochronological data available for the FMC, the Morvan, Vendée and Poitou regions (Fig. 1a) emphasises a well-documented F mineralisation period between *ca.* 165 and 140 Ma (Fig. 12). A similar observation has been made by Burisch et al. (2022) on a broader scale, highlighting a major F deposition episode between *ca.* 185 and 140 Ma when taking into account most of Europe's major fluorite provinces. Considering the close textural relation between fluorite and apatite IIIa in the Beauvoir PRMG, fluorite precipitation likely occurred around 268.3 ± 20.4 Ma (Fig. 12). Despite the large uncertainty of this age, it significantly contrasts with previous assumptions suggesting a Liassic mineralisation event. Nevertheless, it supports its temporal dissociation with the magma emplacement and related early hydrothermal stage (*ca.* 305–315 Ma) (Fig. 12), thus necessitating the involvement of external (non-magmatic-hydrothermal) fluid circulation.

The Variscan belt (e.g., Bohemian Massif, Black Forest, Massif Central and Armorican Massif) is characterised by important hydrothermal uranium mineralisation, mostly deposited between 300 and 260 Ma (e.g., Wendt et al., 1979; Carl et al., 1983; Eikenberg, 1988; Cathelineau et al., 1990; Hofmann and Eikenberg, 1991; Kříbek et al., 2009; Velichkin and Vlasov, 2011; Ballouard et al., 2018) (Fig. 12). The mobilisation of U from fertile peraluminous leucogranites, syntectonically emplaced along extensional faults or strike-slip shear zones during the late Carboniferous, derives from sub-solidus alteration via surface-derived low-salinity oxidising fluids, with possible contribution of Permian basin-derived fluids, at temperatures ranging from *ca.* 250 to 350 °C (e.g., Cathelineau, 1982; Turpin et al., 1990b; Barsukov et al., 2006; Kříbek et al., 2009; Dolníček et al., 2014; Ballouard et al., 2017; Dusséaux et al., 2022). Rare occurrences of U-rich fluorite, also referred to as antozonite, have been documented in late Carboniferous to Permian U deposits, such as the Retail mineralised vein (Vendée; Ruhlmann et al., 1980), the Ecarpière deposit (Vendée; Sarcia et al., 1958), or the Bauzot mineralisation (Burgundy; Carrat, 1956). Fluorine mineralisation recognised within the Beauvoir intrusion is proposed to be related to this widespread hydrothermal event, thus recording brittle reactivation of Variscan shear zones during the Permian post-orogenic evolution (e.g., Cathelineau et al., 1990; Ballouard et al., 2017, 2018).

No clear intergrowth texture has been observed between apatite IIIb and other minerals. However, precipitation of colloform apatite IIIb in the porosity of a vuggy quartz vein exhibiting a Mn-oxides selvedge suggests a late precipitation, Fe- and Mn-oxides being thought to derive from weathering during the late hydrothermal evolution of the Beauvoir PRMG (Merceron et al., 1987, 1992; Monnier et al., 2019). Supergene kaolinisation, known to affect Variscan RMGs during the Eocene (e.g., Estéoule-Choux, 1967; Gaudin et al., 2015), represents the last pervasive alteration episode of the Beauvoir PRMG (Merceron et al., 1987). The main P-bearing mineral precipitating during supergene kaolinisation of the Beauvoir PRMG consists of crandallite-group minerals typically replacing greisen-related apatite (Figs. 5i, j; Monnier et al., 2019), thus precipitation of apatite IIIb most likely predates this event. Apatite IIIb

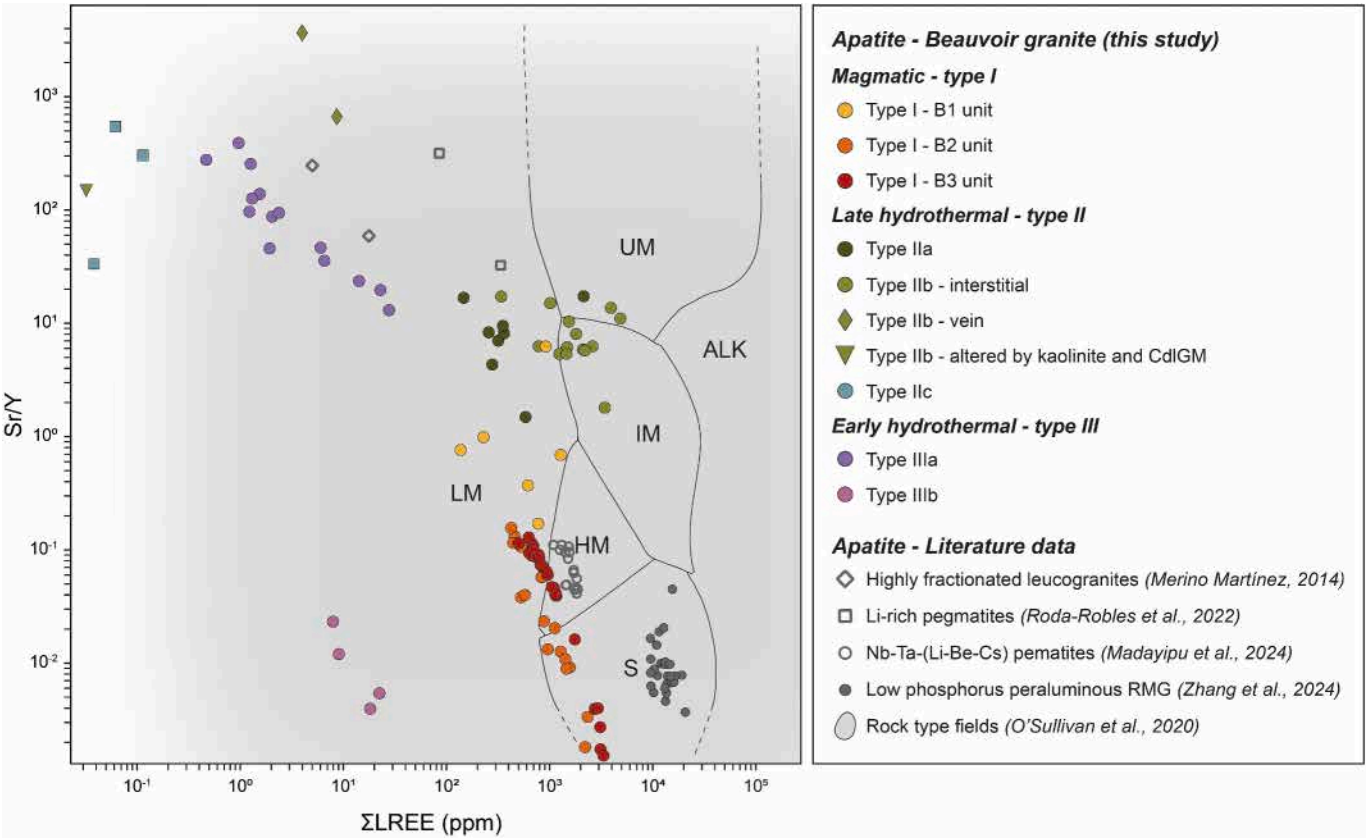

Fig. 13. Discriminant Sr/Y vs ∑LREE plot after O'Sullivan et al. (2020) to decipher the nature of the parent rock from apatite chemistry. Abbreviations for groups: ALK = alkali-rich igneous rocks; IM = mafic I-type granitoids and mafic igneous rocks; LM = low- and medium-grade metamorphic and metasomatic; HM = partial-melts/leucosomes/high-grade metamorphic; S = S-type granitoids and high aluminium saturation index (ASI) 'felsic' I-types; UM = ultramafic rocks including carbonatites, lherzolites and pyroxenites.

yields a lower intercept age of 148.5 ± 26.6 Ma, which, albeit imprecise, overlaps the precipitation age of illite within the Beauvoir PRMG estimated at 151 ± 4 Ma (K-Ar on illite; Merceron et al., 1987) (Fig. 12). As previously mentioned, F-Ba-Pb-Zn ore deposits formed across Western Europe from the Jurassic to Lower Cretaceous period, with a well-documented mineralisation event occurring between *ca.* 140 and 165 Ma in the FMC and adjacent regions (i.e., Poitou, Morvan and Vendée). At this time, metals from the Variscan metamorphic rocks and granites were leached by basinal brines and redeposited below or above the unconformity between basement and Liassic sediments. The circulation of such fluids at temperatures up to 200 °C, was notably conducive to illite precipitation (e.g., Cathelineau et al., 2012), and likely resulted from far-field deformation during the Tethys-Atlantic-Caribbean rift evolution (Burisch et al., 2022) and the onset of the opening of the Bay of Biscay (Bouat et al., 2023). The precipitation of apatite IIIb and illite within the Beauvoir PRMG suggests that the Sioule region might have been partially covered by the Paris basin sediments at the end of the Jurassic and fluid infiltrations during reactivation of ancient basement faults may reflect the influence of the Pangea breakup on the FMC.

5.2. *Apatite as a proxy for magmatic evolution in PRMG systems*

Cathodoluminescence imaging of magmatic apatite from the Beauvoir PRMG commonly reveals growth zoning, as well as resorption textures, and distinctly secondary zones resulting from dissolution-reprecipitation processes, possibly related to the greisen alteration event (Figs. 4c, d, f, g, i). The greenish blue colour of magmatic apatite reflects high Mn content (Ribeiro et al., 2005) (Figs. 3a-c, 4b), which is a distinctive feature of apatite crystallising from highly evolved peraluminous melts (e.g., Sha and Chappell, 1999; Belousova et al., 2002; Broska et al., 2004; Roda-Robles et al., 2022). The decreasing proportion of magmatic apatite from the B2 and B3 units to the B1 unit is proposed to derive from the higher degree of magmatic evolution of the latter, P being preferentially concentrated into feldspars with increasing differentiation (London, 1992). Another possible explanation is the higher abundance of amblygonite-group minerals scavenging P from the melt in the B1 unit compared to the B2 and B3 units (Raimbault et al., 1995).

Considering the typical plots used to identify the parent rock type from apatite chemistry (e.g., Sha and Chappell, 1999; Belousova et al., 2002; O'Sullivan et al., 2020), magmatic apatite from the B2 and B3 units exhibit partial overlap with the "S-type granites" field as depicted on the Sr/Y vs ΣLREE biplot proposed by O'Sullivan et al. (2020) (Fig. 13). The remaining data points from these two units, as well as magmatic apatite from the B1 unit, fall within the fields corresponding to apatite from leucosomes/partial melts from high-grade metamorphic rocks and low-grade metamorphic/metasomatic rocks. Given that the Beauvoir PRMG exhibits a chemistry that is highly distinct from typical S-type granites, it is very likely that the chemistry of its magmatic apatite is also unique, which may account for the observed discrepancy from the "S-type granites" field. This is supported by the particular composition of igneous apatite from highly differentiated peraluminous granites and Li-rich pegmatites from the Variscan Iberian Massif (Spain; Merino Martínez, 2014; Roda-Robles et al., 2022) and Nb-Ta-(Li-Be-Cs) pegmatites from the Mufushan Complex rare-metal ore field (South China; Madayipu et al., 2024), exhibiting similar to even higher Sr/Y and lower LREE content compared to magmatic apatite in the Beauvoir PRMG. As illustrated in Fig. 13 and also in Fig. 9d, the transition from the less evolved B3 unit to the intermediate B2 unit, and most

differentiated B1 unit is associated with an overall depletion in REE and an increase in the La_N/Yb_N as well as Sr/Y ratios. This evolution could be ascribed to magmatic differentiation processes for PRMGs, as REE typically behave compatibly in low-temperature peraluminous magmas (e.g., Montel, 1993).

The chondrite-normalised REE distribution of magmatic apatite from the Beauvoir PRMG also slightly differs from typical patterns of apatite from S-type granites or other highly differentiated leucogranites (e.g., Sha and Chappell, 1999; Hsieh et al., 2008; Chu et al., 2009; Belousova et al., 2002; Roda-Robles et al., 2022). As previously described, apatite I is associated with a systematic LREE enrichment, a strong to moderate negative Eu anomaly (Eu/Eu* ~ 0.01–0.75), and a slight depletion in Nd only observed in the B2 and B3 units (Fig. 9a). REE patterns of apatite from typical S-type granites from the Lachlan Fold Belt, exhibiting upward convex profiles, pronounced negative Eu anomaly and frequent Nd depletion, resemble those of magmatic apatite from the Beauvoir PRMG (Sha and Chappell, 1999). However, apatite from those S-type granites differ from Beauvoir PRMG's apatite by a significant LREE depletion that has been ascribed to the crystallisation of monazite, which tends to reach saturation earlier than apatite in reduced and peraluminous magmas (Sha and Chappell, 1999). Due to the high concentration in fluxing elements, such as F and Li, within the Beauvoir melts, monazite saturation was likely not achieved (Raimbault et al., 1995). This could account for the LREE-enriched feature observed in both the whole-rock and igneous apatite REE patterns of the Beauvoir PRMG (Fig. 9a).

As expected for highly peraluminous granites, apatite I displays a pronounced negative Eu anomaly, its amplitude decreasing from the least differentiated B3 unit and intermediate B2 unit to the most evolved B1 unit. As Eu^{3+} is much closer to Ca^{2+} in ionic radius than Eu^{2+} at the two Ca nonequivalent sites in apatite, Eu^{3+} is preferentially incorporated in apatite structure compared to Eu^{2+} that is concentrated into feldspars (e.g., Budzinski and Tischendorf, 1989; Sha and Chappell, 1999). The partition coefficient of Eu between apatite and melt is thought to increase with increasing oxygen fugacity (fO_2), decreasing melt aluminosity and Eu^{2+}/Eu^{3+} ratio (Sha and Chappell, 1999). Therefore, the relative Eu enrichment observed with increasing differentiation may derive from the increase of oxidation degree characterising the transition from the B3 and B2 units to the B1 unit within the Beauvoir PRMG, which was interpreted by Cuney et al. (1992) and Pichavant (2022) as a primary magmatic feature.

Moreover, magmatic apatite exhibits an important tetrad effect, with estimated tetrad effect degrees (TE_{1-3}) ranging from 1.05 to 1.73 and mostly exceeding the significance threshold of 1.1 (Fig. 9a; Irber, 1999). This feature is commonly observed in highly evolved granites and associated metasomatic rocks. It has also been documented in melt inclusions (Peretyazhko and Savina, 2010) and minerals, such as zircon (Yang et al., 2014), columbite-group minerals (Badanina et al., 2015) and apatite (Chu et al., 2009; Roda-Robles et al., 2022). Although some recent studies suggested that the tetrad effect could be inherited from monazite and xenotime fractionation (Duc-Tin and Keppler, 2015; Shuai et al., 2021), it has been widely attributed to the selective complexation of REE by F or Cl during metasomatism, or fluid and melt exsolution (e.g., Bau, 1996; Irber, 1999; Jahn et al., 2001; Veksler et al., 2005; Monecke et al., 2007; Peretyazhko and Savina, 2010; Dostal et al., 2015; Ballouard et al., 2020b). As monazite and xenotime likely did not reach saturation from the Beauvoir melts (Raimbault et al., 1995), the pronounced tetrad effect observed in magmatic apatite REE distribution could reflect the exsolution of F-rich and Cl-rich magmatic fluids during magma crystallisation, which has been emphasised by the study of fluid inclusions (Aïssa et al., 1987).

From these data, apatite I has essentially preserved its original magmatic signature, but its chemistry also reveals signs of metasomatic overprint, in particular its O isotopic signature (Fig. 10a). In the absence of O isotopic data for apatite from other strongly fractionated highly peraluminous rocks, we suggest comparing the bulk rock $\delta^{18}O$ values of other Variscan peraluminous leucogranites and the Richemont rhyolitic dyke, which represents the subvolcanic equivalent of the Beauvoir PRMG, with the calculated oxygen isotopic composition of the Beauvoir melts. The latter can be estimated from $\delta^{18}O$ data obtained for magmatic apatite using the crystal-melt temperature-dependent fractionation factor of Zhao and Zheng (2003) for rhyolitic melt. For a crystallisation temperature of *ca.* 670 to 550 °C (emcompassing liquidus to solidus temperatures determined by Pichavant, 2022), the oxygen isotopic fractionation between apatite and the parent melt is limited ($\Delta^{18}O_{apatite\text{-}melt} \sim -1.3$ to -1.0 ‰; Zhao and Zheng, 2003). For unaltered zones of magmatic apatite, $\delta^{18}O$ values for the corresponding Beauvoir melts range from 7.3 to 9.8 ‰ (median ~ 8.9 ‰), 4.9 to 11.2 ‰ (median ~ 7.2 ‰), and 3.0 to 17.1 ‰ (median ~ 6.4 ‰) for the B3, B2 and B1 units, respectively. More than half of these estimates are significantly lower than the bulk rock $\delta^{18}O$ compositions of other Variscan peraluminous granites, which are typically above 11 ‰ when their magmatic signature is preserved (~ 10.7–13.6 ‰; Bernard-Griffiths et al., 1985; Turpin et al., 1990a; Tartèse and Boulvais, 2010; Ballouard et al., 2017), and are also below the single whole-rock $\delta^{18}O$ ratio of 9.0 ‰ obtained for the Richemont rhyolitic dyke (Raimbault and Burnol, 1998). Such discrepancy possibly indicates a partial reequilibration of apatite O isotopic compositions with external hydrothermal fluids, resulting in relatively low and highly variable $\delta^{18}O$ ratios. This O isotopic exchange might have been more intense towards the surface (i.e., from the B3 to B2 and B1 units), thus explaining the observed variability between magmatic apatite from the distinct units. Relatively low $\delta^{18}O$ values have been reported for other igneous minerals within the Beauvoir PRMG, including quartz, feldspar and lepidolite, and were interpreted to record meteoric water incursion at supra-solidus conditions and subsequent melt-fluid interactions (Fouillac et al., 1987; Fouillac and Rossi, 1991). Such hypothesis cannot be fully excluded and could explain the light isotope signature of magmatic apatite from the Beauvoir PRMG. However, apatite is sensitive to metasomatism (Harlov, 2015) and a subsolidus isotopic reequilibration with hydrothermal fluids remains plausible.

Overall, although the oxygen isotope signature of magmatic apatite was possibly partially reequilibrated during supra- to sub-solidus alteration, we argue that its elemental composition, at least its content of immobile elements (e.g., REEs and Y), was mostly preserved, thereby recording the evolution of the Beauvoir granitic melts. A comparable finding was observed in magmatic apatite from the Black Mountain porphyry deposit (Philippines; Cao et al., 2021). In this case, hydrothermal alteration resulted in modifications to the CL characteristics, fluid-mobile element concentrations (including Cl, Mg, Fe, Sr, Pb), and Sr-O isotope signatures of apatite, whereas other components (REE, Y, U, Th, and Zr) and the Nd isotope composition were preserved. Although Mn is generally considered as fluid-mobile, its concentration in magmatic apatite (Fig. 7) decreases from the B3 to B1 unit, mimicking Mn bulk rock concentrations, which could be ascribed to magmatic differentiation processes (Raimbault et al., 1995).

5.3. *Apatite as a proxy to trace nature and dynamics of hydrothermal systems in PRMGs*

The isotopic and elemental chemistry of apatite are currently considered as valuable tools in deciphering hydrothermal evolution in diverse geological environments, particularly in ore-forming systems (e.g., Seo et al., 2015; Bouzari et al., 2016; Mao et al., 2016; Ballouard et al., 2018; Cave et al., 2018; Pochon et al., 2018; Andersson et al., 2019; Melfou et al., 2023). For example, the $\delta^{18}O$ value in apatite is derived from the parent fluid and governed by temperature-dependent fractionation (Zheng, 1996), making the apatite O isotopic signature a recorder of fluid origin. The halogen (i.e., F, Cl, Br, and I) composition of apatite is also distinctive, as major terrestrial fluid reservoirs exhibit characteristic halogen chemistry generally preserved through most ore-forming processes (Lecumberri-Sanchez and Bodnar, 2018 and references therein). Although the anion site in apatite is dominated by F, Cl and OH, additional trace elements are typically incorporated, including

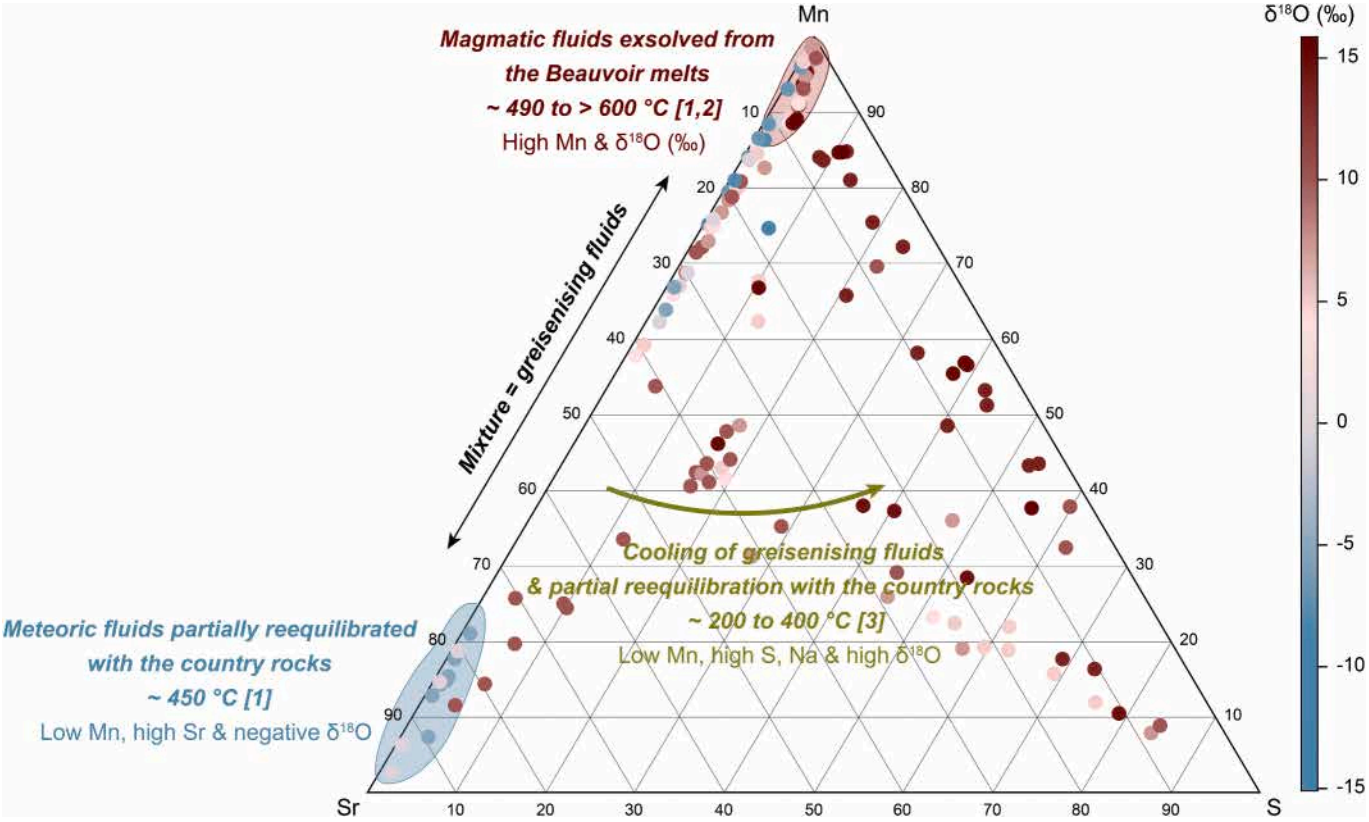

Fig. 14. Mn, Sr & S ternary diagram showing the geochemical evolution of hydrothermal apatite from the Beauvoir PRMG with colour scale representing $\delta^{18}O$ values. Data are from EPMA. When an element was not detected at an analysis spot, half of the detection limit was assigned as the concentration. Detailed trends between Sr and S content and O isotopic signature of apatite are illustrated on Fig. S3 (Supplementary Material 1). The early evolution of the Beauvoir magmatic-hydrothermal system is associated with mixing dynamics between isotopically heavy Mn-rich magmatic fluids and isotopically light oxidised Sr-rich meteoric fluids, partially reequilibrated with mica schist and paragneiss country rocks, at relatively high temperature. Progressive cooling and oxidation of the system concomitant with an increase of meteoric fluid contribution and degree of fluid-host-rock interaction led to an increase of $\delta^{18}O$ along with Mn depletion and S ± Na enrichment in apatite. The enrichement in S indicates partial reequilibration of the fluids with the counstry rocks. [1] Aïssa et al. (1987); [2] Harlaux et al. (2017); [3] Monnier et al. (2020).

Br and I (Pan and Fleet, 2002), with possible minor fractionation between Br and I during apatite precipitation (Andersson et al., 2019). The Br/I ratio of apatite could thus be used as a proxy for the Br/I ratio of the melts and hydrothermal fluids, providing insights into their origin.

O isotopic composition, major and trace elements content in the successive hydrothermal apatite generations of PRMGs, as exemplified by the Beauvoir case study, is a powerful approach to decipher the complex hydrothermal history that affected such type of magmatic system through time. Dark-CL primary micro-domains of apatite IIa (Fig. 5b) are characterised by significant MnO and Sn concentrations (2.7–4.8 wt.% and 24–65 ppm, respectively) (Fig. 14). Their REE distribution also shares similarities with magmatic apatite (i.e., comparable total REE concentrations and LREE enrichment), yet differing by a distinctive positive Eu anomaly (Fig. 9b). The latter may reflect the destabilisation of igneous feldspars during greisen alteration, which preferentially incorporate Eu in felsic magmas (Sha and Chappell, 1999). These dark primary micro-domains also exhibit Br/I molar ratios varying between 2.6 and 15.9, which largely overlap the range observed for apatite I (1.1–39.1), and fall in the range of fluids exsolved from S-type intrusions (3–20; Andersson et al., 2019) (Fig. 15). Furthermore, the co-precipitation of apatite IIa with cassiterite (generation II) in a vein highlights significant transport of Sn by hydrothermal fluids (Figs. 2, 5a). All of these characteristics combined suggest that apatite IIa primarily precipitated from hot and saline magmatic fluids, capable of transporting a significant amount of metals including Sn and REE (e.g., Candela, 1995; Bai and Van Groos, 1999; Audétat et al., 2008; Pirajno, 2009; Audétat and Edmonds, 2020). Dark primary micro-domains most likely recorded the circulation at high temperature (*ca.* 490 to >600 °C) of magmatic fluids exsolved from the Beauvoir melts (Aïssa et al., 1987; Harlaux et al., 2017), which are proven to be relatively enriched in Sn (*ca.* 1000–40,000 ppm; Harlaux et al., 2017) (Fig. 14). At such elevated temperatures, oxygen isotopic fractionation between fluids and apatite is minor (i.e., $\Delta^{18}O_{apatite\text{-}fluid} \sim -0.1$ to -0.5 ‰; Zheng, 1996). The $\delta^{18}O$ value of dark primary zones in apatite IIa varying between 2.7 and 7.5 ‰, the O isotopic composition estimated for the parent fluid (i.e., 2.8–8.0 ‰) essentially falls in the expected range for magmatic fluids (i.e., 5.5–9.5 ‰; Sheppard, 1986). The lowest $\delta^{18}O$ values probably derive from metasomatic alteration of apatite IIa, resulting in precipitation of the bright secondary micro-domains (Fig. 5b).

Apatite IIb exhibits heterogeneous O isotopic (Fig. 10) and elemental signatures (Figs. 7, 8, 9), with a trend between two end-members, excluding apatite IIb overprinted by kaolinisation (Fig. 14). The first end-member corresponds to magmatic fluids, as identified through the chemistry of apatite IIa. The second end-member, essentially represented by the analysed quartz-apatite vein, displays low MnO and high SrO contents (<0.1–1.0 wt.% and 1.0–4.7 wt.%, respectively), negative $\delta^{18}O$ values (−3.3 to −1.0 ‰) and a significantly different REE distribution from that of apatite IIa (i.e., MREE enrichment, with low La_N/Yb_N ratios, flat HREE signatures, and no distinct Eu anomaly). The following information can be deduced from these observations:

- Due to the preferentially incorporation of Mn^{2+} over Mn^{3+} and Mn^{4+} in apatite from direct substitution with Ca^{2+}, Mn content in apatite

not only depends on magma or fluid compositions, but also on oxygen fugacity (fO_2) within the system (e.g., Belousova et al., 2002). Within the Beauvoir PRMG, apatite Mn content progressively decreases over time, with the magmatic generation exhibiting significantly higher Mn concentrations compared to the early and late hydrothermal generations (MnO ~ 3.7 wt.%, 1.7 wt.% and 0.4 wt.%, respectively). Manganese depletion upon alteration has been documented in apatite from U deposit-related leucogranites of the Variscan belt and interpreted to reflect an interaction with oxidised meteoric hydrothermal fluids at subsolidus conditions (e.g., Ballouard et al., 2018).

- Strontium behaves compatibly during peraluminous magma differentiation, due to feldspar fractionation. Consequently, differentiated granitic intrusions typically exhibit very low whole-rock Sr contents. Experimental work has confirmed that Sr should have been depleted in the Beauvoir residual melts upon crystallisation (Pichavant, 2022). Despite its strongly differentiated nature, the Beauvoir PRMG is paradoxically rich in Sr, with whole-rock concentrations reaching up to 1000 ppm (Raimbault et al., 1995). To explain this unexpected particularity, Charoy et al. (2003) suggested the introduction of external Sr at the magmatic-hydrothermal transition by meteoric fluids partially equilibrated with the host mica schist. This high temperature hydrothermal event is presumed to have significantly affected both the chemistry and mineralogy of the Beauvoir PRMG, notably by inducing the recrystallisation of primary feldspars in albite (Pichavant et al., 1987a; Charoy et al., 2003; Pichavant, 2022). However, since the host mica schist is relatively Sr-poor (34–144 ppm, Table S9 in Supplementary Material 2), the Sr-enrichment observed in the Beauvoir PRMG may more likely originate from the leaching of the structurally overlying (Fig. 1b) and Sr-richer paragneiss units (112–259 ppm Sr; Fig. 8) by meteoric fluids. This incursion of Sr-rich meteoric fluids may also account for the Sr enrichment observed in apatite IIb (up to 4.7 wt.% SrO; mean ~ 1.15 wt.%), except in cases where apatite IIb has been overprinted by kaolinisation.
- Oxygen isotopic fractionation between fluids and apatite is minor at high temperature (e.g., $\Delta^{18}O_{apatite\text{-}fluid} = -0.5$ ‰ at 600 °C; Zheng, 1996). At temperatures lower than 480 °C, $\delta^{18}O$ values of the parent fluid are shown to be systematically lower than those of apatite (i.e., $\Delta^{18}O_{apatite\text{-}fluid} > 0$; Zheng, 1996). Consequently, the negative $\delta^{18}O$ values of several apatite IIb imply an equilibrium fluid with even more negative $\delta^{18}O$, strengthening the interpretation of a meteoric origin (Sheppard, 1986).
- This second end-member finally displays low total REE concentrations (< 26 ppm), MREE enrichment compared to LREE and HREE, with low La_N/Yb_N ratios (0.26–1.50), flat HREE profiles, and no distinct Eu anomaly. These characteristics are typically associated with a decrease in pH, temperature and fluid salinity, along with an increase in fO_2, which tend to result in an increased speciation of LREE within the fluid as highly stable and soluble chloride complexes, inhibiting their incorporation into apatite (e.g., Krneta et al., 2017). LREE depletion in apatite could also result from the co-precipitation of LREE-rich minerals, such as secondary monazite, as observed in Fig. 5c.

All these features indicate the influx of external fluids, mostly of meteoric origin, which underwent partial chemical equilibration and likely oxygen isotopic exchange with the country rocks during the greisenisation episode at *ca.* 310–315 Ma. At this period, the infiltration of meteoric fluids in the upper continental crust through strike-slip and detachment shear zones was previously highlighted in the Limousin region (north-western FMC) (Dusséaux et al., 2021). The distribution of apatite IIb data between the two end-members suggests mixing dynamics between magmatic and meteoric fluids (Fig. 14). Incursion of external fluids, concomitant with magmatic fluid circulation within the Beauvoir PRMG at high temperatures equal or above 400 °C, was previously emphasised by the study of fluid inclusions (Aïssa et al., 1987; Harlaux et al., 2017), and confirmed based on O isotope analyses by Fouillac et al. (1987) and Fouillac and Rossi (1991).

Greisen-alteration affecting RMGs is proposed to be mainly caused by the circulation of magmatic, acidic fluids, exhibiting low to moderate salinities (up to 10 wt.% NaCl eq) and a broad range of circulation temperatures (*ca.* 200 to 500 °C; e.g., Burt, 1981; Štemprok, 1987; Shepherd et al., 1985; Taylor, 1988; Schwartz and Surjono, 1990; Halter et al., 1998; Dobeš, 2005; Monnier et al., 2020). Mixing of magmatic fluids with fluids of external origin, in particular meteoric water, has however been emphasised in many ore-forming systems. This is for example the case for the Piaotang W-Sn deposit (Jiangxi, China), where meteoric fluids infiltrated the Piaotang granite from the earliest stages of its hydrothermal evolution (Legros et al., 2016, 2018 and references therein). Moreover, in the Cornubian Batholith (SW England), fluids of meteoric origin mixed with acidic and B-(Fe-Sn)-saturated magmatic-hydrothermal fluids and were responsible for muscovitisation (Putzolu et al., 2024). In the Beauvoir PRMG, meteoric fluid incursion is proposed to have been facilitated by fracture formation during greisenisation, and could have contributed to the progressive cooling of greisenising fluids from *ca.* 400 °C to 190 °C (Monnier et al., 2020).

Further evolution of the early hydrothermal fluid circulation, as recorded by apatite IIb overprinted by kaolinisation and apatite IIc, is characterised by a more pronounced depletion in MnO (<0.1–4.3 wt.%), an enrichment in SO_3, Na_2O, and, to a lesser extent, Al_2O_3 (<0.1–4.1 wt.%, <0.05–1.4 wt.% and <0.05–3.5 wt.%, respectively), along with heavier O isotopic signatures (mean ~ 8.2 ± 0.2 ‰) and highly variable Br/I ratios (~ 0.8–842) (Figs. 14, 15 and S3b in Supplementary Material 1). The S enrichment of the involved fluids most likely derives from similar processes to Sr enrichment, i.e., interactions with surrounding mica schist or paragneiss. Incorporation of the high-valence oxidised S^{6+} into the apatite structure also indicates that the hydrothermal system was relatively oxidising (i.e., high fO_2; e.g., Mao et al., 2016; Wang et al., 2022). The observed increase in Na content is probably a result of the co-substitution of S with Na to maintain charge balance (Pan and Fleet, 2002). The heavier O isotopic signature may originate from the combination of: (i) low-temperature fluid circulation inducing important oxygen isotope fractionation between fluids and apatite, and (ii) isotopic reequilibration of fluids with the host mica schists/paragneisses. While partial reequilibration of meteoric fluids with organic matter during their circulation within the country rocks may explain the relatively low Br/I ratios observed (*ca.* ⟨30) (Kendrick et al., 2011), another hypothesis could be the involvement of low Br/I sedimentary formation water (Worden, 1996) (Fig. 15). The first hypothesis seems more conceivable, as the Sioule region was likely not covered by a sedimentary basin at *ca.* 310–315 Ma. Higher Br/I ratios are mostly observed for apatite IIb overprinted by kaolinisation, and may result from a major contribution of high Br/I sedimentary formation water, possibly deriving from Mesozoic basins, and/or seawater (Worden, 1996)(Fig. 15). In summary, the early hydrothermal stage is initially dominated by the circulation of magmatic fluids, which mixed at high temperature (≥ 400 °C) with meteoric fluids partially reequilibrated with the host-rocks (Fig. 14). Meteoric fluids became progressively predominant (and cooler), inducing an increase in fO_2, and a subsequent decrease in Mn content and increase in S content and $\delta^{18}O$ in apatite II (Figs. 14 and S3b in Supplementary Material 1).

Two late hydrothermal events are temporally disconnected from the intrusion of the Beauvoir PRMG and result from the circulation of external fluids related to the regional tectonics. Apatite IIIa co-precipitated with fluorite at *ca.* 270 Ma and is essentially characterised by high As_2O_3 concentrations (0.4–5.3 wt.%) (Fig. 7), variable Br/I ratios (7–542; Fig. 15), a relatively heavy O isotope signature ($\delta^{18}O$ ~ 3.4–14.4 ‰) (Fig. 10h), as well as a LREE depletion compared to MREE and HREE (La_N/Yb_N ~ 0.06–0.51), and a moderate negative Eu anomaly (Eu/Eu* ~ 0.38–0.71) (Fig. 9c). The high As content of apatite IIIa reflects a high fO_2 within the system, as apatite preferentially incorporates its high-valence oxidised state (i.e., As^{5+}) (e.g., Mao et al.,

2016; Wang et al., 2022). Arsenic mobilisation from minerals depends on many parameters, including fluids temperature, pH and redox conditions (Smedley and Kinniburgh, 2002). Oxidising conditions will trigger As release from sulphide species, such as arsenopyrite (FeAsS) and arsenian pyrite ($Fe(S,As)_2$). Elevated As concentrations between 130 and 170 ppm, likely hosted in sulphide minerals, were measured for the Sioule mica schists (Table S9 in Supplementary Material 2) and hydrothermal alteration of such rocks at oxidised conditions could have liberated significant amount of this metal. Although Br/I ratios predominantly fall within the range of magmatic fluids, some values reach up to *ca.* 542. This may reflect halogen introduction from an external source, and more precisely, the possible circulation of sedimentary formation water derived from the overlying Permian basins (Fig. 15; Worden, 1996). Uraniferous deposits from the European Variscan belt were emplaced following the circulation of surface-derived oxidising aqueous fluids able to leach U from uranium oxides in the leucogranites (e.g., Cathelineau, 1982; Turpin et al., 1990b; Barsukov et al., 2006; Kříbek et al., 2009; Dolníček et al., 2014; Ballouard et al., 2017; Dusséaux et al., 2022) and As-rich apatite, dated at *ca.* 290 Ma, was found in a U-mineralised episyenite from a leucogranitic massif of the Variscan Armorican Massif (Ballouard et al., 2018). The circulation of such oxidised fluids within the Echassières complex may have mobilised As from the Sioule mica schists, and the F component of fluorite could directly originate from the destabilisation of F-rich igneous minerals such as lepidolite, topaz (and apatite) during interaction with hydrothermal fluids, without the need for external input of F.

Finally, the last hydrothermal stage affecting the Beauvoir PRMG, as identified in this study, led to the precipitation of apatite IIIb. Apatite IIIb exhibits a similar chemistry to the apatite characterising the end of the early hydrothermal stage, i.e., enrichment in SO_3, Na_2O and Al_2O_3 (<0.1–16 wt.%, 0.2–0.6 wt.% and <0.05–1.10 wt.%, respectively) (Fig. 7), LREE depletion compared to MREE and HREE (Fig. 9c), as well as the heaviest O isotopic signature (~ 13.6–17.0 ‰) (Fig. 10d). Therefore, the corresponding hydrothermal event likely originated from external fluid circulation at relatively low temperature in an oxidising environment. Apatite IIIb precipitation appears contemporaneous to illite precipitation in the Beauvoir PRMG (Fig. 12), and involved fluids that might have circulated at temperatures of *ca.* 200 °C (Merceron et al., 1987). As discussed in section 5.1, the precipitation of apatite IIIb may be linked to the widespread hydrothermal event affecting Western Europe from *ca.* 210 to 100 Ma, leading to the genesis of F-Ba-Pb-Zn mineralisation (Fig. 12). F-Ba-(Pb-Zn) vein-type deposits have been attributed to the circulation of moderately to highly saline, $CaCl_2$-NaCl-rich brines derived from seawater and/or meteoric water at temperatures ranging from 70 to 200 °C (Sizaret et al., 2004; Boiron et al., 2010; Sánchez et al., 2010). Assuming negligible fluid-apatite fractionation, the variable Br/I ratios observed for apatite IIIb, ranging from *ca.* 3 to 122 (Fig. 15), are consistent with such fluid origins.

5.4. *Apatite as a window into mineralising processes within PRMGs*

The decrease of Eu anomaly from the B3 to B1 unit (Fig. 9a) has important metallogenic implications as it confirms an increase in oxygen fugacity conditions during Beauvoir granitic magma differentiations previously recognised, based on the decrease in the Fe^{3+}/Fe^{2+} ratio of Li-micas from the B3 to the B1 (Cuney et al., 1992) and crystallisation experiments (Pichavant, 2022). Crystallisation experiments were carried out on powder samples from the Beauvoir B1 and B2 units and demonstrated that, to achieve the mineralogical and geochemical characteristics of the Beauvoir PRMG, the melts crystallised under unexpectedly oxidising conditions compared to the reduced conditions typically characterising highly peraluminous granitic magmas (Pichavant, 2022). Oxygen fugacity has been shown to have a dramatic influence on SnO_2 solubility in granitic melts, with cassiterite crystallisation ($Sn^{2+} \rightarrow Sn^{4+}$ transition) being favoured under oxidised conditions (Linnen et al., 1996; Bhalla et al., 2005; Pichavant, 2022). Therefore, in the Beauvoir PRMG, magmatic oxidation concomitant with increasing differentiation may have enhanced cassiterite crystallisation at the magmatic stage notably in the B1 unit (Cst I; Fig. 2). The causes of such oxididdation remain unclear. It may reflect the "self-oxidation" of the melt due to the exsolution of HF^- as a vapor component (Pichavant et al., 2016). However, open-system mechanisms including the impact of external fluids still deserves to be evaluated in the context of the Beauvoir PRMG, considering that the oxygen isotope analyses of igneous minerals including quartz, lepidolite (Fouillac et al., 1987; Fouillac and Rossi, 1991) and magmatic apatite (this study) suggest incursion of oxidised meteoric fluids at high temperatures and possibly suprasolidus conditions.

Vein apatite IIa is characterised by a complex CL texture, featuring bright secondary zones replacing dark primary areas (Fig. 16a). It

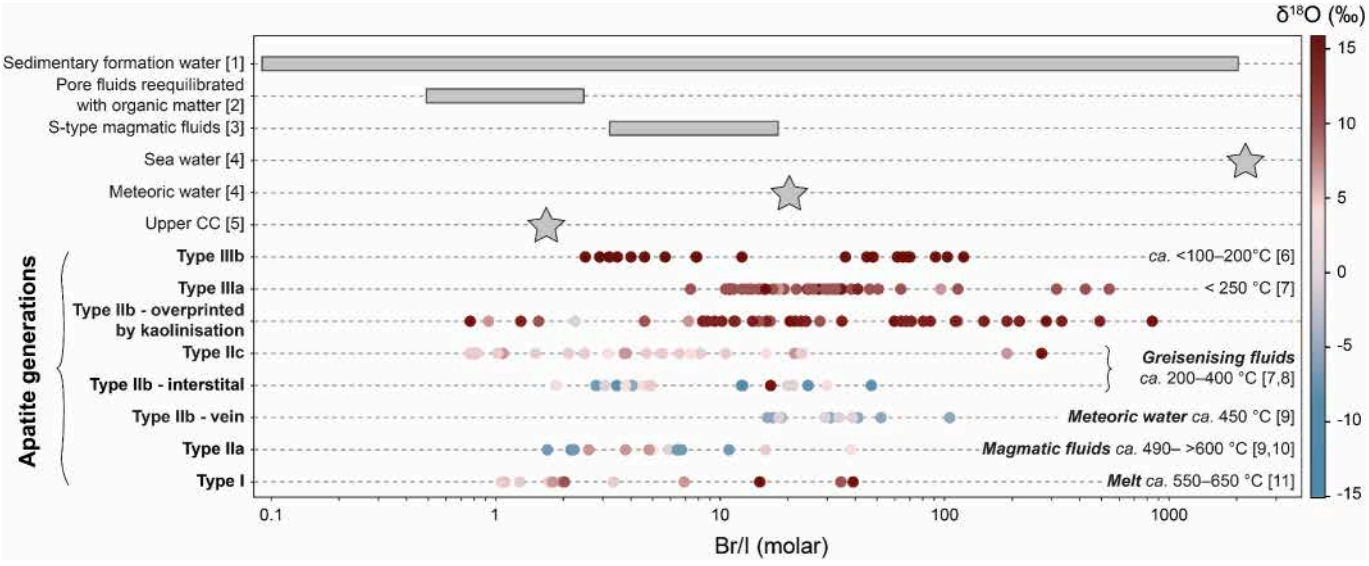

Fig. 15. Br/I molar ratios of the distinct apatite generations within the Beauvoir PRMG with colour scale representing $\delta^{18}O$ values. Data for the upper continental crust, meteoric water, sea water, S-type magmatic fluids, pore fluids reequilibrated with organic matter and sedimentary formation water are plotted as reference. [1] Worden (1996); [2] Kendrick et al. (2011); [3] Andersson et al. (2019); [4] Worden (2018); [5] Webster et al. (2018); [6] Merceron et al. (1987); [7] Merceron et al. (1992); [8] Monnier et al. (2020); [9] Aïssa et al. (1987); [10] Harlaux et al. (2017); [11] Pichavant (2022).

represents the only hydrothermal apatite subset within the Beauvoir PRMG that notably co-precipitates with rare metal-bearing minerals, in this instance cassiterite (Fig. 16b). Apatite IIb has also been found in association with wolframite within greisen-altered quartz veins of the La Bosse stockwork (Fig. 5c; Table 1; Monnier et al., 2019).

The two distinct textural micro-domains of apatite IIa differ by specific elemental and O isotopic chemistries, as illustrated on Figs. 16c and d. The dark-CL primary zones show high Mn and low Sr contents, as well as relatively heavy O isotopic signatures. In contrast, bright-CL secondary zones exhibit lower Mn but higher Sr concentrations and negative $\delta^{18}O$ values. While the characteristics of dark-CL primary zones can be attributed to their precipitation from magmatic fluids exsolved from the melt, the precipitation of bright-CL secondary zones is unambiguously related to the circulation of meteoric fluids (section 5.3). Another interesting discrepancy between both micro-domains is their Sn concentrations, which are relatively higher in dark-CL primary zones compared to secondary ones (*ca.* 23–65 ppm and 0–3 ppm, respectively; Fig. 16c). This observation is consistent with the significant Sn content of magmatic fluids emphasised through the study of fluid inclusions (*ca.* 1000–40,000 ppm; Harlaux et al., 2017).

In Cl-F-bearing magmatic fluids, SnO_2 solubility decreases with increasing oxygen fugacity (fO_2) and decreasing fluid acidity ($m_{HCl,aq}$) (Taylor and Wall, 1993). The early incursion of meteoric fluids highlighted in apatite IIa and their mixing with magmatic fluids would thus likely trigger cassiterite precipitation (Cst II; Fig. 2). This process could explain the preferential localisation of cassiterite within the luminescent secondary zones or at the transition between dark- and bright-CL zones (Fig. 16b).

Mixing dynamics between magmatic and meteoric fluids thus appear to have significant implications for the precipitation of metals, particularly Sn, during the hydrothermal stage within the Beauvoir PRMG. Although the necessity of oxidising agents for cassiterite precipitation was questioned by Liu et al. (2023), the prominent role of meteoric water influx in the crystallisation of cassiterite is well-established in Sn (-W) hydrothermal deposits associated with granite intrusions (Witt, 1988; Heinrich, 1990; Audétat et al., 1998; Karimzadeh Somarin and Ashley, 2004; Fekete et al., 2016; Liu et al., 2020; Chen et al., 2023; Peng et al., 2023). Therefore, although the majority of Sn mineralisation derives from Sn saturation at the magmatic stage, leading to the crystallisation of cassiterite I, meteoric water influx also appears to be inherent to the hydrothermal ore-forming processes (Cst II) of the Beauvoir PRMG, and could probably play a major role in other PRMGs.

The majority of current genetic models proposed for PRMGs, and more broadly RMGs, involve closed systems of isocomposition dominated by purely magmatic processes (e.g., Kovalenko et al., 1970; Groves and McCarthy, 1978; Raimbault et al., 1995; Pichavant, 2022). Yet, some studies highlighted the necessity to consider the exsolution of magmatic fluids (or hydrosaline melt) and subsequent fluid-rock interactions to fully explain the formation of rare-metal deposits (e.g., Thomas et al., 2011; Badanina et al., 2015; Ballouard et al., 2016, 2020a; Araujo et al., 2023; Pfister et al., 2023; Putzolu et al., 2024), and in some rare cases, the interactions between melt and external fluids to trigger metal precipitation (London et al., 1996; Linnen et al., 2019; McNeil et al., 2020). Beyond the already well-established role of meteoric fluids in Sn precipitation, some authors have suggested a significant contribution of external fluids to the Fe and Mn content of columbite-group minerals (Linnen et al., 2019). In the Beauvoir PRMG, the crystallisation of columbite- and pyrochlore-group minerals is thought to have been influenced by fluid circulation of meteoric origin, especially in the most evolved B1 unit (Ohnenstetter and Piantone, 1988; Fouillac and Rossi, 1991). Therefore, RMGs genesis involving open systems, potentially characterised by interactions between melts and external fluids, seems to require more serious consideration.

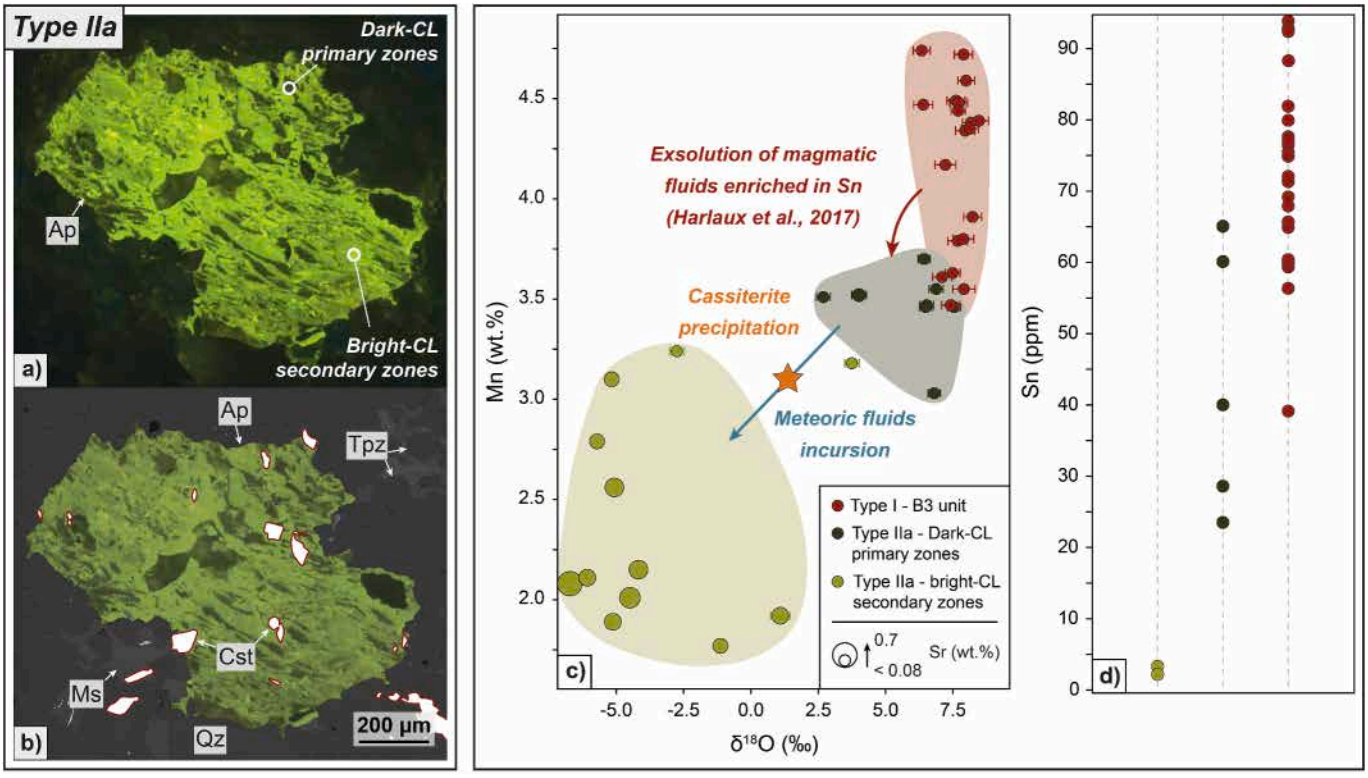

Fig. 16. Chemistry of CL textural micro-domains in early hydrothermal apatite IIa: (a) CL image highlighting dark primary and bright secondary zones; (b) Superposition of CL and BSE images highlighting cassiterite preferential precipitation in bright-CL secondary zones or at the transition between dark- and bright-CL zones; (c) Oxygen isotopic signature plotted against Mn content in apatite, with the size of the data points representing the Sr content; (d) Sn contents of the two distinct micro-domains of apatite IIa. The composition of magmatic apatite I from the B3 unit of the Beauvoir PRMG is shown in (c) and (d) for comparison.

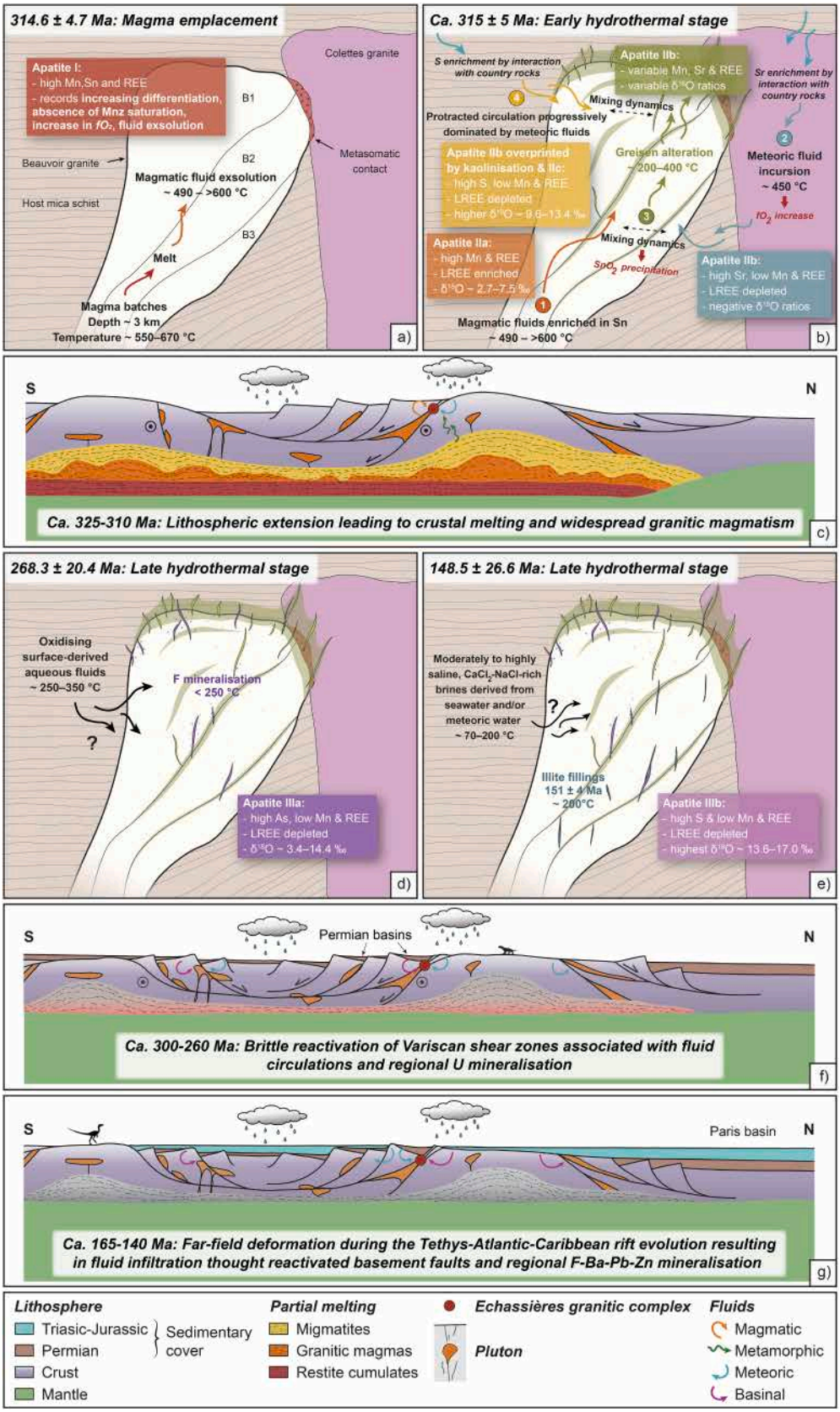

(caption on next page)

Fig. 17. Simplified cross-sections illustrating a schematic evolution of the Beauvoir magmatic-hydrothermal system, as revealed by apatite chemistry and U-Pb geochronology, along with corresponding regional geodynamic events: (a-c) Magmatic to early hydrothermal evolution and (d-g) Late hydrothermal evolution. Crustal scale cross-sections (c-f-g) are modified from Monnier et al. (2021). The age mentioned in Figure b corresponds to the overlap of ages obtained for apatite IIa and IIb (i.e., 314.3 ± 5.5 Ma and 311.7 ± 8.1 Ma, respectively). Temperatures of melts, fluid circulations and greisen alteration within the Beauvoir PRGM (a-b-d-e) are from Aïssa et al. (1987); Merceron et al. (1987, 1992); Harlaux et al. (2017); Monnier et al. (2020); Pichavant (2022). Temperatures of external fluid circulation (d-e) are from Ballouard et al. (2017) and references therein, Cathelineau et al. (2012) and references therein.

6. Summary and conclusions

The study of apatite within the Beauvoir PRMG unravel a complex and polyphased magmatic-hydrothermal system (Fig. 17):

- Magmatic apatite (apatite I) formed at 314.6 ± 4.7 Ma, consistent with previous estimations based on other geochronometers. The LREE enrichment observed reflects the absence of monazite saturation during crystallisation, while the decrease in the Eu anomaly amplitude may record the increase in fO_2 from the root to the apical zone of the granite upon differentiation, which may have facilitated the crystallisation of the predominant cassiterite generation (i.e., cassiterite I) at supra-solidus conditions. The exsolution of magmatic fluids also affected the signature of magmatic apatite, especially from the deeper facies, by inducing a pronounced tetrad effect in its REE patterns.
- The exsolution of magmatic fluids, evidenced by apatite I and IIa, initiated the early hydrothermal stage at 314.3 ± 5.5 Ma. It is characterised by magmatic fluid exsolution followed by mixing dynamics between magmatic and meteoric fluids during greisenisation, which contributed to a gradual decrease in temperature and further increase in fO_2 of the system (Mn-depleted apatite reaching negative $\delta^{18}O$ values). Meteoric fluids were partially reequilibrated with the country rocks, resulting in a progressive introduction of Sr and S within the Beauvoir PRMG. Apatite chemistry shows that meteoric fluids play an important role in greisenisation processes within the Beauvoir PRMG. The early incursion of meteoric fluids most likely resulted in a sudden shift in redox conditions towards a more oxidising environment, triggering precipitation of cassiterite from magmatic fluids. Further constraining the timing and temperature conditions of meteoric fluid incursion in the Beauvoir magmatic-hydrothermal system is crucial, as it might have major implications for understanding the crystallisation mechanism of rare metal-bearing minerals in PRMG environments.
- Two later hydrothermal events, post-dating granite emplacement at *ca.* 310–315 Ma and the circulation of magmatic-hydrothermal fluids, have been identified from apatite U-Pb ages and chemical characteristics, providing insights in the influence of regional tectonic events on the evolution of the Beauvoir PRMG. The first event took place at 268.3 ± 20.4 Ma (Permian-Triassic). It resulted in fluorite mineralisation in the Beauvoir PRMG, and is possibly related to Europe-wide post-ororgenic extension-related circulation of basin- and surface-derived oxidising fluids that mobilised U from fertile Variscan leucogranites between 300 and 260 Ma. The second event, dated at 148.5 ± 26.6 Ma (Jurassic-Cretaceous), is proposed to be linked to widespread extension-related F-Ba-Pb-Zn mineralisation affecting Western Europe from *ca.* 210 to 100 Ma.

As demonstrated in several studies, apatite represents a powerful mineral to decipher magmatic and hydrothermal processes within various environments, and this study showcases its usefulness in granite-related rare metal deposits. The PHP-RMGs typified by the Beauvoir granite are specifically marked by high P concentrations which favour apatite crystallisation throughout most of its magmatic and hydrothermal evolution. As such, studying the distinct apatite generations in such context thus provides major insights for the magmatic and hydrothermal processes that have affected them through geological history and controlled their metal endowment.

CRediT authorship contribution statement

Océane Rocher: Writing – original draft, Methodology, Investigation, Funding acquisition, Conceptualization. **Christophe Ballouard:** Writing – review & editing, Supervision, Funding acquisition, Conceptualization. **Antonin Richard:** Writing – review & editing, Supervision, Funding acquisition, Conceptualization. **Loïs Monnier:** Writing – review & editing, Supervision, Funding acquisition, Conceptualization. **Patrick Carr:** Writing – review & editing, Methodology, Investigation. **Oscar Laurent:** Writing – review & editing, Supervision, Funding acquisition, Conceptualization. **Yanis Khebabza:** Investigation. **Andreï Lecomte:** Methodology. **Nordine Bouden:** Methodology. **Johan Villeneuve:** Methodology. **Benjamin Barré:** Writing – review & editing, Resources. **Patrick Fullenwarth:** Writing – review & editing, Resources. **Mathieu Leisen:** Writing – review & editing, Supervision, Methodology. **Julien Mercadier:** Writing – review & editing, Supervision, Funding acquisition, Conceptualization.

Declaration of competing interest

The authors declare the following financial interests/personal relationships which may be considered as potential competing interests: Oceane Rocher reports financial support was provided by IMERYS. Oceane Rocher reports a relationship with IMERYS that includes: funding grants. If there are other authors, they declare that they have no known competing financial interests or personal relationships that could have appeared to influence the work reported in this paper.

Data availability

Data will be made available on request.

Acknowledgments

This work was supported by the French National Research Agency through the national program “Investissements d’avenir” with the reference ANR-10-LABX-21 – RESSOURCES21, the ANR TRANSFAIR (ANR-21-01CE-0022-01) project, a CNRS-INSU-TelluS-SYSTER grant, and Imerys company.

We warmly thank, Matthieu Harlaux, Jérémy Melleton and Eric Gloaguen (BRGM) and Michel Cuney and the Li-Beauvoir group (Université de Lorraine) for fruitful discussions. We are indebt to Grégoire Jean (Imerys) for his continuous support. We greatly thank Alexandre Flammang and John Moine for thin section preparation, Olivier Rouer for support in EMP analyses at GeoRessources as well as Françoise Maubé and Aurélie Marquet for precious help for SEM and LA-ICP-MS analyses at Géosciences Environnement Toulouse. We also thank all members of the Li-Beauvoir working group at GeoRessources and CRPG laboratories for fruitful discussions, and especially Nicolas Esteves for sharing samples. We are indebt to Robin Shail and an anonymous reviewer for their insightful reviews, and to co-editor-in-chief Marco Fiorentini for his careful editorial handling.

Appendix A. Supplementary data

Supplementary data to this article can be found online at https://doi.org/10.1016/j.chemgeo.2024.122400.

References

Aïssa, M., Weisbrod, A., Marignac, C., 1987. Caractéristiques chimiques et thermodynamiques des circulations hydrothermales du site d'Échassières. Géol. Fr. 2-3, 335–350.

Andersen, C., Weis, P., 2020. Heat transfer from convecting magma reservoirs to hydrothermal fluid flow systems constrained by coupled numerical modeling. Geophys. Res. Lett. 47 https://doi.org/10.1029/2020GL089463 e2020GL089463.

Andersson, S.S., Wagner, T., Jonsson, E., Fusswinkel, T., Whitehouse, M.J., 2019. Apatite as a tracer of the source, chemistry and evolution of ore-forming fluids: the case of the Olserum-Djupedal REE-phosphate mineralisation, SE Sweden. Geochim. Cosmochim. Acta 255, 163–187. https://doi.org/10.1016/j.gca.2019.04.014.

Angrand, P., Mouthereau, F., 2021. Evolution of the Alpine orogenic belts in the Western Mediterranean region as resolved by the kinematics of the Europe-Africa diffuse plate boundary. BSGF-Earth Sci. Bull. 192, 42. https://doi.org/10.1051/bsgf/2021031.

Araujo, F.P., Muchez, P., Hulsbosch, N., 2023. The magmatic-hydrothermal transition in P-rich pegmatitic melts: Crystal-melt-fluid interactions recorded by phosphate minerals. Geochim. Cosmochim. Acta 356, 129–148. https://doi.org/10.1016/j.gca.2023.07.009.

Aubert, G., 1969. Les coupoles granitiques de Montebras et d'Echassières (Massif central français) et la genèse de leurs minéralisations en étain, lithium, tungstène et béryllium. [PhD thesis, BRGM, Paris] Mem, 46. BRGM, pp. 1–349.

Audétat, A., Edmonds, M., 2020. Magmatic-Hydrothermal Fluids. Elem 16, 401–406. https://doi.org/10.2138/gselements.16.6.401.

Audétat, A., Günther, D., Heinrich, C.A., 1998. Formation of a magmatic-hydrothermal ore deposit: Insights with LA-ICP-MS analysis of fluid inclusions. Sci 279, 2091–2094. https://doi.org/10.1126/science.279.5359.2091.

Audétat, A., Günther, D., Heinrich, C.A., 2000. Magmatic-hydrothermal evolution in a fractionating granite: a microchemical study of the Sn-W-F-mineralized mole granite (Australia). Geochim. Cosmochim. Acta 64, 3373–3393. https://doi.org/10.1016/S0016-7037(00)00428-2.

Audétat, A., Pettke, T., Heinrich, C.A., Bodnar, R.J., 2008. Special paper: the composition of magmatic-hydrothermal fluids in barren and mineralized intrusions. Econ. Geol. 103, 877–908. https://doi.org/10.2113/gsecongeo.103.5.877.

Badanina, E.V., Veksler, I.V., Thomas, R., Syritso, L.F., Trumbull, R.B., 2004. Magmatic evolution of Li-F, rare-metal granites: a case study of melt inclusions in the Khangilay complex, Eastern Transbaikalia (Russia). Chem. Geol. 210, 113–133. https://doi.org/10.1016/j.chemgeo.2004.06.006.

Badanina, E.V., Sitnikova, M.A., Gordienko, V.V., Melcher, F., Gäbler, H.-E., Lodziak, J., Syritso, L.F., 2015. Mineral chemistry of columbite-tantalite from spodumene pegmatites of Kolmozero, Kola Peninsula (Russia). Ore Geol. Rev. 64, 720–735. https://doi.org/10.1016/j.oregeorev.2014.05.009.

Baertschi, P., 1976. Absolute18O content of standard mean ocean water. Earth Planet. Sci. Lett. 31, 341–344. https://doi.org/10.1016/0012-821X(76)90115-1.

Bai, T.B., Van Groos, A.K., 1999. The distribution of Na, K, Rb, Sr, Al, Ge, Cu, W, Mo, La, and Ce between granitic melts and coexisting aqueous fluids. Geochim. Cosmochim. Acta 63, 1117–1131. https://doi.org/10.1016/S0016-7037(98)00284-1.

Ballèvre, M., Martínez Catalán, J.R., López-Carmona, A., Pitra, P., Abati, J., Fernández, R.D., Ducassou, C., Arenas, R., Bosse, V., Castiñeiras, P., Fernández-Suárez, J., Gómez Barreiro, J., Paquette, J.-L., Peucat, J.-J., Poujol, M., Ruffet, G., Sánchez Martínez, S., 2014. Correlation of the nappe stack in the Ibero-Armorican arc across the Bay of Biscay: a joint French-Spanish project. Geol. Soc. Lond. Spec. Publ. 405, 77–113. https://doi.org/10.1144/SP405.13.

Ballouard, C., Poujol, M., Boulvais, P., Branquet, Y., Tartèse, R., Vigneresse, J.-L., 2016. Nb-Ta fractionation in peraluminous granites: a marker of the magmatic-hydrothermal transition. Geol 44, 231–234. https://doi.org/10.1130/G37475.1.

Ballouard, C., Poujol, M., Boulvais, P., Mercadier, J., Tartèse, R., Venneman, T., Deloule, E., Jolivet, M., Kéré, I., Cathelineau, M., Cuney, M., 2017. Magmatic and hydrothermal behavior of uranium in syntectonic leucogranites: the uranium mineralization associated with the Hercynian Guérande granite (Armorican Massif, France). Ore Geol. Rev. 80, 309–331. https://doi.org/10.1016/j.oregeorev.2016.06.034.

Ballouard, C., Poujol, M., Mercadier, J., Deloule, E., Boulvais, P., Baele, J.M., Cuney, M., Cathelineau, M., 2018. Uranium metallogenesis of the peraluminous leucogranite from the Pontivy-Rostrenen magmatic complex (French Armorican Variscan belt): the result of long-term oxidized hydrothermal alteration during strike-slip deformation. Mineral. Deposita 53, 601–628. https://doi.org/10.1007/s00126-017-0761-5.

Ballouard, C., Elburg, M.A., Tappe, S., Reinke, C., Ueckermann, H., Doggart, S., 2020a. Magmatic-hydrothermal evolution of rare metal pegmatites from the Mesoproterozoic Orange River pegmatite belt (Namaqualand, South Africa). Ore Geol. Rev. 116, 103252 https://doi.org/10.1016/j.oregeorev.2019.103252.

Ballouard, C., Massuyeau, M., Elburg, M.A., Tappe, S., Viljoen, F., Brandenburg, J.-T., 2020b. The magmatic and magmatic-hydrothermal evolution of felsic igneous rocks as seen through Nb-Ta geochemical fractionation, with implications for the origins of rare-metal mineralizations. Earth Sci. Rev. 203, 103115 https://doi.org/10.1016/j.earscirev.2020.103115.

Ballouard, C., Couzinié, S., Bouilhol, P., Harlaux, M., Mercadier, J., Montel, J.-M., 2023. A felsic meta-igneous source for Li-F-rich peraluminous granites: insights from the Variscan Velay dome (French Massif Central) and implications for rare-metal magmatism. Contrib. Mineral. Petrol. 178, 75. https://doi.org/10.1007/s00410-023-02057-1.

Ballouard, C., Carr, P., Parisot, F., Gloaguen, É., Melleton, J., Cauzid, J., Lecomte, A., Rouer, O., Salsi, L., Mercadier, J., 2024. Petrogenesis and tectonic-magmatic context of emplacement of lepidolite and petalite pegmatites from the Fregeneda-Almendra field (Variscan Central Iberian Zone): clues from Nb-Ta-Sn oxide U-Pb geochronology and mineral geochemistry. BSGF-Earth Sci. Bull. 195, 3. https://doi.org/10.1051/bsgf/2023015.

Barbarin, B., 1999. A review of the relationships between granitoid types, their origins and their geodynamic environments. Lithos 46, 605–626. https://doi.org/10.1016/S0024-4937(98)00085-1.

Barsukov, V.L., Sokolova, N.T., Ivanitskii, O.M., 2006. Metals, arsenic, and sulfur in the Aue and Eibenstock granites, Erzgebirge. Geochem. Int. 44, 896–911. https://doi.org/10.1134/S0016702906090059.

Bau, M., 1996. Controls on the fractionation of isovalent trace elements in magmatic and aqueous systems: evidence from Y/Ho, Zr/Hf, and lanthanide tetrad effect. Contrib. Mineral. Petrol. 123, 323–333. https://doi.org/10.1007/s004100050159.

Baubron, J.C., Jébrak, M., Joannes, C., Lhégu, J., Touray, J.C., Ziserman, A., 1980. Nouvelles datations K/Ar sur des filons à quartz et fluorine du Massif Central français. C. R. Acad. Sci. 290, 951–953.

Bellahsen, N., Mouthereau, F., Boutoux, A., Bellanger, M., Lacombe, O., Jolivet, L., Rolland, Y., 2014. Collision kinematics in the western external Alps. Tecton 33, 1055–1088. https://doi.org/10.1002/2013TC003453.

Belousova, E.A., Griffin, W.L., O'Reilly, S.Y., Fisher, N.I., 2002. Apatite as an indicator mineral for mineral exploration: trace-element compositions and their relationship to host rock type. J. Geochem. Explor. 76, 45–69. https://doi.org/10.1016/S0375-6742(02)00204-2.

Bernard-Griffiths, J., Peucat, J.J., Sheppard, S., Vidal, P., 1985. Petrogenesis of Hercynian leucogranites from the southern Armorican Massif: contribution of REE and isotopic (Sr, Nd, Pb and O) geochemical data to the study of source rock characteristics and ages. Earth Planet. Sci. Lett. 74, 235–250. https://doi.org/10.1016/0012-821X(85)90024-X.

Bettencourt, J.S., Leite Jr., W.B., Goraieb, C.L., Sparrenberger, I., Bello, R.M., Payolla, B. L., 2005. Sn-polymetallic greisen-type deposits associated with late-stage rapakivi granites, Brazil: fluid inclusion and stable isotope characteristics. Lithos 80, 363–386. https://doi.org/10.1016/j.lithos.2004.03.060.

Bhalla, P., Holtz, F., Linnen, R.L., Behrens, H., 2005. Solubility of cassiterite in evolved granitic melts: effect of T, fO_2, and additional volatiles. Lithos 80, 387–400. https://doi.org/10.1016/j.lithos.2004.06.014.

Blès, J.L., Bonijoly, D., Castaing, C., Gros, Y., 1989. Successive post-Variscan stress fields in the French Massif Central and its borders (Western European plate): comparison with geodynamic data. Tectonophys 169, 79–111. https://doi.org/10.1016/0040-1951(89)90185-6.

Boiron, M.-C., Cathelineau, M., Richard, A., 2010. Fluid flows and metal deposition near basement/cover unconformity: lessons and analogies from Pb-Zn-F-Ba systems for the understanding of Proterozoic U deposits. Geofluids 10, 270–292. https://doi.org/10.1111/j.1468-8123.2010.00289.x.

Bouat, L., Strzerzynski, P., Mourgues, R., Branquet, Y., Cogné, N., Barré, G., Gardien, V., 2023. Early, far-field and diffuse tectonics records in the North Aquitaine Basin (France). BSGF-Earth Sci. Bull. 194, 17. https://doi.org/10.1051/bsgf/2023014.

Bouchez, J.-L., Bernier, S., Rochette, P., Guineberteau, B., 1987. Log des susceptibilités magnétiques et anisotropies de susceptibilité dans le granite de Beauvoir : conséquences pour sa mise en place. Géol. Fr. 2-3, 223–232.

Bouchot, V., Ledru, P., Lerouge, C., Lescuyer, J.-L., Milesi, J.-P., 2005. 5: late Variscan mineralizing systems related to orogenic processes: the French Massif Central. Ore Geol. Rev. 27, 169–197. https://doi.org/10.1016/j.oregeorev.2005.07.017.

Bouzari, F., Hart, C.J.R., Bissig, T., Barker, S., 2016. Hydrothermal Alteration Revealed by Apatite Luminescence and Chemistry: a potential Indicator Mineral for Exploring Covered Porphyry Copper deposits. Econ. Geol. 111, 1397–1410. https://doi.org/10.2113/econgeo.111.6.1397.

Boynton, W.V., 1984. Cosmochemistry of the rare Earth elements: Meteorite Studies. Dev. Geochem. 2, 63–114. https://doi.org/10.1016/B978-0-444-42148-7.50008-3.

Breiter, K., Müller, A., Leichmann, J., Gabašová, A., 2005. Textural and chemical evolution of a fractionated granitic system: the Podlesí stock, Czech Republic. Lithos 80, 323–345. https://doi.org/10.1016/j.lithos.2003.11.004.

Breiter, K., Ďurišová, J., Hrstka, T., Korbelová, Z., Hložková Vaňková, M., Vašinová Galiová, M., Kanický, V., Rambousek, P., Knésl, I., Dobeš, P., Dosbaba, M., 2017. Assessment of magmatic vs. metasomatic processes in rare-metal granites: a case study of the Cínovec/Zinnwald Sn-W-Li deposit, Central Europe. Lithos 292, 198–217. https://doi.org/10.1016/j.lithos.2017.08.015.

Broska, I., Williams, C.T., Uher, P., Konečný, P., Leichmann, J., 2004. The geochemistry of phosphorus in different granite suites of the Western Carpathians, Slovakia: the role of apatite and P-bearing feldspar. Chem. Geol. 205, 1–15. https://doi.org/10.1016/j.chemgeo.2003.09.004.

Bruguier, O., Becq-Giraudon, J.F., Bosch, D., Lancelot, J.R., 1998. Late Visean hidden basins in the internal zones of the Variscan belt: U-Pb zircon evidence from the French Massif Central. Geol 26, 627–630. https://doi.org/10.1130/0091-7613(1998)026%3C0627:LVHBIT%3E2.3.CO;2.

Budzinski, H., Tischendorf, G., 1989. Distribution of REE among minerals in the Hercynian postkinematic granites of Westerzgebirge-Vogtland, GDR. Z. Geol. Wiss. 17, 1019–1031.

Burisch, M., Markl, G., Gutzmer, J., 2022. Breakup with benefits-hydrothermal mineral systems related to the disintegration of a supercontinent. Earth Planet. Sci. Lett. 580, 117373 https://doi.org/10.1016/j.epsl.2022.117373.

Burnard, P.G., Polya, D.A., 2004. Importance of mantle derived fluids during granite associated hydrothermal circulation: he and Ar isotopes of ore minerals from Panasqueira. Geochim. Cosmochim. Acta 68, 1607–1615. https://doi.org/10.1016/j.gca.2003.10.008.

Burnham, C.W., 1979. The importance of volatile constituents. The Evolution of the Igneous Rocks 439, 82.

Burt, D.M., 1981. Acidity-salinity diagrams; application to greisen and porphyry deposits. Econ. Geol. 76, 832–843. https://doi.org/10.2113/gsecongeo.76.4.832.
Candela, P.A., 1995. Model Ore-Metal Partitioning from Melts into Vapor and Vapor/Brine Mistures. Magmas, Fluids, and Ore Depos.
Candela, P.A., 1997. A review of shallow, ore-related granites: textures, volatiles, and ore metals. J. Petrol. 38, 1619–1633. https://doi.org/10.1093/petroj/38.12.1619.
Cao, M., Evans, N.J., Hollings, P., Cooke, D.R., McInnes, B.I.A., Qin, K., 2021. Apatite texture, composition, and O-Sr-Nd isotope signatures record magmatic and hydrothermal fluid characteristics at the Black Mountain porphyry deposit, Philippines. Econ. Geol. 116, 1189–1207. https://doi.org/10.5382/econgeo.4827.
Carl, C., Dill, H.G., Kreuzer, H., Wendt, I., 1983. U-Pb dating of ores in NE Bavaria. Terra Cognita 3, 195–196.
Carr, P.A., Mercadier, J., Harlaux, M., Romer, R.L., Moreira, E., Legros, H., Cuney, M., Marignac, C., Cauzid, J., Salsi, L., 2021. U/Pb geochronology of wolframite by LA-ICP-MS; mineralogical constraints, analytical procedures, data interpretation, and comparison with ID-TIMS. Chem. Geol. 584, 120511 https://doi.org/10.1016/j.chemgeo.2021.120511.
Carrat, G.H., 1956. Uranium Deposit of Bauzot (Saone et Loire). CEA Saclay.
Cathelineau, M., 1982. Les gisements d'uranium liés spatialement aux leucogranites sud-armoricains et à leur encaissant métamorphique, relations et interactions entre les minéralisations et divers contextes géologiques et structuraux. BRGM. Sci. Terre 42, 7–347.
Cathelineau, M., Boiron, M.C., Holliger, P., Poty, B., 1990. Metallogenesis of the French part of the Variscan orogen. Part II: Time-space relationships between U, au and Sn-W ore deposition and geodynamic events—mineralogical and U-Pb data. Tectonophys 177, 59–79. https://doi.org/10.1016/0040-1951(90)90274-C.
Cathelineau, M., Boiron, M.-C., Fourcade, S., Ruffet, G., Clauer, N., Belcourt, O., Coulibaly, Y., Banks, D.A., Guillocheau, F., 2012. A major late Jurassic fluid event at the basin/basement unconformity in western France: 40Ar/39Ar and K-Ar dating, fluid chemistry, and related geodynamic context. Chem. Geol. 322, 99–120. https://doi.org/10.1016/j.chemgeo.2012.06.008.
Cave, B.W., Lilly, R., Glorie, S., Gillespie, J., 2018. Geology, Apatite Geochronology, and Geochemistry of the Ernest Henry Inter-lens: Implications for a Re-Examined Deposit Model. Miner 8, 405. https://doi.org/10.3390/min8090405.
Černý, P., 1986. Characteristics of Pegmatite Deposits of Tantalum. In: Möller, P., Černý, Petr, Saupé, F. (Eds.), Lanthanides, Tantalum and Niobium. Spec. Publ. No. 7 Soc. Geol. Appl. Min. Depos. Springer Berl. Heidelb, pp. 195–239. https://doi.org/10.1007/978-3-642-87262-4_8.
Černý, P., Ercit, T.S., 2005. The classification of granitic pegmatites revisited. Can. Mineral. 43, 2005–2026. https://doi.org/10.2113/gscanmin.43.6.2005.
Charoy, B., Chaussidon, M., Le Carlier De Veslud, C., Duthou, J.L., 2003. Evidence of Sr mobility in and around the albite-lepidolite-topaz granite of Beauvoir (France): an in-situ ion and electron probe study of secondary Sr-rich phosphates. Contrib. Mineral. Petrol. 145, 673–690. https://doi.org/10.1007/s00410-003-0458-x.
Cheilletz, A., Archibald, D.A., Cuney, M., Charoy, B., 1992. Ages $^{40}Ar/^{39}Ar$ du leucogranite à topaze-lépidolite de Beauvoir et des pegmatites sodolithiques de Chédeville (Nord du Massif Central, France). Signification pétrologique et géodynamique. C. R. Acad. Sci. Série 2, Méc., Phys., Chim., Sci. Univers, Sci. Terre 315, 329–336.
Chen, Y.-K., Ni, P., Pan, J.-Y., Cui, J.-M., Li, W.-S., Fang, G.-J., Zhao, Z.-H., Xu, Y.-M., Ding, J.-Y., Han, L., 2023. Fluid evolution and metallogenic mechanism of the Xianghualing skarn-type Sn deposit, South China: evidence from petrography, fluid inclusions and trace-element composition of cassiterite. Ore Geol. Rev. 154, 105351 https://doi.org/10.1016/j.oregeorev.2023.105351.
Chew, D.M., Spikings, R.A., 2015. Geochronology and thermochronology using apatite: time and temperature, lower crust to surface. Elem 11, 189–194. https://doi.org/10.2113/gselements.11.3.189.
Chu, M.-F., Wang, K.-L., Griffin, W.L., Chung, S.-L., O'Reilly, S.Y., Pearson, N.J., Iizuka, Y., 2009. Apatite Composition: Tracing Petrogenetic Processes in Transhimalayan Granitoids. J. Petrol. 50, 1829–1855. https://doi.org/10.1093/petrology/egp054.
Coulson, I.M., Villeneuve, M.E., Dipple, G.M., Duncan, R.A., Russell, J.K., Mortensen, J.K., 2002. Time-scales of assembly and thermal history of a composite felsic pluton: constraints from the Emerald Lake area, northern Canadian Cordillera, Yukon. J. Volcanol. Geotherm. Res. 114, 331–356. https://doi.org/10.1016/S0377-0273(01)00294-3.
Cuney, M., Autran, A., 1987. Objectifs généraux du projet GPF Echassières n.1 et résultats essentiels acquis par le forage de 900 m sur le granite albitique à topaze-lépidolite de Beauvoir. Géol. Fr. 2-3, 7–24.
Cuney, M., Marignac, C., Weisbrod, A., 1992. The Beauvoir topaz-lepidolite albite granite (Massif Central, France); the disseminated magmatic Sn-Li-Ta-Nb-be mineralization. Econ. Geol. 87, 1766–1794. https://doi.org/10.2113/gsecongeo.87.7.1766.
Cuney, M., Alexandrov, P., Carlier, Le, de Veslud, C., Cheilletz, A., Raimbault, L., Ruffet, G., Scaillet, S., 2002. The timing of W-Sn-rare metals mineral deposit formation in the Western Variscan chain in their orogenic setting: the case of the Limousin area (Massif Central, France). Geol. Soc. Lond. Spec. Publ. 204, 213–228. https://doi.org/10.1144/GSL.SP.2002.204.01.13.
Davaine, J.J., 1980. Les croûtes silico-fluorées mésozoïques du Bazois, description et modèle d'évolution. Mem. BRGM 104, 211–241.
Decrée, S., Cawthorn, G., Deloule, E., Mercadier, J., Frimmel, H., Baele, J.-M., 2020. Unravelling the processes controlling apatite formation in the Phalaborwa complex (South Africa) based on combined cathodoluminescence, LA-ICPMS and in-situ O and Sr isotope analyses. Contrib. Mineral. Petrol. 175, 34. https://doi.org/10.1007/s00410-020-1671-6.
Dilles, J.H., 1987. Petrology of the Yerington Batholith, Nevada; evidence for evolution of porphyry copper ore fluids. Econ. Geol. 82, 1750–1789. https://doi.org/10.2113/gsecongeo.82.7.1750.
Do Couto, D., Faure, M., Augier, R., Cocherie, A., Rossi, P., Li, X.-H., Lin, W., 2015. Monazite U-Th-Pb EPMA and zircon U-Pb SIMS chronological constraints on the tectonic, metamorphic, and thermal events in the inner part of the Variscan orogen, example from the Sioule series, French Massif Central. Int. J. Earth Sci. 105, 557–579. https://doi.org/10.1007/s00531-015-1184-0.
Dobeš, P., 2005. Fluid inclusion planes and paleofluid records in the Podlesí granite, Krušné hory Mts., Czech Republic. Bull. Geosci. 80, 2.
Dolníček, Z., René, M., Hermannová, S., Prochaska, W., 2014. Origin of the Okrouhlá Radouň episyenite-hosted uranium deposit, Bohemian Massif, Czech Republic: fluid inclusion and stable isotope constraints. Mineral. Deposita 49, 409–425. https://doi.org/10.1007/s00126-013-0500-5.
Dostal, J., Kontak, D.J., Gerel, O., Shellnutt, J.G., Fayek, M., 2015. Cretaceous ongonites (topaz-bearing albite-rich microleucogranites) from Ongon Khairkhan, Central Mongolia: products of extreme magmatic fractionation and pervasive metasomatic fluid: rock interaction. Lithos 236, 173–189. https://doi.org/10.1016/j.lithos.2015.08.003.
Duc-Tin, Q., Keppler, H., 2015. Monazite and xenotime solubility in granitic melts and the origin of the lanthanide tetrad effect. Contrib. Mineral. Petrol. 169, 1–26. https://doi.org/10.1007/s00410-014-1100-9.
Dusséaux, C., Gébelin, A., Ruffet, G., Mulch, A., 2021. Late Carboniferous paleoelevation of the Variscan belt of Western Europe. Earth Planet. Sci. Lett. 569, 117064 https://doi.org/10.1016/j.epsl.2021.117064.
Dusséaux, C., Gébelin, A., Boulvais, P., Ruffet, G., Poujol, M., Cogné, N., Branquet, Y., Mottram, C., Barou, F., Mulch, A., 2022. Timing and duration of meteoric water infiltration in the Quiberon detachment zone (Armorican Massif, Variscan belt, France). J. Struct. Geol. 156, 104546 https://doi.org/10.1016/j.jsg.2022.104546.
Duthou, J.-L., Pin, C., 1987. Etude isotopique Rb-Sr de l'apex granitique d'Echassières (Granite des Colettes, granite de Beauvoir). Géol. Fr. 2-3, 63–67.
Eikenberg, J.H.R., 1988. Vergleichende Datierung von Uranmineralien mit den U-XE, U-KR und U-PB Systemen, sowie Untersuchungen der Produktion von NE und AR durch Kernprozesse. [PhD thesis, ETH Zürich]. https://www.research-collection.ethz.ch/bitstream/handle/20.500.11850/139396/eth-37452-01.pdf.
Estéoule-Choux, J., 1967. Contribution à l'étude des argiles du Massif armoricain. Argiles des altérations et des bassins sédimentaires tertiaires. Mém. Soc. Géol. Min. de Bretagne 14, 319.
Esteves, N., France, L., Bouilhol, P., Cuney, M., 2024. Plutonic formation through sills stacking and amalgamation: the case of Beauvoir rare-metal granite. EGU General Assembly 2024, Vienna, Austria, 14–19 Apr 2024, EGU24-20364. https://doi.org/10.5194/egusphere-egu24-20364.
Faure, M., Lardeaux, J.-M., Ledru, P., 2009. A review of the pre-Permian geology of the Variscan French Massif Central. Compt. Rendus Geosci. 341, 202–213. https://doi.org/10.1016/j.crte.2008.12.001.
Fekete, S., Weis, P., Driesner, T., Bouvier, A.-S., Baumgartner, L., Heinrich, C.A., 2016. Contrasting hydrological processes of meteoric water incursion during magmatic-hydrothermal ore deposition: an oxygen isotope study by ion microprobe. Earth Planet. Sci. Lett. 451, 263–271. https://doi.org/10.1016/j.epsl.2016.07.009.
Feybesse, J.L., 1985. Etude structurale du massif d'Echassières et de son encaissant métamorphique. Geol. Fr. 8 Doc. BRGM 95-8, 55–72.
Ford, M., Lickorish, W.H., 2004. Foreland basin evolution around the western Alpine Arc. Geol. Soc. Lond. Spec. Publ. 221, 39–63. https://doi.org/10.1144/GSL.SP.2004.221.01.04.
Fouillac, A.-M., Rossi, P., 1991. Near-solidus delta^{18}O depletion in a Ta-Nb-bearing albite granite: the Beauvoir Granite, France. Econ. Geol. 86, 1704–1720. https://doi.org/10.2113/gsecongeo.86.8.1704.
Fouillac, A.-M., Kosakevitch, A., Merceron, T., Meunier, A., Rossi, P., 1987. Comportement des fluides dans l'évolution magmatique puis hydrothermale du granite à Ta, Nb, Li de Beauvoir d'après la géochimie isotopique de l'oxygène et l'hydrogène. Géol. Fr. 2-3, 279–293.
Gagny, C., 1987. Organisation séquentielle évolutive des intrusions successives du Granite de Beauvoir dans son caisson: Arguments géochimiques. Géol. Fr. 2-3, 199–208.
Gagny, C., Jacquot, T., 1987. Contribution de la pétrologie structurale à la connaissance des conditions de mise en place et de structuration complexe du granite des Colettes (Massif d'Echassières, Massif Central Français). Géol. Fr. 2-3, 47–56.
Gagny, C., Courrioux, G., Cuenin, O., Jacquot, T., Leistel, J.-M., 1984. Contrôle structural de la métallogenèse dans la région d'Echassières par une zone de cisaillement régional orientée à N 60E (Massif Central français). C. R. Séances Acad. Sci. Série 2, Méc.-phys., Chim., Sci. Univers, Sci. Terre 298, 459–462.
Gaudin, A., Ansan, V., Rigaudier, T., 2015. Mineralogical and $\delta^{18}O$-δD isotopic study of kaolinized micaschists at Penestin, Armorican Massif, France: New constraint in the kaolinization process. Catena 133, 97–106. https://doi.org/10.1016/j.catena.2015.05.006.
Gigoux, M., 2015. Origine des minéralisations stratiformes de fluorine de la bordure sud-est du bassin de Paris. [PhD thesis, Université Paris Sud - Paris XI]. https://theses.hal.science/tel-01249598/.
Gigoux, M., Delpech, G., Guerrot, C., Pagel, M., Augé, T., Négrel, P., Brigaud, B., 2015. Evidence for an early cretaceous mineralizing event above the basement/sediment unconformity in the intracratonic Paris Basin: paragenetic sequence and Sm-Nd dating of the world-class Pierre-Perthuis stratabound fluorite deposit. Mineral. Deposita 50, 455–463. https://doi.org/10.1007/s00126-015-0592-1.
Grolier, J., 1971. Contribution à l'étude géologique des séries cristallophylliennes inverses du Massif Central français : la série de la Sioule (Puy-de-Dôme, Allier). [PhD thesis, BRGM, Paris] Mem. BRGM 64, 1–163.

Groves, D.I., McCarthy, T.S., 1978. Fractional crystallization and the origin of tin deposits in granitoids. Mineral. Deposita 13, 11–26. https://doi.org/10.1007/BF00202905.

Guillocheau, F., Robin, C., Allemand, P., Bourquin, S., Brault, N., Dromart, G., Fridenberg, R., Garcia, J.-P., Gaulier, J.-M., Gaumet, F., Grosdoy, B., Hanot, F., Le Start, P., Mettraux, M., Nalpas, T., Prijac, C., Rigoltet, C., Serrano, O., Grandjean, G., 2000. Meso-Cenozoic geodynamic evolution of the Paris Basin: 3D stratigraphic constraints. Geodin. Acta 13, 189–245. https://doi.org/10.1080/09853111.2000.11105372.

Halter, W.E., Webster, J.D., 2004. The magmatic to hydrothermal transition and its bearing on ore-forming systems. Chem. Geol. 210, 1–6. https://doi.org/10.1016/j.chemgeo.2004.06.001.

Halter, W.E., Williams-Jones, A.E., Kontak, D.J., 1998. Modeling fluid-rock interaction during greisenization at the East Kemptville tin deposit: implications for mineralization. Chem. Geol. 150, 1–17. https://doi.org/10.1016/S0009-2541(98)00050-3.

Handy, M.R., Schmid, S.M., Bousquet, R., Kissling, E., Bernoulli, D., 2010. Reconciling plate-tectonic reconstructions of Alpine Tethys with the geological-geophysical record of spreading and subduction in the Alps. Earth Sci. Rev. 102, 121–158. https://doi.org/10.1016/j.earscirev.2010.06.002.

Harlaux, M., Mercadier, J., Bonzi, W.M.-E., Kremer, V., Marignac, C., Cuney, M., 2017. Geochemical Signature of Magmatic-Hydrothermal Fluids Exsolved from the Beauvoir Rare-Metal Granite (Massif Central, France): Insights from LA-ICPMS Analysis of primary Fluid Inclusions. Geofluids 2017, 1–25. https://doi.org/10.1155/2017/1925817.

Harlaux, M., Romer, R.L., Mercadier, J., Morlot, C., Marignac, C., Cuney, M., 2018. 40 Ma of hydrothermal W mineralization during the Variscan orogenic evolution of the French Massif Central revealed by U-Pb dating of wolframite. Mineral. Deposita 53, 21–51. https://doi.org/10.1007/s00126-017-0721-0.

Harlov, D.E., 2015. Apatite: a Fingerprint for Metasomatic Processes. Elem 11, 171–176. https://doi.org/10.2113/gselements.11.3.171.

Heinrich, C.A., 1990. The chemistry of hydrothermal tin (−tungsten) ore deposition. Econ. Geol. 85, 457–481. https://doi.org/10.2113/gsecongeo.85.3.457.

Hofmann, B., Eikenberg, J., 1991. The Krunkelbach uranium deposit, Schwarzwald, Germany; correlation of radiometric ages (U-Pb, U-Xe-Kr, K-Ar, ^{230}Th-^{234}U). Econ. Geol. 86, 1031–1049. https://doi.org/10.2113/gsecongeo.86.5.1031.

De Hoÿm de Marien, de Marien, L., Pitra, P., Poujol, M., Cogné, N., Cagnard, F., Le Bayon, B., 2023. Complex geochronological record of an emblematic Variscan eclogite (Haut-Allier, French Massif Central). J. Metamorph. Geol. 41, 967–995. https://doi.org/10.1111/jmg.12733.

Hsieh, P.-S., Chen, C.-H., Yang, H.-J., Lee, C.-Y., 2008. Petrogenesis of the Nanling Mountains granites from South China: Constraints from systematic apatite geochemistry and whole-rock geochemical and Sr-Nd isotope compositions. J. Asian Earth Sci. 33, 428–451. https://doi.org/10.1016/j.jseaes.2008.02.002.

Ingebritsen, S.E., Geiger, S., Hurwitz, S., Driesner, T., 2010. Numerical simulation of magmatic hydrothermal systems. Rev. Geophys. 48 https://doi.org/10.1029/2009RG000287.

Irber, W., 1999. The lanthanide tetrad effect and its correlation with K/Rb, Eu/Eu*, Sr/Eu, Y/Ho, and Zr/Hf of evolving peraluminous granite suites. Geochim. Cosmochim. Acta 63, 489–508. https://doi.org/10.1016/S0016-7037(99)00027-7.

Jacquot, T., 1987. Dynamique de l'organisation séquentielle du magma de Beauvoir. Apport de la pétrologie structurale. Géol. Fr. 2-3, 209–222.

Jacquot, T., Gagny, C., 1987. Pétrologie structurale du granite de Beauvoir (Massif d'Echassières) : données et interprétation a son niveau apical. Géol. Fr. 2-3, 57–62.

Jahn, B., Wu, F., Capdevila, R., Martineau, F., Zhao, Z., Wang, Y., 2001. Highly evolved juvenile granites with tetrad REE patterns: the Woduhe and Baerzhe granites from the Great Xing'an Mountains in NE China. Lithos 59, 171–198. https://doi.org/10.1016/S0024-4937(01)00066-4.

Jaranowski, M., Budzyń, B., Rzepa, G., Sláma, J., Sawłowicz, Z., 2021. Geochemical constraints on the distribution of trace elements and volatiles in fluorapatite from the Panasqueira tin-tungsten deposit (Portugal). Geochem 81, 125765. https://doi.org/10.1016/j.chemer.2021.125765.

Jochum, K.P., Weis, U., Stoll, B., Kuzmin, D., Yang, Q., Raczek, I., Jacob, D.E., Stracke, A., Birbaum, K., Frick, D.A., 2011. Determination of reference values for NIST SRM 610-617 glasses following ISO guidelines. Geostand. Geoanal. Res. 35, 397–429. https://doi.org/10.1111/j.1751-908X.2011.00120.x.

Johan, V., Monier, G., Rossi, P., 1988. Etude pétrographique systématique des granites du sondage GPF1 de Beauvoir. Documents BRGM 124, 11–101.

Joseph, D., Bellon, H., Derre, C., Touray, J.C., 1973. Fluorite veins dated in the 200 million year range at La Petite Verrière and Chavaniac. France. Econ. Geol. 68, 707–708. https://doi.org/10.2113/gsecongeo.68.5.707.

Kaeter, D., Barros, R., Menuge, J.F., Chew, D.M., 2018. The magmatic-hydrothermal transition in rare-element pegmatites from Southeast Ireland: LA-ICP-MS chemical mapping of muscovite and columbite-tantalite. Geochim. Cosmochim. Acta 240, 98–130. https://doi.org/10.1016/j.gca.2018.08.024.

Karimzadeh Somarin, A., Ashley, P., 2004. Hydrothermal alteration and mineralisation of the Glen Eden Mo-W-Sn deposit: a leucogranite-related hydrothermal system, Southern New England Orogen, NSW, Australia. Mineral. Deposita 39, 282–300. https://doi.org/10.1007/s00126-003-0399-3.

Kendrick, M.A., Phillips, D., Wallace, M., Miller, J.M., 2011. Halogens and noble gases in sedimentary formation waters and Zn-Pb deposits: a case study from the Lennard Shelf, Australia. Appl. Geochem. 26, 2089–2100. https://doi.org/10.1016/j.apgeochem.2011.07.007.

Kovalenko, V.I., Kuz'min, M.I., Letnikov, F.A., 1970. Magmatic origin of lithium-and fluorine-bearing rare-metal granite. Dokl. Acad. Sci. USSR. Earth Sci. Seet 190, 189–190.

Kříbek, B., Žák, K., Dobeš, P., Leichmann, J., Pudilová, M., René, M., Scharm, B., Scharmová, M., Hájek, A., Holeczy, D., 2009. The Rožná uranium deposit (Bohemian Massif, Czech Republic): shear zone-hosted, late Variscan and post-Variscan hydrothermal mineralization. Mineral. Deposita 44, 99–128. https://doi.org/10.1007/s00126-008-0188-0.

Krneta, S., Ciobanu, C.L., Cook, N.J., Ehrig, K., Kontonikas-Charos, A., 2017. Rare earth element behaviour in apatite from the Olympic Dam Cu-U-Au-Ag deposit, South Australia. Miner 7, 135. https://doi.org/10.3390/min7080135.

Kusebauch, C., John, T., Whitehouse, M.J., Engvik, A.K., 2015a. Apatite as probe for the halogen composition of metamorphic fluids (Bamble Sector, SE Norway). Contrib. Mineral. Petrol. 170, 34. https://doi.org/10.1007/s00410-015-1188-6.

Kusebauch, C., John, T., Whitehouse, M.J., Klemme, S., Putnis, A., 2015b. Distribution of halogens between fluid and apatite during fluid-mediated replacement processes. Geochim. Cosmochim. Acta 170, 225–246. https://doi.org/10.1016/j.gca.2015.08.023.

Launay, G., Sizaret, S., Lach, P., Melleton, J., Gloaguen, É., Poujol, M., 2021. Genetic relationship between greisenization and Sn-W mineralizations in vein and greisen deposits: Insights from the Panasqueira deposit (Portugal). Bull. Soc. Géol. Fr. 192, 2. https://doi.org/10.1051/bsgf/2020046.

Laurent, O., Zeh, A., Gerdes, A., Villaros, A., Gros, K., Słaby, E., 2017. How do granitoid magmas mix with each other? Insights from textures, trace element and Sr-Nd isotopic composition of apatite and titanite from the Matok pluton (South Africa). Contrib. Mineral. Petrol. 172, 1–22. https://doi.org/10.1007/s00410-017-1398-1.

Lecumberri-Sanchez, P., Bodnar, R.J., 2018. Halogen Geochemistry of Ore deposits: Contributions Towards Understanding sources and Processes. In: Harlov, D.E., Aranovich, L. (Eds.), The Role of Halogens in Terrestrial and Extraterrestrial Geochemical Processes. Springer Geochem, pp. 261–305. https://doi.org/10.1007/978-3-319-61667-4_5.

Lecumberri-Sanchez, P., Vieira, R., Heinrich, C.A., Pinto, F., Wälle, M., 2017. Fluid-rock interaction is decisive for the formation of tungsten deposits. Geol 45, 579–582. https://doi.org/10.1130/G38974.1.

Legros, H., Marignac, C., Mercadier, J., Cuney, M., Richard, A., Wang, R.-C., Charles, N., Lespinasse, M.-Y., 2016. Detailed paragenesis and Li-mica compositions as recorders of the magmatic-hydrothermal evolution of the Maoping W-Sn deposit (Jiangxi, China). Lithos 264, 108–124. https://doi.org/10.1016/j.lithos.2016.08.022.

Legros, H., Marignac, C., Tabary, T., Mercadier, J., Richard, A., Cuney, M., Wang, R.-C., Charles, N., Lespinasse, M.-Y., 2018. The ore-forming magmatic-hydrothermal system of the Piaotang W-Sn deposit (Jiangxi, China) as seen from Li-mica geochemistry. Am. Mineral. 103, 39–54. https://doi.org/10.2138/am-2018-6196.

Legros, H., Richard, A., Tarantola, A., Kouzmanov, K., Mercadier, J., Vennemann, T., Marignac, C., Cuney, M., Wang, R.-C., Charles, N., 2019. Multiple fluids involved in granite-related W-Sn deposits from the world-class Jiangxi province (China). Chem. Geol. 508, 92–115. https://doi.org/10.1016/j.chemgeo.2018.11.021.

Lenoir, L., Blaise, T., Chourio-Camacho, D., Richard, A., Tarantola, A., Agrinier, P., Rigaudier, T., Monvoisin, G., Bardoux, G., Brigaud, B., 2023. The origin of fluorite-barite mineralization at the interface between the Paris Basin and its Variscan basement: insights from fluid inclusion chemistry and isotopic (O, H, Cl) composition. Mineral. Deposita 59, 397–417. https://doi.org/10.1007/s00126-023-01219-2.

Linnen, R.L., 1998. The solubility of Nb-Ta-Zr-Hf-W in granitic melts with Li and Li+ F; constraints for mineralization in rare metal granites and pegmatites. Econ. Geol. 93, 1013–1025. https://doi.org/10.2113/gsecongeo.93.7.1013.

Linnen, R.L., Cuney, M., 2005. Granite-related rare-element deposits and experimental constraints on Ta-Nb-W-Sn-Zr-Hf mineralization. In: Linnen, R.L., Samson, I.M. (Eds.), Rare-Element Geochemistry and Mineral Deposits. Geol. Assoc. Can, Short Course.

Linnen, R.L., Pichavant, M., Holtz, F., 1996. The combined effects of fO_2 and melt composition on SnO_2 solubility and tin diffusivity in haplogranitic melts. Geochim. Cosmochim. Acta 60, 4965–4976. https://doi.org/10.1016/S0016-7037(96)00295-5.

Linnen, R.L., McNeil, A., Flemming, R., 2019. Some thoughts on metasomatism in pegmatites. Can. Mineral. 57, 765–766. https://doi.org/10.3749/canmin.AB00016.

Liu, P., Mao, J., Jian, W., Mathur, R., 2020. Fluid mixing leads to main-stage cassiterite precipitation at the Xiling Sn polymetallic deposit, SE China: evidence from fluid inclusions and multiple stable isotopes (H-O-S). Mineral. Deposita 55, 1233–1246. https://doi.org/10.1007/s00126-019-00933-0.

Liu, X., Yu, P., Xiao, C., 2023. Tin transport and cassiterite precipitation from hydrothermal fluids. Geosci. Front. 14, 101624 https://doi.org/10.1016/j.gsf.2023.101624.

London, D., 1992. Phosphorus in S-type magmas: the P_2O_5 content of feldspars from peraluminous granites, pegmatites, and rhyolites. Am. Mineral. 77, 126–145.

London, D., Morgan, G.B., Wolf, M.B., 1996. Boron in granitic rocks and their contact aureoles. Rev. Mineral. Geochem. 33, 299–330.

Lotout, C., Poujol, M., Pitra, P., Anczkiewicz, R., Van Den Driessche, J., 2020. From Burial to Exhumation: Emplacement and Metamorphism of Mafic Eclogitic Terranes Constrained through Multimethod Petrochronology, Case Study from the Lévézou Massif (French Massif Central, Variscan Belt). J. Petrol. 61, egaa046. https://doi.org/10.1093/petrology/egaa046.

Madayipu, N., Li, H., Elatikpo, S.M., Ghaderi, M., Heritier, R.N., Hu, X.-J., Zheng, H., Wu, Q.-H., 2024. Tracing fluid exsolution and hydrothermal alteration signature of the Mufushan Nb-Ta-(Li-Be-Cs) deposit, South China: an apatite perspective. J. Geol. Soc. Lond. 181 https://doi.org/10.1144/jgs2023-087 jgs2023-087.

Mao, M., Rukhlov, A.S., Rowins, S.M., Spence, J., Coogan, L.A., 2016. Apatite Trace Element Compositions: a Robust New Tool for Mineral Exploration. Econ. Geol. 111, 1187–1222. https://doi.org/10.2113/econgeo.111.5.1187.

Marignac, C., Cuney, M., Cathelineau, M., Lecomte, A., Carocci, E., Pinto, F., 2020. The Panasqueira rare Metal Granite Suites and their Involvement in the Genesis of the World-Class Panasqueira W-Sn-Cu Vein Deposit: a Petrographic. Mineralogical, and Geochemical Study Miner. 10, 562. https://doi.org/10.3390/min10060562.

Masuda, A., Kawakami, O., Dohmoto, Y., Takenaka, T., 1987. Lanthanide tetrad effects in nature: two mutually opposite types, W and M. Geochem. J. 21, 119–124. https://doi.org/10.2343/geochemj.21.119.

Matte, P., 1986. Tectonics and plate tectonics model for the Variscan belt of Europe. Tectonophys 126, 329–374. https://doi.org/10.1016/0040-1951(86)90237-4.

Matte, P., 1991. Accretionary history and crustal evolution of the Variscan belt in Western Europe. Tectonophys 196, 309–337. https://doi.org/10.1016/0040-1951(91)90328-P.

McDowell, F.W., McIntosh, W.C., Farley, K.A., 2005. A precise ^{40}Ar-^{39}Ar reference age for the Durango apatite (U-Th)/he and fission-track dating standard. Chem. Geol. 214, 249–263. https://doi.org/10.1016/j.chemgeo.2004.10.002.

McNeil, A.G., Linnen, R.L., Flemming, R.L., Fayek, M., 2020. An experimental approach to examine fluid-melt interaction and mineralization in rare-metal pegmatites. Am. Mineral. 105, 1078–1087. https://doi.org/10.2138/am-2020-7216.

Melfou, M., Richard, A., Tarantola, A., Villeneuve, J., Carr, P., Peiffert, C., Mercadier, J., Dean, B., Drejing-Carroll, D., 2023. Tracking the origin of metasomatic and ore-forming fluids in IOCG deposits through apatite geochemistry (Nautanen North deposit, Norrbotten, Sweden). Lithos 438-439, 106995. https://doi.org/10.1016/j.lithos.2022.106995.

Melleton, J., Gloaguen, E., Frei, D., 2015. Rare-elements (Li-Be-Ta-Sn-Nb) magmatism in the European Variscan belt, a review. In: André-Mayer, A.S., Cathelineau, M., Muchez, P., Pirard, E., Sindern, S. (Eds.), Proceedings of the 13th Biennial SGA Meeting, 24–27 August 2015, Nancy, France, Vol, vol. 2, pp. 807–810. https://brgm.hal.science/hal-01156421.

Merceron, T., Bonhomme, M.G., Fouillac, A.M., Vivier, G., Meunier, A., 1987. Pétrologie des altérations hydrothermales du sondage GPF Echassières N. 1. Géol. Fr. 2-3, 259–269.

Merceron, T., Vieillard, P., Fouillac, A.-M., Meunier, A., 1992. Hydrothermal alterations in the Echassières granitic cupola (Massif central, France). Contrib. Mineral. Petrol. 112, 279–292. https://doi.org/10.1007/BF00310461.

Merino Martínez, E., 2014. Geochemistry, U-Pb Geochronology and Hf-Isotope Zircon Composition of Variscan Granitoids from the Montes de Toledo Batholith. [PhD thesis, Universidad Complutense Madrid, Spain]. https://www.academia.edu/108832323/Geoqu%C3%ADmica_geocronolog%C3%ADa_U_Pb_y_composici%C3%B3n_isot%C3%B3pica_de_Hf_en_circ%C3%B3n_de_granitoides_Variscos_del_batolito_de_los_Montes_de_Toledo.

Monecke, T., Dulski, P., Kempe, U., 2007. Origin of convex tetrads in rare earth element patterns of hydrothermally altered siliceous igneous rocks from the Zinnwald Sn-W deposit, Germany. Geochim. Cosmochim. Acta 71, 335–353. https://doi.org/10.1016/j.gca.2006.09.010.

Monier, G., Charoy, B., Cuney, M., Ohnensteter, D., Robert, J.L., 1987. Evolution spatiale et temporelle de la composition des micas du granite albitique à topaze-lepidolite de Beauvoir (Massif Central, France). Géol. Fr. 2-3, 179–188.

Monnier, L., Lach, P., Salvi, S., Melleton, J., Bailly, L., Béziat, D., Monnier, Y., Gouy, S., 2018. Quartz trace-element composition by LA-ICP-MS as proxy for granite differentiation, hydrothermal episodes, and related mineralization: the Beauvoir Granite (Echassières district), France. Lithos 320-321, 355–377. https://doi.org/10.1016/j.lithos.2018.09.024.

Monnier, L., Salvi, S., Melleton, J., Bailly, L., Béziat, D., De Parseval, P., Gouy, S., Lach, P., 2019. Multiple Generations of Wolframite Mineralization in the Echassières District (Massif Central, France). Miner 9, 637. https://doi.org/10.3390/min9100637.

Monnier, L., Salvi, S., Jourdan, V., Sall, S., Bailly, L., Melleton, J., Béziat, D., 2020. Contrasting fluid behavior during two styles of greisen alteration leading to distinct wolframite mineralizations: the Echassières district (Massif Central, France). Ore Geol. Rev. 124, 103648 https://doi.org/10.1016/j.oregeorev.2020.103648.

Monnier, L., Melleton, J., Vanderhaeghe, O., Salvi, S., Lach, P., Bruguier, O., Benmammar, A., Bailly, L., Béziat, D., Gloaguen, E., 2021. Episodic precipitation of Wolframite during an orogen: the Échassières district. Variscan belt of France. Miner. 11, 923. https://doi.org/10.3390/min11090923.

Monnier, L., Salvi, S., Melleton, J., Lach, P., Pochon, A., Bailly, L., Béziat, D., De Parseval, P., 2022. Mica trace-element signatures: Highlighting superimposed W-Sn mineralizations and fluid sources. Chem. Geol. 600, 120866 https://doi.org/10.1016/j.chemgeo.2022.120866.

Montel, J.-M., 1993. A model for monazite/melt equilibrium and application to the generation of granitic magmas. Chem. Geol. 110, 127–146. https://doi.org/10.1016/0009-2541(93)90250-M.

Müller, A., Spratt, J., Thomas, R., Williamson, B.J., Seltmann, R., 2018. Alkali-F-rich albite zones in evolved NYF pegmatites: the product of melt-melt immiscibility. Can. Mineral. 56, 657–687. https://doi.org/10.3749/canmin.1700087.

Nigon, P., 1988. La fluorine stratiforme de la bordure Ouest du Morvan: Géologie, Géochimie et modélisation. [Unpublished PhD thesis, Université d'Orléans].

Ohnenstetter, D., Piantone, P., 1988. Géochimie et évolutions des minéraux du groupe des columbo-tantalites et des minéraux du groupe du pyrochlore du sondage GPF 1 Echassières (Allier). Géol. Fr. 8, 113–163.

O'Sullivan, G., Chew, D., Kenny, G., Henrichs, I., Mulligan, D., 2020. The trace element composition of apatite and its application to detrital provenance studies. Earth Sci. Rev. 201, 103044 https://doi.org/10.1016/j.earscirev.2019.103044.

Pan, Y., Fleet, M.E., 2002. Compositions of the Apatite-Group Minerals: Substitution Mechanisms and Controlling Factors. Rev. Mineral. Geochem. 48, 13–49. https://doi.org/10.2138/rmg.2002.48.2.

Peng, H.-W., Fan, H.-R., Lecumberri-Sanchez, P., Lai, J.-Q., Hu, H.-L., Lan, T.-G., Li, X.-H., 2023. Fluid evolution and ore genesis of the Tiantangshan granite-related vein-type Rb-Sn-W deposit, South China: constraints from LA-ICP-MS analyses of fluid inclusions. Mineral. Deposita 58, 751–769. https://doi.org/10.1007/s00126-022-01155-7.

Peretyazhko, I.S., Savina, E.A., 2010. Tetrad effects in the rare earth element patterns of granitoid rocks as an indicator of fluoride-silicate liquid immiscibility in magmatic systems. Petrol 18, 514–543. https://doi.org/10.1134/S086959111005005X.

Pfister, J.D., Kontak, D.J., Groat, L.A., 2023. Textural and mineralogical evolution of the Little Nahanni pegmatite group (NWT, Canada) with implications for metasomatism, rare-metal mineralization, and pegmatite-wall rock interaction. Can. J. Mineral. Petrol. 61, 467–505. https://doi.org/10.3749/2000086.

Pichavant, M., 2022. Experimental Crystallization of the Beauvoir Granite as a Model for the Evolution of Variscan rare Metal Magmas. J. Petrol. 63, egac120. https://doi.org/10.1093/petrology/egac120.

Pichavant, M., Boher, M., Stenger, J.-F., Aïssa, M., Charoy, B., 1987a. Relations de phase des granites de Beauvoir à 1 et 3 kbar en conditions de saturation en H_2O. Géol. Fr. 2-3, 77–86.

Pichavant, M., Valencia Herrera, J., Boulmier, S., Briqueu, L., Joron, J.-L., Juteau, M., Michard, A., Sheppard, S.M.F., Treuil, M., Vernet, M., 1987b. The Macusani glasses, SE Peru: evidence of chemical fractionation in peraluminous magmas. Magmatic Process: Physicochemical Principles. Geochem. Soc. Spec. Publ. 1, 359–373.

Pichavant, M., Villaros, A., Deveaud, S., Scaillet, B., Lahlafi, M., 2016. The influence of redox state on mica crystallization in leucogranitic and pegmatitic liquids. Can. Mineral. 54, 559–581. https://doi.org/10.3749/canmin.1500079.

Pirajno, F., 2009. Hydrothermal Processes and Mineral Systems, first ed. Springer Science & Business Media.

Pochon, A., Gloaguen, E., Branquet, Y., Poujol, M., Ruffet, G., Boiron, M.-C., Boulvais, P., Gumiaux, C., Cagnard, F., Gouazou, F., Gapais, D., 2018. Variscan Sb-au mineralization in Central Brittany (France): a new metallogenic model derived from the Le Semnon district. Ore Geol. Rev. 97, 109–142. https://doi.org/10.1016/j.oregeorev.2018.04.016.

Putzolu, F., Seltmann, R., Dolgopolova, A., Armstrong, R.N., Shail, R.K., Spratt, J., Buret, Y., Broderick, C., Brownscombe, W., 2024. Influence of magmatic and magmatic-hydrothermal processes on the lithium endowment of micas in the Cornubian Batholith (SW England). Mineral. Deposita 59, 1067–1088. https://doi.org/10.1007/s00126-024-01248-5.

Raimbault, L., 1988. Géochimie des terres rares dans les fluorines fissurales du granite de Beauvoir entre 420 et 625 m (sondage GPF, Echassières, Massif central français). Géol. Fr. 8, 419–426.

Raimbault, L., 1998. Composition of complex lepidolite-type granitic pegmatites and of constituent columbite-tantalite, Chedeville, Massif Central. France. Can. Mineral. 36, 563–583.

Raimbault, L., Azencott, C., 1987. Géochimie des éléments majeurs et traces du granite à métaux rares de Beauvoir. Géol. Fr. 2-3, 189–198. https://geolfrance.brgm.fr/sites/default/files/upload/documents/gf19-2-3-1987_0.pdf.

Raimbault, L., Burnol, L., 1998. The Richemont rhyolite dyke, Massif Central, France; a subvolcanic equivalent of rare-metal granites. Can. Mineral. 36, 265–282. https://rruff.geo.arizona.edu/doclib/cm/vol36/CM36_265.pdf.

Raimbault, L., Cuney, M., Azencott, C., Duthou, J.-L., Joron, J.L., 1995. Geochemical evidence for a multistage magmatic genesis of Ta-Sn-Li mineralization in the granite at Beauvoir, French Massif Central. Econ. Geol. 90, 548–576. https://doi.org/10.2113/gsecongeo.90.3.548.

Ribeiro, H.B., Guedes, K.J., Pinheiro, M.V.B., Greulich-Weber, S., Krambrock, K., 2005. About the blue and green colours in natural fluorapatite. Phys. Status Solidi C 2, 720–723. https://doi.org/10.1002/pssc.200460274.

Robardet, M., 2002. Alternative approach to the Variscan Belt in southwestern Europe: Preorogenic paleobiogeographical constraints, in: Martínez Catalán, J.R., Hatcher, R. D., Jr., Arenas, R., Díaz García, F., (Eds.), Variscan-Appalachian dynamics: the building of the late Paleozoic basement: Boulder, Colorado. Geol. Soc. Am. Spec. Pap. 364, 1–15. https://doi.org/10.1130/0-8137-2364-7.1.

Robb, L., 2020. Introduction to Ore-Forming Processes, second ed. John Wiley & Sons.

Roda-Robles, E., Gil-Crespo, P.P., Pesquera, A., Lima, A., Garate-Olave, I., Merino-Martínez, E., Cardoso-Fernandes, J., Errandonea-Martin, J., 2022. Compositional Variations in Apatite and Petrogenetic significance: examples from Peraluminous Granites and Related Pegmatites and Hydrothermal Veins from the Central Iberian Zone (Spain and Portugal). Miner 12, 1401. https://doi.org/10.3390/min12111401.

Romer, R.L., Pichavant, M., 2020. Rare Metal Granites and Pegmatites, second ed. Encyclopedia of Geology.

Romer, R.L., Thomas, R., Stein, H.J., Rhede, D., 2007. Dating multiply overprinted Sn-mineralized granites - examples from the Erzgebirge, Germany. Mineral. Deposita 42, 337–359. https://doi.org/10.1007/s00126-006-0114-2.

Rosenbaum, G., Lister, G.S., Duboz, C., 2002. Relative motions of Africa, Iberia and Europe during Alpine orogeny. Tectonophys 359, 117–129. https://doi.org/10.1016/S0040-1951(02)00442-0.

Rossi, P., Autran, A., Burnol, L., Cuney, M., Ohnensteter, D., Monier, C., 1987. Logs pétrographiques et géochimiques du granite de Beauvoir dans le sondage Echassières I. Minéralogie et géochimie comparées. Géol. Fr. 2-3, 111–135.

Rudnick, R.L., Gao, S., 2003. The Composition of the Continental Crust. In: Holland, H. D., Turekian, K.K. (Eds.), Treatise on Geochemistry, vol. 3. The Crust. Elsevier-Pergamon, Oxford, pp. 1–64. https://doi.org/10.1016/B0-08-043751-6/03016-4.

Ruhlmann, F., Gillet, Y., Lissillour, J., 1980. Une occurrence uranifère à sélénium et bismuth dans la ceinture métamorphique du leucogranite de Mortagne-sur-Sèvre (Vendée). Bull. Mineral. 103, 245–249. https://doi.org/10.3406/bulmi.1980.7403.

Russell, J.K., Edwards, B.R., Shyder, L.D., 1995. Volatile production possibilities during magmatic assimilation: heat and mass-balance constraints, in: Thompson JF Magmas, fluids and ore deposits. Mineral. Ass. Can. Short Course Series 23, 1–24.
Sánchez, V., Cardellach, E., Corbella, M., Vindel, E., Martín-Crespo, T., Boyce, A.J., 2010. Variability in fluid sources in the fluorite deposits from Asturias (N Spain): further evidences from REE, radiogenic (Sr, Sm, Nd) and stable (S, C, O) isotope data. Ore Geol. Rev. 37, 87–100. https://doi.org/10.1016/j.oregeorev.2009.12.001.
Sarcia, J.A., Carrat, J., Poughon, A., Sanselme, H., 1958. Geology of uranium vein-deposits in France; Géologie des gites uranifères et filoniens en France. Rapport CEA 1032, France. https://www.osti.gov/etdeweb/servlets/purl/20912748.
Schmitz, M.D., Bowring, S.A., Ireland, T.R., 2003. Evaluation of Duluth complex anorthositic series (AS3) zircon AS a U-Pb geochronological standard: New high-precision isotope dilution thermal ionization mass spectrometry results. Geochim. Cosmochim. Acta 67, 3665–3672. https://doi.org/10.1016/S0016-7037(03)00200-X.
Schoene, B., Bowring, S.A., 2006. U-Pb systematics of the McClure Mountain syenite: thermochronological constraints on the age of the $^{40}Ar/^{39}Ar$ standard MMhb. Contrib. Mineral. Petrol. 151, 615–630. https://doi.org/10.1007/s00410-006-0077-4.
Schulmann, K., Edel, J.-B., Catalán, J.R.M., Mazur, S., Guy, A., Lardeaux, J.-M., Ayarza, P., Palomeras, I., 2022. Tectonic evolution and global crustal architecture of the European Variscan belt constrained by geophysical data. Earth Sci. Rev. 234, 104195 https://doi.org/10.1016/j.earscirev.2022.104195.
Schulz, B., 2009. EMP-monazite age controls on P-T paths of garnet metapelites in the Variscan inverted metamorphic sequence of La Sioule, French Massif Central. Bull. Soc. Géol. Fr. 180, 271–282. https://doi.org/10.2113/gssgfbull.180.3.271.
Schwartz, M.O., Surjono, 1990. Greisenization and albitization at the Tikus tin-tungsten deposit, Belitung, Indonesia. Econ. Geol. 85, 691–713. https://doi.org/10.2113/gsecongeo.85.4.691.
Schwartz, M.O., 1992. Geochemical criteria for distinguishing magmatic and metasomatic albite-enrichment in granitoids - examples from the Ta-Li granite Yichun (China) and the Sn-W deposit Tikus (Indonesia). Mineral. Deposita 27, 101–108. https://doi.org/10.1007/BF00197092.
Seo, J., Choi, S.-G., Kim, D.W., Park, J.W., Oh, C.W., 2015. A new genetic model for the Triassic Yangyang iron-oxide-apatite deposit, South Korea: Constraints from in situ U-Pb and trace element analyses of accessory minerals. Ore Geol. Rev. 70, 110–135. https://doi.org/10.1016/j.oregeorev.2015.04.009.
Sha, L.-K., Chappell, B.W., 1999. Apatite chemical composition, determined by electron microprobe and laser-ablation inductively coupled plasma mass spectrometry, as a probe into granite petrogenesis. Geochim. Cosmochim. Acta 63, 3861–3881. https://doi.org/10.1016/S0016-7037(99)00210-0.
Shepherd, T.J., Miller, M.F., Scrivener, R.C., Darbyshire, D.F., 1985. Hydrothermal fluid evolution in relation to mineralization in Southwest England with special reference to the Dartmoor-Bodmin area. In: High Heat Production (HHP) Granites, Hydrothermal Circulation and Ore Genesis. Conference, pp. 345–364.
Sheppard, S.M., 1986. Characterization and isotopic variations in natural waters. In: Valley, J., Taylor, H., O'Neil, J. (Eds.), Stable Isotopes in High Temperature Geological Processes. De Gruyter, Berlin, Boston, pp. 165–184. https://doi.org/10.1515/9781501508936-011.
Shuai, X., Li, S.-M., Zhu, D.-C., Wang, Q., Zhang, L.-L., Zhao, Z., 2021. Tetrad effect of rare earth elements caused by fractional crystallization in high-silica granites: an example from Central Tibet. Lithos 384, 105968. https://doi.org/10.1016/j.lithos.2021.105968.
Sillitoe, R.H., 2010. Porphyry copper systems. Econ. Geol. 105, 3–41. https://doi.org/10.2113/gsecongeo.105.1.3.
Sizaret, S., Marcoux, E., Jébrak, M., Touray, J.C., 2004. The Rossignol fluorite vein, Chaillac, France: multiphase hydrothermal activity and intravein sedimentation. Econ. Geol. 99, 1107–1122. https://doi.org/10.2113/gsecongeo.99.6.1107.
Sizaret, S., Marcoux, E., Boyce, A., Jebrak, M., Stevenson, R., Ellam, R., 2009. Isotopic (S, Sr, Sm/Nd, D, Pb) evidences for multiple sources in the early Jurassic Chaillac F-Ba ore deposit (Indre, France). Bull. Soc. Géol. Fr. 180, 83–94. https://doi.org/10.2113/gssgfbull.180.2.83.
Smedley, P.L., Kinniburgh, D.G., 2002. A review of the source, behaviour and distribution of arsenic in natural waters. Appl. Geochem. 17, 517–568. https://doi.org/10.1016/S0883-2927(02)00018-5.
Soule de Lafont, D., Lhegu, J., 1980. Les gisements stratiformes du Morvan (Sud-Est du bassin de Paris, France). In: International Geological Congrès, p. 40.
Stacey, J.T., Kramers, J.D., 1975. Approximation of terrestrial lead isotope evolution by a two-stage model. Earth Planet. Sci. Lett. 26, 207–221. https://doi.org/10.1016/0012-821X(75)90088-6.
Stampfli, G.M., Borel, G.D., Marchant, R., Mosar, J., 2002. Western Alps geological constraints on western Tethyan reconstructions. J. Virtual Explor. 8, 77–106. https://doi.org/10.3809/jvirtex.2002.00057.
Štemprok, M., 1987. Greisenization (a review). Geol. Rundsch. 76, 169–175. https://doi.org/10.1007/BF01820580.
Szuszkiewicz, A., Pieczka, A., Gołębiowska, B., Dumańska-Słowik, M., Marszałek, M., Szełęg, E., 2018. Chemical composition of Mn-and Cl-rich apatites from the Szklary pegmatite, Central Sudetes, SW Poland: Taxonomic and genetic implications. Miner 8, 350. https://doi.org/10.3390/min8080350.
Tait, J., Schätz, M., Bachtadse, V., Soffel, H., 2000. Palaeomagnetism and Palaeozoic palaeogeography of Gondwana and European terranes. Geol. Soc. Lond. Spec. Publ. 179, 21–34. https://doi.org/10.1144/GSL.SP.2000.179.01.04.
Tartèse, R., Boulvais, P., 2010. Differentiation of peraluminous leucogranites "en route" to the surface. Lithos 114, 353–368. https://doi.org/10.1016/j.lithos.2009.09.011.
Taylor, R.G., 1988. Pervasine hydrothermal alteration in tin bearing granites and implications for the evolution of ore-bearing fluids. Can. Inst. Min. Metall. Spec. 39, 86–95.
Taylor, J.R., Wall, V.J., 1993. Cassiterite solubility, tin speciation, and transport in a magmatic aqueous phase. Econ. Geol. 88, 437–460. https://doi.org/10.2113/gsecongeo.88.2.437.
Thomas, R., Webster, J.D., Davidson, P., 2011. Be-daughter minerals in fluid and melt inclusions: implications for the enrichment of be in granite-pegmatite systems. Contrib. Mineral. Petrol. 161, 483–495. https://doi.org/10.1007/s00410-010-0544-9.
Thomson, S.N., Gehrels, G.E., Ruiz, J., Buchwaldt, R., 2012. Routine low-damage apatite U-Pb dating using laser ablation-multicollector-ICPMS. Geochem. Geophys. Geosyst. 13 https://doi.org/10.1029/2011GC003928.
Tischendorf, G., 1977. Geochemical and petrographic characteristics of silicic magmatic rocks associated with rare-metal mineralization. In: Štemprok, M., Burnol, L., Tischendorf, G. (Eds.), Metallization Associated with Acid Magmatism, 2. Geol. Surv. Prague, Prague, pp. 41–96.
Turpin, L., Cuney, M., Friedrich, M., Bouchez, J.-L., Aubertin, M., 1990a. Meta-igneous origin of Hercynian peraluminous granites in NW French Massif Central: implications for crustal history reconstructions. Contrib. Mineral. Petrol. 104, 163–172. https://doi.org/10.1007/BF00306440.
Turpin, L., Leroy, J.L., Sheppard, S.M., 1990b. Isotopic systematics (O, H, C, Sr, Nd) of superimposed barren and U-bearing hydrothermal systems in a Hercynian granite, Massif Central, France. Chem. Geol. 88, 85–98. https://doi.org/10.1016/0009-2541(90)90105-G.
Van Hinsbergen, D.J., Torsvik, T.H., Schmid, S.M., Maţenco, L.C., Maffione, M., Vissers, R.L., Gürer, D., Spakman, W., 2020. Orogenic architecture of the Mediterranean region and kinematic reconstruction of its tectonic evolution since the Triassic. Gondwana Res. 81, 79–229. https://doi.org/10.1016/j.gr.2019.07.009.
Vanderhaeghe, O., Laurent, O., Gardien, V., Moyen, J.-F., Gébelin, A., Chelle-Michou, C., Couzinié, S., Villaros, A., Bellanger, M., 2020. Flow of partially molten crust controlling construction, growth and collapse of the Variscan orogenic belt: the geologic record of the French Massif Central. BSGF - Earth Sci. Bull. 191, 25. https://doi.org/10.1051/bsgf/2020013.
Veksler, I.V., Dorfman, A.M., Kamenetsky, M., Dulski, P., Dingwell, D.B., 2005. Partitioning of lanthanides and Y between immiscible silicate and fluoride melts, fluorite and cryolite and the origin of the lanthanide tetrad effect in igneous rocks. Geochim. Cosmochim. Acta 69, 2847–2860. https://doi.org/10.1016/j.gca.2004.08.007.
Velichkin, V.I., Vlasov, B.P., 2011. Domal structures and hydrothermal uranium deposits of the Erzgebirge, Saxony, Germany. Geol. Ore Depos. 53, 74–83. https://doi.org/10.1134/S1075701511010053.
Vermeesch, P., 2018. IsoplotR: a free and open toolbox for geochronology. Geosci. Front. 9, 1479–1493. https://doi.org/10.1016/j.gsf.2018.04.001.
Villa, I.M., De Bièvre, P., Holden, N.E., Renne, P.R., 2015. IUPAC-IUGS recommendation on the half life of ^{87}Rb. Geochim. Cosmochim. Acta 164, 382–385. https://doi.org/10.1016/j.gca.2015.05.025.
Wang, R., 1988. Etude minéralogique et cristallochimique de cassitérite, niobo-tantalates et minéraux disséminés du granite de Beauvoir (Allier) : implications métallogéniques. [Unpublished PhD thesis, Université Paul Sabatier, Toulouse].
Wang, H., Cai, K., Sun, M., Xia, X.-P., Lai, C.-K., Li, P., Wan, B., Zhang, Z., 2022. Apatite as a magma redox indicator and its application in metallogenic research. Lithos 422, 106749. https://doi.org/10.1016/j.lithos.2022.106749.
Warr, L.N., 2021. IMA-CNMNC approved mineral symbols. Mineral. Mag. 85, 291–320. https://doi.org/10.1180/mgm.2021.43.
Webster, J.D., Tappen, C.M., Mandeville, C.W., 2009. Partitioning behavior of chlorine and fluorine in the system apatite-melt-fluid. II: Felsic silicate systems at 200 MPa. Geochim. Cosmochim. Acta 73, 559–581. https://doi.org/10.1016/j.gca.2008.10.034.
Webster, J.D., Baker, D.R., Aiuppa, A., 2018. Halogens in mafic and intermediate-silica content magmas. In: Harlov, D., Aranovich, L. (Eds.), The Role of Halogens in Terrestrial and Extraterrestrial Geochemical Processes. Springer Geochem, pp. 307–430. https://doi.org/10.1007/978-3-319-61667-4_6.
Wendt, I., Lenz, H., Höhndorf, A., Bültemann, H., Bültemann, W.-D., 1979. Das Alter der Pechblende der Lagerstätte Menzenschwand, Schwarzwald. Z. Dtsch. Geol. Ges. 130, 619–626 (with an abstract in English).
Witt, W.K., 1988. Evolution of high-temperature hydrothermal fluids associated with greisenization and feldspathic alteration of a tin-mineralized granite, Northeast Queensland. Econ. Geol. 83, 310–334. https://doi.org/10.2113/gsecongeo.83.2.310.
Worden, R.H., 1996. Controls on halogen concentrations in sedimentary formation waters. Mineral. Mag. 60, 259–274. https://doi.org/10.1180/minmag.1996.060.399.02.
Worden, R.H., 2018. Halogen elements in sedimentary systems and their evolution during diagenesis. In: Harlov, D., Aranovich, L. (Eds.), The Role of Halogens in Terrestrial and Extraterrestrial Geochemical Processes. Springer Geochem, pp. 185–260. https://doi.org/10.1007/978-3-319-61667-4_4.
Xu, J., Xia, X.-P., Wang, Q., Spencer, C.J., Zhang, L., Zhu, X., 2024. Apatite textures, elemental and isotopic compositions unmask the homogenizing process in silicic magma chambers. Geophys. Res. Lett. 51 https://doi.org/10.1029/2023GL106646 e2023GL106646.
Yang, W.-B., Niu, H.-C., Shan, Q., Sun, W.-D., Zhang, H., Li, N.-B., Jiang, Y.-H., Yu, X.-Y., 2014. Geochemistry of magmatic and hydrothermal zircon from the highly evolved Baerzhe alkaline granite: implications for Zr-REE-Nb mineralization. Mineral. Deposita 49, 451–470. https://doi.org/10.1007/s00126-013-0504-1.

Zhang, X., Guo, F., Zhang, B., Zhao, L., Wu, Y., Wang, G., Alemayehu, M., 2020. Magmatic evolution and post-crystallization hydrothermal activity in the early cretaceous Pingtan intrusive complex, SE China: Records from apatite geochemistry. Contrib. Mineral. Petrol. 175, 1–18. https://doi.org/10.1007/s00410-020-1675-2.

Zhang, F., Guo, F., Zhang, X., Zhao, L., Hua, W., Huang, X., Tian, X., 2024. Multiple-pulse magmatic intrusion and fluid metasomatism in Mesozoic Qianlishan rare metal granite, South China: Records from apatite geochemistry. Lithos 474, 107580. https://doi.org/10.1016/j.lithos.2024.107580.

Zhao, Z.-F., Zheng, Y.-F., 2003. Calculation of oxygen isotope fractionation in magmatic rocks. Chem. Geol. 193, 59–80. https://doi.org/10.1016/S0009-2541(02)00226-7.

Zheng, Y.-F., 1996. Oxygen isotope fractionations involving apatites: Application to paleotemperature determination. Chem. Geol. 127, 177–187. https://doi.org/10.1016/0009-2541(95)00088-7.